Phenomenology of gamma-ray spectral features induced by dark matter cascade processes

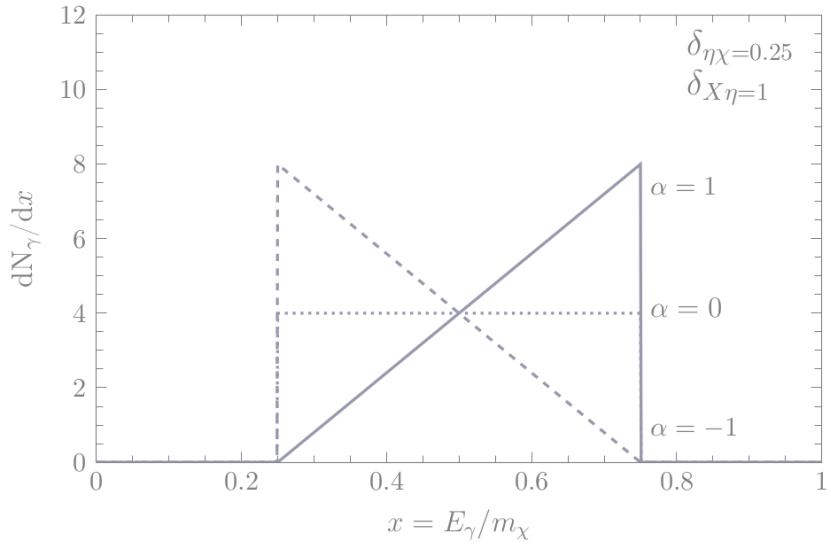

Dissertation

by

Sergio Andrés López Gehler

Excellence Cluster Universe


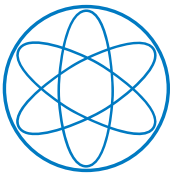

Phenomenology of gamma-ray spectral features induced by dark matter cascade processes

Sergio Andrés López Gehler

Vollständiger Abdruck der von der Fakultät für Physik der Technischen Universität München zur Erlangung des akademischen Grades eines

Doktors der Naturwissenschaften

genehmigten Dissertation.

Vorsitzender:	Prof. Dr. Peter Fierlinger
Prüfer der Dissertation:	1. Prof. Dr. Alejandro Ibarra
	2. Prof. Dr. Nora Brambilla

Diese Dissertation wurde am 25.07.2016 bei der Technischen Universität München eingereicht und durch die Fakultät für Physik am 29.08.2016 angenommen.

A mi abuelita,
me voy a acordar de tí,
siempre.

Abstract

In this thesis, we study the gamma-ray output of 1-step dark matter cascade processes. The emitted spectrum can present distinctive features which are given by the details of the specific dark matter model. These spectral features are confined to an energy regime dictated by the kinematics of the process, yielding different kinds of spectra from narrow, line-like features to wide signals, providing always a sharp cut-off at the maximal photon energy. The shape of the signal can vary depending on the particle type involved in the intermediate state of the cascade. We classify these features as gamma-ray boxes and triangles. Then, we investigate the power of dark matter indirect searches for these features. We find that gamma-ray boxes and triangles are useful tools, setting upper limits on the dark matter annihilation cross section down to $\langle \sigma v \rangle \simeq 10^{-29}\,\mathrm{cm}^3\,\mathrm{s}^{-1}$ and cover over four orders of magnitude in the dark matter mass using current and future experiments. Furthermore, gamma-ray triangles open the possibility of probing asymmetric dark matter with indirect detection.

Zusammenfassung

In dieser Arbeit untersuchen wir die in kaskadenförmigen Annihilationen von Dunkler Materie entstehende Gammastrahlung, welche entsprechend der spezifischen Details des Modells verschiedene markante Merkmale aufweisen kann. Diese spektralen Merkmale sind auf ein von der Kinematik bestimmendes Energieintervall begrenzt, mit einer Form von engen Linien-ähnlichen Spektren bis hin zu weiter ausgedehnten Signaltypen, aber in jedem Fall mit einem scharfen Abfall bei der maximalen Photonenergie. Der genaue Typ des Signals hägt dabei von den Art des Teilchens ab welches im Zwischenschritt des Kaskadenprozesses auftritt. Wir klassifizieren diese spektralen Merkmale der Gammastrahlung als box- und dreiecksförmig. Anschließend untersuchen wir die Relevanz der indirekten Suche nach diesen Merkmalen. Unsere Ergebnisse zeigen, dass die box- und dreiecksförmigen Spektren verwendet werden können um im Bereich von vier Größenordnungen in der Masse der Dunklen Materie starke obere Schranken an den Annihilationswirkungsquerschnitt zu setzen, bis hin zu $\langle \sigma v \rangle \simeq 10^{-29}\,\mathrm{cm}^3\,\mathrm{s}^{-1}$. Des Weiteren zeigen wir, dass dreiecksförmige Spektren die Möglichkeit eröffnen asymmetrische Dunkle Materie mit Hilfe von indirekter Detektion zu untersuchen.

Contents

1. Introduction

The standard models of cosmology and particle physics are currently the most fundamental theories in physics. The first succeeds in explaining the evolution of the Universe from the early stages after the Big Bang until today. The second is an elegant description of the particle content of the Universe and the governing interactions. Three of the four known interactions can be explained as gauge theories, whereas the remaining interaction—that being gravity—is described using the over one hundred years old field equations by Einstein. Nevertheless, there are still several open issues which still lack a satisfying theory behind them.

One of the unresolved issues is connected to the concept called *dark matter*. Several observations have shown that the behaviour of structures at different scales, ranging from tens of kpc up to several tens of Mpc, differs from the one predicted by otherwise the widely accepted theory of gravity. These phenomena can be addressed by the consideration of the dark matter paradigm: the existence of some kind of non-luminous, non-baryonic, and gravitationally interacting substance. First indications of such observations can be tracked down back to the decade of 1920, when the astronomers Jacobus Kapteyn [1] and James Jeans [2] studied the vertical motion of stars near the Galactic plane. They predicted the presence of what they called dark stars in order to explain their findings. In the following years, Oort [3] and Zwicky [4] also observed unexpected movement of celestial bodies which could be explained by the gravitational potential induced by what Zwicky called "dunkle Materie", German for dark matter. After ground breaking discoveries from observations of the rotation curves of galaxies in 1970 [5] and of colliding galaxy clusters in 2006 [6], among others, the hypothesis of dark matter became a leading field of research. A very appealing class of dark matter candidates is given by weakly interacting massive particles, a scenario where dark matter is described as remnants from early stages of the universe which decoupled from the thermal bath early enough to allow for structure formation. However, other attractive scenarios are also possible e.g., asymmetric dark matter, a model where baryogenesis and dark matter share a common production mechanism. In light of the attention this area has drawn, a myriad of experiments was built hoping to observe non-gravitational signals induced by dark matter. A subset of these experiments relies on indirect search strategies—a strategy which hopes to discover dark matter through the observation of cosmic rays.

This work investigates dark matter using gamma-rays as carriers. Depending on the specific details of dark matter, the photon output of dark matter annihilation or decay may be produced with distinctive energy spectra. Such is the case of cascade processes, where dark matter interactions produce an intermediate state which in turn decays into at least one photon. These features can be categorised as *gamma-ray boxes* or *gamma-ray triangles*. We devote this thesis to the study of these signals, their phenomenology, the dark matter models able to produce them, and the sensitivity of experiments towards them. This work is structured in the following way: In chapter 2 we summarise briefly the standard models of particle physics and cosmology. In chapter 3 we explain in detail the concept of dark matter, its history and the current state of research. Chapter 4 discusses exclusively gamma-rays in the contexts of astroparticle physics and dark matter indirect detection. We start the second part with chapter 5, where we explain the phenomenology of gamma-ray boxes and triangles. Then, in chapter 6, we explain in detail

three different particle physics models which give rise to these signals. Finally, in chapter 7 we compare quantitatively the gamma-ray fluxes expected from these signatures to the data measured by different telescopes and the expected performance of future experiments. We end this work with a summary of the conclusions in chapter 8.

This thesis is largely based in the following works:

[7] **Gamma-ray boxes from axion-mediated dark matter,**
A. Ibarra, H. M. Lee, S. L ópez Gehler, W.-I. Park, and M. Pato, JCAP 1305 (2013) 016, [Erratum: JCAP1603,no.03,E01(2016)].

[8] **On the sensitivity of CTA to gamma-ray boxes from multi-TeV dark matter,**
A. Ibarra, A. S. Lamperstorfer, S. López-Gehler, M. Pato, and G. Bertone, JCAP 1509 (2015), no. 09 048.

[9] **Gamma-ray triangles: a possible signature of asymmetric dark matter in indirect searches,**
A. Ibarra, S. Lopez-Gehler, E. Molinaro, and M. Pato, arXiv:1604.01899.

We remark that some figures and parts of the discussion is also presented in these publications.

Part I.

State of the art: Where we stand

2. Standard models of particle physics and cosmology

The reach of this work lies within the branch of physics called *astroparticle physics*, a cross disciplinary field of research requiring the input of particle physics, astrophysics, and cosmology. On the one hand, the Standard Model of particle physics (SM) describes the fundamental building blocks of matter and the mechanics of their interactions as a gauge theory under the group G_{SM}, described in the first section. On the other hand, the Λ-CDM Model explains modern cosmology, which we address in the second section of this chapter. Together these two theories describe nature at its most fundamental level. In this chapter, we discuss the SM and Λ-CDM Model in a concise manner. Throughout this work we assume $\hbar = c = 1$ unless explicitly stated otherwise.

2.1. Standard model of particle physics

This is the most fundamental theory in physics up to date. It describes the particle content of the universe and their interactions using Quantum Field Theory (QFT) as a gauge theory under the group $G_{SM} = SU(3)_C \times SU(2)_L \times U(1)_Y$, where the electroweak symmetry $SU(2)_L \times U(1)_Y$ is spontaneously broken at lower temperatures leaving a remaining $U(1)_{em}$. A thorough overview of the SM lies outside the scope of this work; we refer to [10, 11] for a more extensive review. Instead, we present it in a superficial fashion, summarising the content, mechanisms, and unresolved issues.

2.1.1. The model

The SM includes several fields that constitute the fundamental particle content of the universe. Twelve of the thirteen elementary particles known to date are described by fermion fields, whereas the thirteenth is a scalar field linked to the Higgs mechanism. The interaction between these states is dictated by their transformation behaviour under the group G_{SM}, as gauge fields are introduced to ensure gauge symmetry. We summarise the particle content of the SM and their respective representations in the upper panel of table 2.1 with the notation $(\mathbf{c}, \mathbf{l})_y$, where $\mathbf{c}$ and $\mathbf{l}$ are the numeric labels of the corresponding representation under the groups $SU(3)_C$ and $SU(2)_L$, respectively, and y is the hypercharge of the one dimensional representation of $U(1)_Y$. We align them according to their families and generations, and distinguish between *quarks*—non-trivial transformation under $SU(3)_C$—and *leptons*.

In this phase, the fermion fields are massless, since the mass terms are not allowed due to gauge symmetry. However, these terms can be generated via the Higgs mechanism through the spontaneous symmetry breaking (SSB) of the electroweak symmetries. At lower energy scales, the Higgs field acquires a non-vanishing vacuum expectation value (vev) $\langle h^0 \rangle \to v \neq 0$, which breaks the electroweak symmetry to a remaining $U(1)_{em}$. Three main consequences can be listed from this transition: First, the Yukawa couplings between the fermions and the scalar induce mass terms for the fermions, with exception of the neutrino fields ν_α. Second, the

	Generation 1st	2nd	3rd	Repr. $(\mathbf{c},\mathbf{l})_y$	$U(1)_{em}$ charge Q
Leptons	$\begin{pmatrix}\nu_e\\ e\end{pmatrix}_L$	$\begin{pmatrix}\nu_\mu\\ \mu\end{pmatrix}_L$	$\begin{pmatrix}\nu_\tau\\ \tau\end{pmatrix}_L$	$(\mathbf{1},\mathbf{2})_{-1/2}$	0 -1
	e_R	μ_R	τ_R	$(\mathbf{1},\mathbf{1})_{-1}$	-1
Quarks	$\begin{pmatrix}u\\ d\end{pmatrix}_L$	$\begin{pmatrix}c\\ s\end{pmatrix}_L$	$\begin{pmatrix}t\\ b\end{pmatrix}_L$	$(\mathbf{3},\mathbf{2})_{1/6}$	$2/3$ $-1/3$
	u_R	c_R	t_R	$(\mathbf{3},\mathbf{1})_{2/3}$	$2/3$
	d_R	s_R	b_R	$(\mathbf{3},\mathbf{1})_{-1/3}$	$-1/3$
Scalar field		$\begin{pmatrix}h^+\\ h^0\end{pmatrix}$		$(\mathbf{1},\mathbf{2})_{1/2}$	$-$ 0

before SSB	$SU(3)_C$	$SU(2)_L$	$U(1)_Y$
	$G^\mu_{i=1..8}$	$W^\mu_{j=1..3}$	B^μ
after SSB	$SU(3)_C$	$U(1)_{em}$	massive
	$G^\mu_{i=1..8}$	A^μ	$W^\mu_\pm$, Z^μ

Table 2.1.: Top: Summary of the transformation behaviour of the fermion and scalar fields in the SM before the electroweak symmetry breaking and the charge for the residual $U(1)_{em}$ symmetry after the transition. Bottom: Gauge fields of the group G_{SM} before the electroweak symmetry breaking, and the remnants afterwards.

four gauge fields of the electroweak symmetry group are reformulated as one remaining gauge field, the photon, and three massive vector fields the $W^\pm$ and Z bosons. And third, a massive uncharged scalar particle remains from the scalar field, namely the Higgs boson. The $SU(3)_C$ gauge bosons are unaffected by this mechanism. We summarise this transition of the gauge fields in the lower panel of table 2.1. This theory succeeds brilliantly at describing almost all phenomena at high energies, and is in agreement with other low-energy theories.

2.1.2. Unresolved issues

Although the SM provides an accurate description of elementary particles and their interactions, there are still some open questions, one of which is closely linked to the topic of this thesis: The origin and nature of dark matter. This subject will be investigated in detail in later chapters; instead here we address briefly two other unsettled issues.

Hierarchy Problem

The Higgs sector, as introduced previously, has a conceptual problem. The Higgs mass receives additive renormalisation corrections of the order of the cut-off scale Λ. Currently, there are no strong hints for the magnitude of this scale, however it is expected to lay at Grand Unification Theories (GUTs) scales or even Planck scales, which usually lie above $10^{16}\,\mathrm{GeV}$. If this is the case, the bare mass of the Higgs particle lies in a similar energy scale, implying that the radiatively corrected mass term is tuned down fourteen orders of magnitude to the observed mass $m_h \simeq 125\,\mathrm{GeV}$. This dramatic cancellation and fine tuning is widely considered to be unnatural, and has led to several efforts to address this concern. One of the most studied proposals is called *supersymmetry* [12], which postulates a relation between bosons and fermions, and as a result a large number of new elementary particles is introduced.

Neutrino masses

A strong argument against the SM being a complete description of nature is the fact that neutrinos are massive. The discovery of neutrino oscillations [13–15] point to non-zero mass terms for the neutral leptons. Up to date, there is no clear method of generating such terms with strong empirical support; however a large set of possible mechanisms have been studied. The most intuitive strategy is to generate neutrino mass terms in the same way as in the quark sector. This is achieved by introducing a new leptonic degree of freedom to the Lagrangian: right-handed neutrinos. In order not to violate any symmetry of the Lagrangian, these new states are required to be completely sterile under G_{SM}, i.e. $(\mathbf{1},\mathbf{1})_0$. Other possibilities include different types of *see-saw mechanisms* or the introduction of new heavy degrees of freedom.

2.2. Standard model of cosmology

As the SM describes the constituents of matter and their interactions, the Big Bang cosmological framework is explained by the Λ-CDM model. It accounts a large set of empirical evidence on an immense span of scales and includes naturally the concepts of dark matter and dark energy. General Relativity (GR) is assumed and used for the description of gravity at all scales, and the SM for the other three fundamental forces. In the remainder of this chapter we explain briefly the main aspects of this model. For a more thorugh exposition of the cosmological model we refer to e.g. [16]. Since this work is focused on dark matter, we leave a more in-depth discussion of this topic for chapter 3.

The description of gravity according to GR states that the matter-energy content curves space-time in such a way to induce gravitational interactions. This is summed up in the equations of the gravitational field of Einstein

$$R_{\mu\nu} - \frac{1}{2} R\, g_{\mu\nu} = -\frac{8\pi G}{c^4} T_{\mu\nu} + \Lambda\, g_{\mu\nu}\,, \tag{2.1}$$

where c is the speed of light, $R_{\mu\nu}$ and R are the Ricci tensor and scalar, respectively, $g_{\mu\nu}$ is the metric tensor, G is Newton's constant, $T_{\mu\nu}$ is the energy-momentum tensor, and Λ is the cosmological constant. These equations describe the relation between geometry of space-time, on the left-hand side, and the mass-energy content of the universe on the right-hand side. We note that the second term on the right-hand side is not explicitly related to the mass-energy content, but is rather an inherent property of space-time itself, dictated by empirical evidence on the geometry and energy content of the universe. Furthermore, we accept the cosmological principle which implies homogeneity and isotropy of the universe, two properties strongly supported by experimental evidence—particularly the *Cosmic Microwave Background* (CMB). With these two symmetries we can simplify the metric to

$$\mathrm{d}s = -c^2 \mathrm{d}t^2 + a(t) \left(\frac{\mathrm{d}r^2}{1 - kr^2} + r^2 \mathrm{d}\Omega^2 \right) , \tag{2.2}$$

known as the Friedmann-Lemaitre-Robertson-Walker metric. Here, $a(t)$ is the scale factor and $k \in \{-1, 0, 1\}$ is the curvature parameter. Using this metric, one of the components of the Einstein equations (2.1) leads to the Friedmann equation

$$H^2 + \frac{k}{a^2} = \frac{8\pi G}{3} \rho_{\mathrm{tot}} \quad \text{with} \quad H(t) \equiv \frac{\dot{a}(t)}{a(t)}\,, \tag{2.3}$$

and ρ_{tot} being the total average energy density of the universe. This equation governs the expansion of the universe in terms of the Hubble parameter $H(t)$. Current estimations for the present-day value of H using measurements of the CMB yield $H_0 \equiv 67.27 \pm 0.66\,\text{km}\,\text{s}^{-1}\,\text{Mpc}^{-1} = h\,100\,\text{km}\,\text{s}^{-1}\,\text{Mpc}^{-1}$ [17], with h being the reduced Hubble constant. We separate three possible geometries of the universe, depending on the value of the curvature parameter k. From equation (2.3), we read that for a total energy density equal to a critical density $\rho_{\text{tot}} = \rho_{\text{c}}$, the universe is flat, i.e. $k = 0$. If the total energy density is larger or smaller than this critical value, the universe is said to be open ($k = 1$) or closed ($k = -1$). It is customary to express the energy density of a particular species i in terms of the critical density as

$$\Omega_i = \frac{\rho_i}{\rho_{\text{c}}} \quad \text{with} \quad \rho_{\text{c}} \equiv \frac{3H^2}{8\pi\, G}\,. \tag{2.4}$$

We also introduce the parameter

$$\Omega_{\text{K}} = \Omega_{\text{tot}} - 1 = \sum_i \Omega_i - 1 \tag{2.5}$$

as a measurement of the flatness of the universe. We say the universe is flat when $\Omega_{\text{K}} = 0$.

Empirical evidence points towards a flat universe made up of a small amount of baryonic matter, a larger amount of *cold dark matter* (CDM). However, this matter content is relatively small and cannot account for the observed flatness. The remaining energy density is called Dark Energy and is attributed to the cosmological constant Λ, hence the name Λ-CDM model. We expand on this discussion in chapter 3.

3. Dark matter

This work is concerned with *dark matter*. Therefore, we devote a complete chapter to the description of the concept, its properties, and the experimental efforts pursuing its observation. First, we summarise the evolution of the concept of dark matter and the ground breaking works and discoveries related to it. Second, we discuss some possible candidates. Lastly, we address the current state of experimental search strategies and efforts. For the rest of this work we reserve the Greek letter χ exclusively for dark matter related entities—such as fields, particles, and masses—or as a name tag referring to dark matter.

3.1. Experimental evidence

Several studies in the last century point to deeper gravitational potentials than the ones expected from observed luminous and baryonic matter [18]. All of these so-called *missing-mass problems* can elegantly and consistently be explained by the presence of a non-luminous kind of matter on all cosmological scales. Furthermore, other studies e.g., on the CMB or on *Big Bang Nucleosynthesis* (BBN), require this additional kind of matter to be non-baryonic. We call this new kind of matter dark matter. Below we discuss compelling evidence towards the existence of dark matter. Therefore, assuring that dark matter has been discovered is not a bold statement, although its specific (particle) nature is left undetermined. We briefly review the most relevant experimental evidences in support of the conjecture of dark matter, from which we also derive important properties.

First missing-mass observations

In the year 1922, the astronomers Jacobus Kapteyn [1] and James Jeans [2] studied the vertical motion of stars near the Galactic plane. This led to an estimation of the density of the Galaxy, for which the results by Jeans required the presence of two dark stars to every bright star. Almost ten years later, the Dutch astronomer Jan Oort and the Swiss astronomer Fritz Zwicky found a similar discrepancy between the gravitational and luminous matter contents. On a galactic scale, Oort found that the stars in the Milky Way moved more rapidly than expected from the gravity exerted by luminous matter [3]. The study carried out by Zwicky one year later arrived at a similar conclusion at the scale of galaxy clusters [4]. Relying on measurements of the velocities of galaxies from the Coma Cluster and the virial theorem he realised that $\simeq 400$ solar masses per solar luminosity were required.

Probably, the most famous hint for the existence of non-luminous matter is the discrepancy between the measured and expected *rotation curves*: The rotational velocity of stars v_{rot} as a function of the distance to the respective galactic centre. Observed and investigated by Vera Rubin and Kent Ford in 1970 [5], this ground-breaking discovery clearly stated the necessity of stronger gravitational potentials than the one expected from luminous matter. Figure 3.1 illustrates the results of similar measurements of the NGC 3195 galaxy adapted from [19]. Newtonian dynamics predicts $v_{\mathrm{rot}} \propto 1/\sqrt{r}$ outside the visible disk, since the amount of enclosed

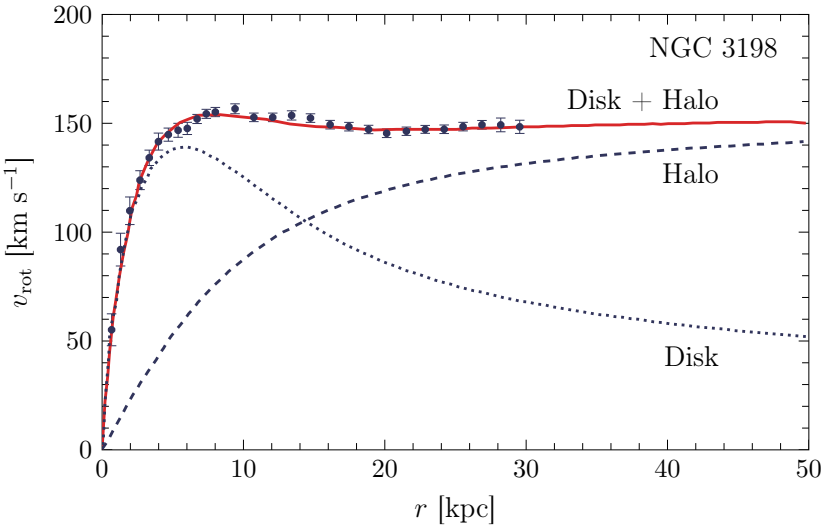

Figure 3.1.: Rotation curve of the galaxy NGC 3198 adapted from [19]. For small radii, $r < 4\,\mathrm{kpc}$, the circular velocity expected from the gravitational potential exerted by the luminous disk (dotted line) is in agreement with the data. For larger radii, $r \gtrsim 10\,\mathrm{kpc}$, the need for a stronger gravitational potential becomes apparent. With the insertion of a non-luminous massive halo (dashed line) this discrepancy is lifted. The predicted circular velocity by the total mass of disk and halo (solid line) provides a good fit to the data.

matter is not expected to vary for larger radii. The flatness of the curves clearly hints for non-luminous matter extending onto larger regions than luminous matter, otherwise stars would scatter away from the galactic centre. Recent works were able to demonstrate the necessity of dark matter even inside the solar circle using the rotation curve of the Milky Way [20].

Although these missing-mass problems can be elegantly explained with the inclusion of dark matter, alternative theories exist. The possibility of this dark component being baryonic e.g., in form of *Massive Compact Halo Objects* (MACHOs) is, at this stage of the discussion, still open. After all, baryonic matter is not required to have a light emitting component. This interpretation loses its validity in light of further experimental analyses as we explained below. Furthermore, alternatives to Newtonian gravity are also a viable explanation [21]. However, studies on strong and weak lensing (see below) disfavour the idea of *Modified Newtonian Dynamics* (MOND).

The Bullet Cluster and lensing

Gravitational lensing is a phenomenon predicted by GR and has proven to be a powerful tool in the search for dark matter. The matter distribution of the Bullet Cluster—a system of two colliding clusters of galaxies—was determined using weak lensing and then compared to X-ray images of the interstellar gas of the same region [6]. Figure 3.2 displays both results simultaneously. A clear offset of the centre of the mass from the centre of luminous mass peaks can be seen. This distinguishes a baryonic, interacting, and light-emitting kind of matter from an opposite dark component that lacks all three properties just mentioned, disfavouring both MOND and MACHOs. Furthermore, an active search for MACHOs using microlensing towards the Large Magellanic Cloud found that these objects are too scarce to account for the

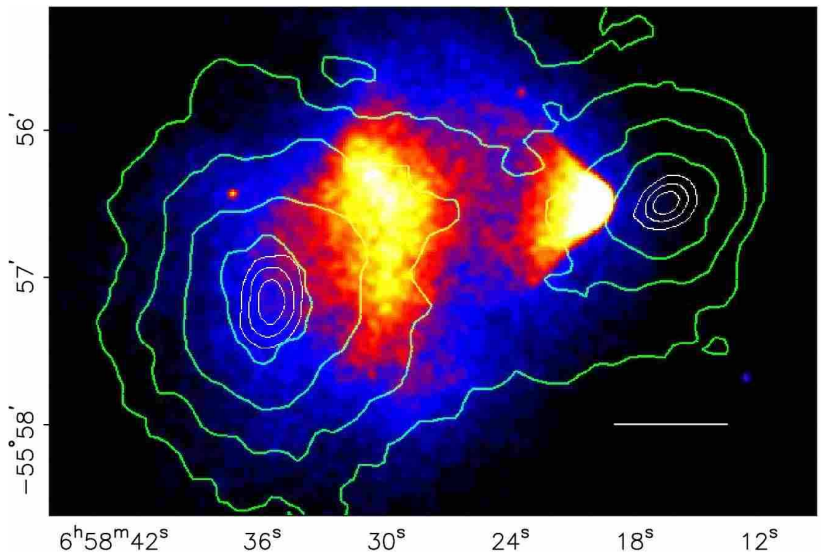

Figure 3.2.: X-ray image of the colliding Bullet Cluster (1E 0657-558) as observed by the Chandra telescope, together with the distribution of mass obtained by weak lensing (green contours). Figure taken from [6].

observations [22].

Strong lensing is also able to deliver similar statements. The total mass of an object can be inferred by the distortion of light due to massive objects leading to formations of Einstein rings and arcs. The presence of dark matter predicts a larger mass concentration as the one calculated from the luminous matter. This is observed, for instance, in the study performed in reference [23] where the absolute mass of the galaxy cluster Abell 1689 was measured by the gravitational lens magnification of a background galaxy population induced by the gravitational potential of the cluster.

Cosmology

In section 2.2, we introduced the CMB, which is similar to a fingerprint left from the moment of recombination. This radiation is remarkably isotropic and follows almost exactly a Planck distribution of temperature $T = 2.7255\,\mathrm{K}$ [17]. However, tiny fluctuations of the order of 10^{-5}, as seen most recently by the Planck space telescope [24], encode important information about the energy content of the universe. These fluctuations are partially rooted in the gravitational wells responsible for redshifting photons at early stages of the universe, a phenomenon known as the Sachs-Wolf effect. Before recombination, no stable atoms or any larger matter clumps could form due to the photon pressure in the plasma. However, for the formation of structures as observed today, gravitational inhomogeneities at early stages of the universe are required. Therefore, some non-baryonic and non-luminous kind of matter is needed for the development of these gravitational inhomogeneities. Analysing the temperature field as a decomposition in spherical harmonics allows us to determine the baryonic and dark (non-baryonic) contributions to the matter budget. The CMB power spectrum measured by Planck [17] is depicted in figure 3.3 where the solid line corresponds to the best-fit for the cosmoligcal parameters. In terms of density fractions Ω_i, as introduced in section 2.2, and the reduced Hubble constant h,

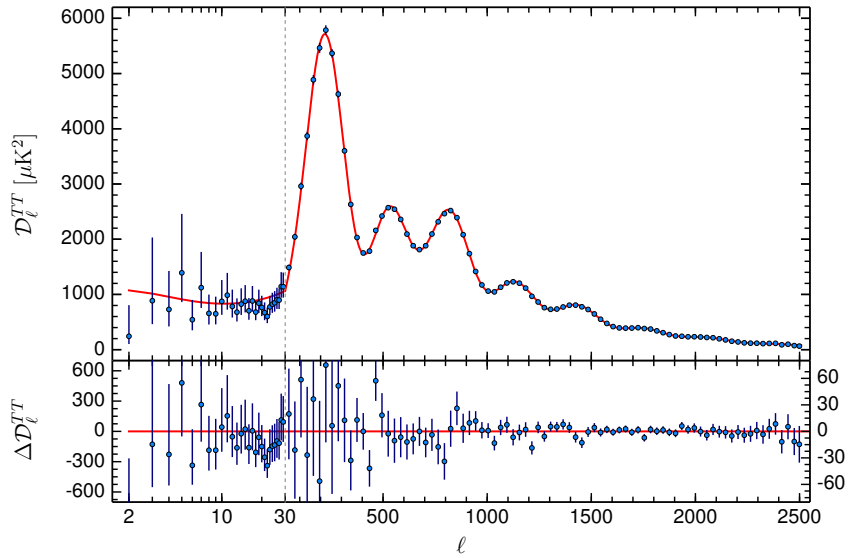

Figure 3.3.: The temperature power spectrum of the CMB as measured by Planck, and the best-fit base ΛCDM spectrum (solid red line) are shown in the upper panel. The residuals between model and data are shown in the lower panel. Figure taken from [17].

we have [17]

$$\Omega_\mathrm{b}h^2 = 0.02225 \pm 0.00016 \quad \text{and} \quad \Omega_\chi h^2 = 0.1198 \pm 0.0015\,. \tag{3.1}$$

Clearly, there is a non-baryonic component making $\simeq 80\%$ of the total matter budget. These results are in concordance with those from BBN, which was the only probe capable of measuring the baryon density before the precision measurements of the CMB were carried out; predicting the abundances of light nuclei and restricting the amount of baryonic matter to [25]

$$0.021 \leq \Omega_\mathrm{b}h^2 \leq 0.024\,. \tag{3.2}$$

Higher baryonic densities would have had an impact on BBN and raised tensions with the observed amount of primordial deuterium. From the CMB it is also possible to determine the total energy content of the universe and therefore its geometry (c.f. section 2.2). These results are strongly supported by studies on the redshift of supernovae [26–28] and on the correlation of baryonic acoustic oscillations with luminous red galaxies [29]:

$$\Omega_\mathrm{M} = 0.3156 \pm 0.0091 \quad \text{and} \quad \Omega_\Lambda = 0.6844 \pm 0.0091\,; \tag{3.3}$$

$$\Omega_\mathrm{K} = 0.040^{+0.038}_{-0.041}\,. \tag{3.4}$$

These calculations show that the geometry of the universe is (close to) flat and therefore a large amount of *dark energy* besides the total matter content is present. We call *dark matter* to the non-baryonic and non-luminous matter required by all of the observations above.

An intuitive candidate for these empirical evidences are neutrinos. Carrying no electric charge and being massive, these leptons seem well suited in order to account for the early

gravitational wells and the non-baryonic content of the universe. However, measurements from the CMB are able to constrain the abundance of relic neutrinos to [17, 25]

$$\Omega_\nu h^2 = \sum_i \frac{m_{\nu_i}}{93\,\mathrm{eV}} < 0.0052\,, \tag{3.5}$$

which is less than 5% of the amount of dark matter required. The existence of other neutrino like particles has also been discredited by these data. Furthermore, the growth of structures is inconsistent with dark matter being constituted solely by neutrinos, as we explain in the following.

We can label dark matter as cold (CDM) or hot (HDM) depending on its velocity at the time of structure formation. If particles moved at non-relativistic velocities we have CDM, otherwise we have HDM for which the neutrino is a standard example[1]. After recombination, baryons fell into the existing gravitational wells—also required by the CMB measurements discussed above—formed by dark matter, otherwise matter would be homogeneously distributed and no structures would have formed. Thus, these two scenarios differ in their description of the evolution of large-scale structures. In an HDM scenario, superclusters would form first and later smaller objects such as galaxies through fragmentation. This scenario is known as *top-down* large-scale structure evolution. On the contrary, a CDM scenario describes it as a *bottom-up* process, where smaller inhomogeneities survive which in turn cluster into larger objects. The observed universe strongly favours CDM [16, 30, 31]. Furthermore, a no-dark matter paradigm as proposed by MOND disagrees strongly with these observations [32].

In conclusion to these discussions a large set of properties can be assigned to dark matter: It is a non-baryonic kind of matter carrying no electric charge, which is significantly more abundant than ordinary matter. At the moment of structure formation it is required for it to have non-relativistic velocities and to be stable or at least long lived. Provided these properties, dark matter is able to explain a large amount of otherwise unexpected observations.

3.2. Candidates

To date, there are no evident experimental results narrowing down the possible particle properties that dark matter may have. This is then reflected into a large set of possible realisations, differing on several characteristics each model could have, such as dark matter mass, interaction with other particles, or production mechanism. In the following paragraphs we outline the concepts of *Weakly Interacting Massive Particles* (WIMPs) and *Asymmetric Dark Matter* (ADM) with considerable depth, as they are of special interest for this work.

3.2.1. WIMPs

Although the SM predicts a large amount of elementary and bound states, only five particles contribute actively to the energy budget of the universe: electrons, protons, neutrons, neutrinos, and photons. These remaining particles do not annihilate or decay into lighter states, due to symmetries or absence of annihilation partners, as do the rest of the particles present in the primordial thermal bath. A quite natural assumption is for dark matter to be a remnant from the past as well, with the corresponding properties necessary for any dark matter candidate,

[1] Warm dark matter (WDM) is also a possibility, if dark matter became non-relativistic at the time of structure formation. We address this scenario as equivalent to CDM.

c.f. section 3.1. We review briefly the WIMP framework, where dark matter is interpreted as a relic with weak interactions.

Motivation

By definition a WIMP is any massive particle which interacts through some portal with ordinary matter with a cross section of the order of weak interactions. Historically, a large set of candidates were being considered separately, all of them falling within the definition of a WIMP. Standard examples are massive neutrinos, supersymmetric particles such as neutralinos, gravitinos, or sneutrinos [18]. Besides fulfilling all required conditions of a dark matter candidate, the most compelling property is the production of the right relic density (see below). A relic with a mass in the order of GeV to TeV subject to weak interactions decouples from the thermal bath with the correct density to account for the observed dark contribution to the total mass density of the universe. This paradigm opens the possibility to detection prospects, since an interaction akin to

$$\chi\chi \leftrightarrow XX, \tag{3.6}$$

with X any SM particle is guaranteed to exist. To date, WIMPs are the most popular candidates due to their simplicity and detectability. Furthermore, several models predict such particles as a by-product. As we study later on, dark matter could have a certain dark particle-antiparticle asymmetry. We study this case separately, therefore we assume a fully symmetrical WIMP density, as several models do.

Freeze-out

According to the current cosmological paradigm, the universe has gone through several transitions as it expands and cools down. The CMB is the print left from the recombination epoch, when photons decoupled from the rest of matter. Similarly, neutrinos detached from a weak-interacting thermal equilibrium with protons, neutrons, and electrons when the rate of expansion of the universe overcame that of the interaction. These resulting ubiquitous remnants are commonly referred to as *relics* and it is not unreasonable for dark matter to be such a particle. We call this process thermal *freeze-out*, the properties of which we now summarise. Here, we focus exclusively on freeze-out as a production mechanism for WIMPs, and refer to e.g. [16] for a more broad description. This framework relies on the interplay between the expansion of the universe and the balance of a dark matter annihilation-production process into SM particles, $\chi\chi \leftrightarrow XX$. This process is initially at equilibrium and, as the universe cools down, the number density per comoving volume n_χ drops as $e^{-m_\chi/T}$. In a stationary universe, this would continue until the dark matter budget depletes. However, the expansion rate of the universe H counters the annihilation rate Γ eventually overcoming it. Henceforth, dark matter is completely detached from thermal equilibrium with the number density per comoving volume being conserved. A detailed description of this mechanism is done using a special case of the Boltzmann equation and the law of entropy conservation. Introducing the fiducial quantities $Y_\chi \equiv n_\chi/s$, with s the entropy density, and $x \equiv m_\chi/T$, T being the temperature of the thermal bath, we write [33]

$$\frac{\mathrm{d}Y_\chi}{\mathrm{d}x} = \frac{1}{3H}\frac{\mathrm{d}s}{\mathrm{d}x}\langle\sigma v\rangle\left[Y_\chi^2 - \left(Y_\chi^{\mathrm{eq}}\right)^2\right], \tag{3.7}$$

where $Y_\chi^{\mathrm{eq}} = n_\chi^{\mathrm{eq}}/s$, with the equilibrium number density n_χ^{eq}, and the Hubble parameter H. We use the expression for H derived from the Friedmann equation (2.3) and introduce the

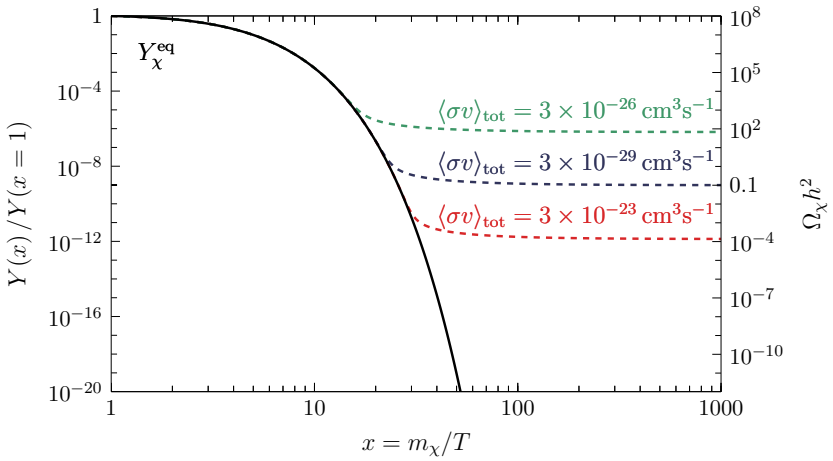

Figure 3.4.: Evolution of the WIMP comoving abundance $Y = n_\chi/s$ as a function of $x = m_\chi/T$ for an expanding universe as described by equation (3.9). The equilibrium abundance $Y_\chi^{\rm eq}$ (solid black) drops, however at freeze out, the expansion rate overcomes the annihilation rate and the number density freezes out (dashed). Several choices for $\langle\sigma v\rangle_{\rm tot}$ are depicted in different colours.

degrees-of-freedom parameter $g_*^{1/2}$

$$H^2 = \frac{8\pi}{3M_P^2}\rho_{\rm tot} \quad \text{and} \quad g_*^{1/2} = \frac{h_{\rm eff}}{g_{\rm eff}^{1/2}}\left(1 + \frac{1}{3}\frac{T}{h_{\rm eff}}\frac{{\rm d}h_{\rm eff}}{{\rm d}T}\right), \tag{3.8}$$

where $g_{\rm eff}$ and $h_{\rm eff}$ are the effective degrees of freedom for the energy and entropy density, respectively, and $M_P = 1.22\times10^{19}\,{\rm GeV}$ is the Planck mass. With these two expressions, equation (3.7) can be rewritten as

$$\frac{{\rm d}Y_\chi}{{\rm d}x} = -\frac{m_\chi\, M_P\, g_*^{1/2}}{x^2}\sqrt{\frac{\pi}{45}}\langle\sigma v\rangle\left[Y_\chi - \left(Y_\chi^{\rm eq}\right)^2\right]. \tag{3.9}$$

The boundary condition for this first order differential equation stems from the assumption that for higher temperatures dark matter was in equilibrium with the thermal bath, hence $Y_\chi = Y_\chi^{\rm eq}$ for $x \simeq 1$. From the solution, we extract the freeze-out temperature $x_{\rm f.o.}$ and the relic abundance $Y_{\rm f.o.} = Y_\chi\,(x\to\infty)$. As discussed in section 3.1, we argued in favour of CDM against HDM, this implies that the freeze-out temperature is ought to be $x_{\rm f.o.} \gg 3$. We show in figure 3.4 the numerical solution of equation (3.9) for different annihilation cross sections. At early stages, WIMPs remain in chemical and thermal equilibrium suffering a suppression as the temperature drops. However, at $x = x_{\rm f.o.}$, when the Hubble expansion rate becomes of the order of the annihilation rate—i.e. the mean free path for dark matter annihilations becomes larger than the Hubble radius—dark matter decouples and its number density converges to $Y_\chi \to Y_\chi^{\rm f.o.}$. In standard cosmology, the freeze-out temperature is approximately $x_{\rm f.o.} \simeq 20$ and therefore the approximate average velocity of dark matter at freeze-out is $v_{\rm f.o.}^2 = 0.3$ [33]. As a result of this analysis, we find that the relic density $\Omega_\chi h^2$ (and the freeze-out temperature $x_{\rm f.o.}$) of a WIMP scenario is dictated by the value of the thermally averaged cross section times velocity as

$$\Omega_\chi h^2 = \frac{h^2\, m_\chi s_0\, Y_{\rm f.o.}}{\rho_0} \simeq \frac{2.2\times10^{-27}\,{\rm cm^3\,s^{-1}}}{\langle\sigma v\rangle}, \tag{3.10}$$

where s_0 denotes the entropy density today, and ρ_0 denotes the present critical density. From this equation and as illustrated in figure 3.4 we see that for increasing cross sections the asymptotic number density drops. From the estimates outlined in the previous section, we expect for dark matter to account for a specific amount of energy density $\Omega_\chi h^2 \simeq 0.12$. Implying for the sum of the cross sections over all the possible annihilation channels

$$\langle \sigma v \rangle_{\text{tot}} = \sum_X \langle \sigma v \rangle_{XX} \simeq 2.2 \times 10^{-26}\,\text{cm}^3\,\text{s}^{-1}\,. \tag{3.11}$$

A remarkable coincidence is the similarity of this scale with that of the weak nuclear force, which is often label WIMP *miracle*. For instance, the annihilation cross section of a stable neutrino with mass of some GeV occurring through the exchange of a Z boson would lie in the order of $\langle \sigma v \rangle \simeq 10^{-27}\,\text{cm}^3\,\text{s}^{-1}$.

3.2.2. Asymmetric Dark Matter

Within the scope of this work we partially address the concept of ADM: when dark matter presents a particle-antiparticle asymmetry similarly to visible matter. This assumption is not unnatural, since the abundances of visible and dark matter are fairly similar today. Furthermore, the density of baryonic matter is established by an asymmetry and it stands to reason for dark matter to share this origin: this is the ADM hypothesis. It is possible to attribute this asymmetry to certain processes that transpired at early stages of the universe. We make a concise overview of the concept of ADM and refer to [34,35] for more comprehensive analyses.

Motivation

In section 3.1 we saw that the present-day mass density of dark matter is larger than the baryonic one approximately by a factor of six

$$\Omega_\chi \simeq 6\,\Omega_\text{b}\,, \tag{3.12}$$

that is, both densities lie in the same order of magnitude. It is possible to treat this coincidence as chance. However, the ADM paradigm suggests a rather more sensible hypothesis: attribute said coincidence to a connection between the origins of both sectors. Simple reasoning and observation shows an excess of baryons B over antibaryons $\overline{B}$. Indeed this asymmetry has been observed even at cosmological scales and parametrised by [17]

$$\eta_B \equiv \frac{n_B - n_{\overline{B}}}{s} \simeq 10^{-10}\,, \tag{3.13}$$

where the number densities of baryons and antibaryons are denoted by n_B and $n_{\overline{B}}$, respectively, and s is the entropy density. This asymmetry is responsible for the density of baryons, since protons and neutrons—as long as bounded in nuclei— are stable. A common origin of visible and dark matter implies an active asymmetry in the dark sector as well, which dictates the dark matter number density Y_χ. Assuming both species have similar energy densities and using equation (3.12), we have

$$\frac{\Omega_\chi}{\Omega_\text{b}} = \frac{m_\chi\, Y_\chi}{m_\text{b}\, Y_\text{b}} \simeq 6\,. \tag{3.14}$$

This suggests a fiducial dark matter mass of $m_\chi \simeq 6\,\text{GeV}$, with $m_\text{b} \simeq 1\,\text{GeV}$ being the mass of the proton. However, different factors such as a Boltzmann suppression, non-trivial dark

quantum numbers, or differing densities allow other mass scales. Usually ADM models are described by a gauge structure

$$\mathrm{G_{SM}} \times \mathrm{G}_\chi \,, \tag{3.15}$$

connecting each factor to the visible and dark sectors, respectively. The dark gauge structure G_χ and its particle content accounts for dark matter and any other interactions and mechanisms related to it (e.g., dark radiation or the generation of the asymmetry). A complex dark sector is not necessary, however the model is required to include two key properties in order to qualify as a plausible ADM scenario: First, an (approximately) conserved quantum number—such as baryon number or electric charge in the visible sector—is needed, such that an asymmetry can be initially defined, we call this a *dark baryon number* and label it as B_χ. And second, an annihilation channel for disposing the remaining symmetric component of the dark sector must be ensured, similar to electroweak interactions in the SM. Any higher degree of complexity is arbitrary and limited only by the imagination of the model builder, therefore we do not investigate this in depth, instead we analyse possible frameworks for ADM scenarios.

Generating an asymmetry

For the generation of an asymmetry of a certain species with charge X the well-known Sakharov conditions need to be fulfilled [36]: out-of-equilibrium processes violating X, and also violation of C and CP symmetry. The mechanism of any ADM scenario follows usually these steps:

1. An asymmetry is generated in either the visible or the dark sector, which is then communicated through some portal to the corresponding non-asymmetric sector. It is also possible to generate separate asymmetries in each sector which are then balanced through a similar portal.

2. The process connecting the two sectors decouples, freezing in the asymmetries separately at that instant.

3. Any remaining symmetric fractions annihilate. In the case of baryons this occurs via electroweak interactions, and in the case of dark matter through the *ad hoc* annihilation channel.

We distinguish two cases for the first step: When an already existing asymmetry from the visible matter is *transferred* to the dark sector, and when the dark sector plays an active role in the *generation* of the asymmetry. In the case of transfer, an existing baryogenesis model is assumed to have generated an asymmetry, which is passed on to dark matter. This can occur through electroweak non-perturbative field configurations or sphalerons, assuming some connection of dark matter to the $\mathrm{SU(2)_L}$ group (e.g. [37]), or high dimension operators enabling the communication between both sectors (for instance [38, 39]), among others. We split the second case into two subcategories: *Cogenesis*, when the generation of the asymmetry is shared between the sectors, and *darkogenesis*[2], when that task is left exclusively to the dark sector and transferred via sphalerons or high dimension operators, analogously to the first case. Common cogenesis scenarios are: out-of-equilibrium decays e.g. [40–43] (adapted from Fukugita-Yanagida leptogenesis [44]), models based on the Affleck-Dine (AD) mechanism [45–47], electoweak cogenesis [48], and asymmetric freeze-out [49]. The last framework is of particular interest, since it marries the ideas of ADM and WIMPs with all the corresponding perks. Dark baryogenesis or

[2]Some literature use the term *darkgenesis*.

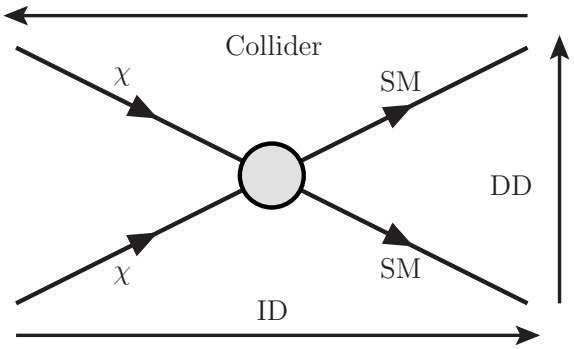

Figure 3.5.: Illustration of the three different search strategies based on different kinds of interactions between dark matter and SM particles: Dark matter indirect detection (ID), dark matter direct detection (DD), and collider searches.

darkogenesis can occur in different ways: The cogenesis methods of out-of-equilibrium decays and AD mechanism can be made exclusive to the dark sector becoming darkogenesis scenarios. Electoweak baryogenesis mechanisms (through phase transitions) can be realised in a suited dark sector instead, such as in [50,51]. In similar fashion, spontaneous baryogenesis [52–54] can be employed to generate a spontaneous dark baryogenesis [55–57]. The summary of scenarios presented in the previous lines is not considered as a complete catalogue of all the existing ADM models; for a fully comprehensive listing we refer to [34, 35].

Other frameworks

The two recently discussed frameworks are part of a far larger set. To date, there are several dark matter candidates each with their own compelling features. Usually these models are constructed from three different kinds of approaches [58]. A microscopical approach, when a minimal extension of the SM effectively introduces dark matter, its interactions and production, with observable consequences. An observable approach, when the properties of dark matter are systematically tailored as an interpretation of empiric material. And a fundamental approach, when dark matter is a by-product of a broader theory at a more fundamental level e.g., supersymmetry. An extensive review on the existing frameworks can be found in reference [59]. In particular candidates such as axions [60] and sterile neutrinos [61], or cases where dark matter is embedded in Kaluza-Klein, composite Higgs [62] or supersymmetric theories [63] are compelling possibilities.

3.3. Search strategies

It is possible to interpret the cosmological and astrophysical evidence as proof for the existence of dark matter. However, to date there is no unambiguous confirmation for the existence of a dark matter particle as it is understood in QFT. The experimental pursuits for data supporting the existence of such a particle is a current effort amongst large international collaborations. There are three search strategies that rely on the interactions of dark matter with standard matter, which are illustrated in figure 3.5. As introduced in section 3.2.1, WIMPs guarantee the reversible annihilation $\chi\chi \leftrightarrow XX$, where X stands for any particular SM particle, therefore the scattering interaction $\chi X \rightarrow \chi X$ is also ensured. Although this work is not uniquely focused on one specific dark matter framework, we illustrate the search strategies using WIMPs, as

Halo model i	α	β	γ	r_s [kpc]
NFW	1	3	1	20
Moore	1	3.02	1.16	30
Cuspy gen.	1	3	1.2	20
Isothermal	2	2	0	4.4
Cored gen.	2.9	2.5	0	4.4
Einasto	0.17			20

Table 3.1.: Parameters for the dark matter density distribution profiles from equations (3.16) and (3.17) [65].

these can be probed by a variety of methods. Then, these strategies can be extended to other frameworks, provided they fulfil the proper characteristics e.g., an annihilation channel into SM particles. In this section, we describe two out of the three strategies: dark matter indirect and direct detection, leaving collider searches out, since they are not relevant within the scope of this work. We also summarise the current status of experimental efforts.

3.3.1. Indirect strategies

We start our discussion on search strategies with dark matter indirect detection. As depicted in figure 3.5, dark matter annihilation gives way to the production of SM particles. The concept of indirect searches is to detect these particles as cosmic rays, provided that they can be backtracked or attributed, in some way, to dark matter. Assuming an annihilation cross section $\langle \sigma v \rangle \simeq 2.2 \times 10^{-26}\,\mathrm{cm}^3\,\mathrm{s}^{-1}$—as suggested by the WIMP paradigm—, the fluxes of different channels, predicted by physical models, are of a relevant intensity and can be tested by existing experiments. Moreover, some anomalous observations of gamma-rays and positrons hint to signals which could be of dark matter origin. Decaying dark matter is a putative scenario, since the stability of dark matter is not ensured, which would give rise to signatures in indirect detection experiments as well. Since the discussion is qualitatively the same, we leave out an explicit consideration of this case and focus on annihilating dark matter. We discuss the main elements required for the computation of signals from a dark origin as well as the different detection channels. Since gamma-rays are of special interest for this work, we leave a detailed discussion on this topic for chapter 4. We refer to [64] for a comprehensive summary of the current status of indirect detection.

Dark matter distribution

From the rotation curves, as presented in section 3.1, we inferred that the Galactic disk is embedded in a dark matter halo, without any specific description of the density distribution. For the computation of signals from dark matter annihilation, a definite quantification of the amount and allocation of dark matter is needed. Several possibilities were considered which can be grouped into two sets, *cored* profiles which turn constant for smaller radii; and *cusped* profiles which grow rapidly near the Galactic Centre (GC). On the one hand, cusped profiles, such as Navarro-Frenk-White (NFW) [66,67], Einasto [68,69], Moore [70], or cuspy generalised profiles [68,71] are favoured by more recent numerical N-body simulations. On the other hand, cored profiles e.g., truncated Isothermal [72,73] or cored generalised profiles [74] are motivated by the observation of rotation curves of other galaxies [65]. The functional expressions of these

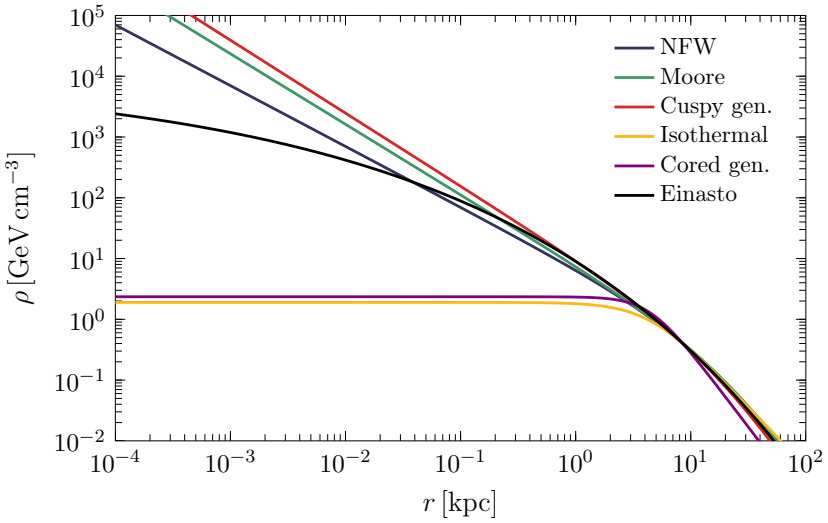

Figure 3.6.: Dark matter density distribution profiles against the distance from the GC. All profiles are normalised to $\rho_0 \equiv \rho(8.5\,\mathrm{kpc}) = 0.4\,\mathrm{GeV\,cm^{-3}}$. For details on the functional expresions of the profiles and references see text.

profiles read:

$$\rho_i\,(r) \;=\; \frac{\rho_s}{(r/r_s)^{\gamma}\,[1+(r/r_s)^{\alpha}]^{(\beta-\gamma)/\alpha}}\,, \tag{3.16}$$

$$\rho_{\mathrm{Ein}} \;=\; \rho_s\,\exp\left\{-\frac{2}{\alpha}\left[\left(\frac{r}{r_s}\right)^{\alpha}-1\right]\right\}, \tag{3.17}$$

where ρ_s and r_s are the scale density and radius. Equation (3.16) is a generalised profile with the parameters as described in table 3.1. These parameters must be in accordance with two astrophysical observations: The local dark matter density $\rho_0 \equiv \rho\,(R_0) \simeq 0.4\,\mathrm{GeV\,cm^{-3}}$ [75, 76], where $R_0 \simeq 8.5\,\mathrm{kpc}$ [77–80] is the distance from the Sun to the GC, and the total dark matter mass contained within a certain volume [65]. We plot these profiles in figure 3.6. We remark that recent simulations, which include interactions with baryonic matter, found profiles which were even more pronounced near the GC than that predicted by dark matter only simulations [81, 82].

The formation of dark matter halos from the perspective of the Λ-CDM model is also an important feature, since fine structural properties of dark matter halos at different scales are strongly correlated to their formation epoch [83–87]. The prediction of substructure within a halo is of particular interest for dark matter indirect detection, as these regions with a higher dark matter density would be promising for the search of a dark matter signal. Furthermore, it is possible to find a correlation between the mass of a halo and its dark matter density distribution reducing the number of parameters of the profiles to one [88–90].

Charged cosmic rays

After being produced the final-state SM particles are subject to hadronisation and decay processes. We intend to detect these particles with experiments at Earth, therefore the channels under scrutiny for indirect searches are stable particles: protons, electrons, neutrinos, and photons (naturally, their antiparticles as well). Effectively, these particles are produced at a

certain rate depending on the specific dark matter model, which can be expressed as source functions[3]

$$q(E_X) = \frac{1}{2}\left(\frac{\rho_\chi}{m_\chi}\right)^2 \langle\sigma v\rangle \sum_X \mathrm{BR}_X \frac{\mathrm{d}N_X}{\mathrm{d}E_X}\,, \tag{3.18}$$

where $\mathbf{r}$ is the position of the annihilation, E the energy at which particle X is emitted, BR_X is the branching fraction of that channel, and $\mathrm{d}N_X/\mathrm{d}E_X$ is the energy spectrum.

We begin by discussing charged particles as carriers and their detection prospects. In most models, SM particles are generated as a particle-antiparticle pair, in contrast to astrophysical sources which generate mainly ordinary matter. Antiparticles are better suited for indirect searches, since their backgrounds are far fainter than those of electrons and protons. The path these particles have to travel is by no means trivial. Due to electromagnetic interactions, they get entangled in the Galactic magnetic fields and diffuse randomly. This diffusion is generally described by a transport equation with a source given by equation (3.18), which can be solved analytically, semi-analytically, or numerically for the given boundary conditions and properties of dark matter. Furthermore, open source tools for the numerical solution of the equation are available, such as DRAGON [91] and GALPROP [92]. Using this knowledge, we can make an educated guess on the expected fluxes at Earth coming from dark matter and compare them with measurements from different experiments. The antiproton flux follows closely the one predicted by astrophysical sources observed by PAMELA [93] and AMS-02 [94], and therefore allows the estimation of strong upper limits on the annihilation cross section of dark matter [95–98]. We display in the left panel of figure 3.7 constraints on $\langle\sigma v\rangle$ for different annihilation channels, using the Einasto dark matter profile and the MED propagation model, computed by [98]. On the contrary, the positron fraction—the ratio $e^+/(e^- + e^+)$—displays a rise at energies $\gtrsim 10\,\mathrm{GeV}$ that is unexpected from the astrophysical background. This observation was first hinted by HEAT [99] and later confirmed by PAMELA [100–102], AMS-02 [103–105], and Fermi [106]. Although this signal can be attributed to dark matter [107], it is also possible to interpret it as re-acceleration of positron secondaries [108–110] and as pulsar radiation [111], the latter being the more likely explanation according to reference [107]. Furthermore, even if dark matter is not responsible for the rise, it is possible to draw constraints from these measurements [112,113]. These limits can test cross sections down to the same level as antiproton observations, as shown in the right panel of figure 3.7. However, both results obtained by the observation of positrons and antiprotons are sensitive to the propagation model chosen for the analysis, yielding to results which can vary by more than an order of magnitude [95,113].

Radio waves

We briefly discuss the status of indirect detection from observations of the radio sky. In contrast to cosmic rays, neutrinos, or gamma rays, radio waves are emitted as dark matter secondary radiation: Charged particles—mostly electrons and positrons—accelerated by the magnetic fields emit electromagnetic waves in form of synchrotron radiation. This is part of the energy losses that influence the transport equation of charged particles, therefore the adopted diffusion model has strong repercussions on the calculations [114]. The distance a particle covers whilst generating synchrotron radiation is minuscule in contrast to Galactic scales, and can be generally interpreted as an in situ emission. Therefore, morphological information of the emission can be critical for a thorough analysis. The synchrotron emission is computed by

[3]Scenarios where dark matter is not self-conjugated require an additional factor 1/2.

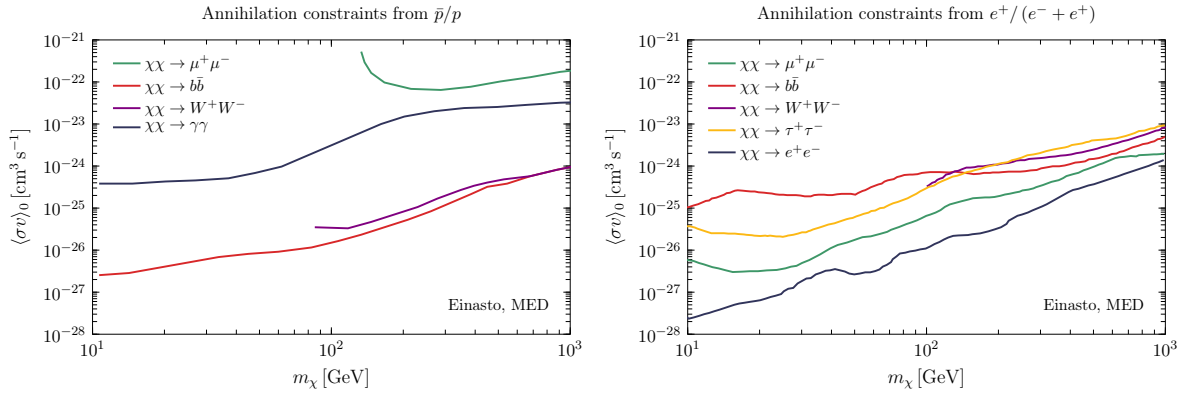

Figure 3.7.: Constraints on the present day annihilation cross section $\langle\sigma v\rangle_0$. Left: Limits obtained using data on the cosmic antiproton flux, adapted from [98]. Right: Limits derived from data on the positron fraction, adapted from [113]. The limits are displayed for several possible annihilation channels. Both measurements were performed by AMS-02 assuming an Einasto profile and the MED propagation profile.

a convolution between the $e^\pm$ number density and the synchrotron emissivity for each given frequency [114–116]. This last term is dependent on the strength of the magnetic fields, such that the total energy radiated is proportional to B^2 [65]. Besides the standard uncertainties when studying indirect detection, those of the Galactic magnetic field have a strong impact when computing the output from synchrotron radiation, jeopardising the robustness of these constraints. In practise, it is possible to estimate the emissivity and astrophysical information into a set of generalised functions characteristic of the energy, position, and frequency of the emission [117]. With an electron-positron injection given by the source in form of equation (3.18), for any specific dark matter model, the radio emission is easily obtainable [116]. The background in radio frequencies is given by two major components, at low frequencies diffuse Galactic synchrotron radiation dominates, whereas at higher frequencies the CMB is the most relevant emission. Furthermore, extended structures called radio loops are present in the radio sky, which also contribute to the background [118]. Dark matter synchrotron radiation has a distinctive intensity spectrum depending on the mass and branching fractions of the annihilation, which can help distinguish the signal from the astrophysical background. This spectrum has a cut-off in frequency dependent on the dark matter mass, this implies that light dark matter does not produce high frequency radiation. The hardness of the spectrum also differs if it was originated by hadronic, leptonic, or vector final states. We present in the left panel of figure 3.8 the upper limits on the annihilation cross section for different dark matter masses obtained from an analysis using the observation of radio waves performed by Planck for different annihilation channels [116]. Finally, we comment that the future radio experiments SKA [119] and LOFAR [120] show promising avenues in radio astronomy.

Neutrinos

Lastly, we summarise the status of dark matter searches using neutrinos as messengers. Since neutrinos are not charged they can propagate almost unhindered from their production position through the Galaxy to Earth, making a directional analysis possible. Experiments like IceCube [122] at the South Pole or Super-Kamiokande [123] in Japan are actively observing the neutrino sky. However, due the fact that neutrinos are only subject to the SM weak

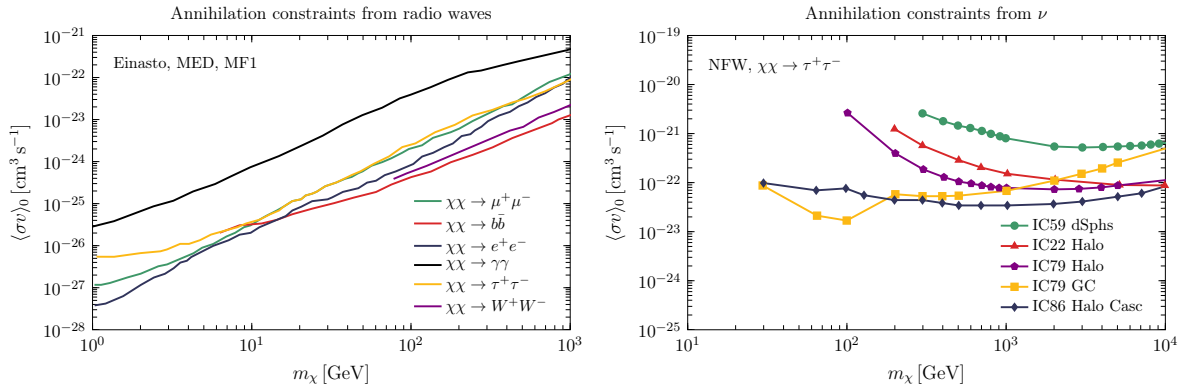

Figure 3.8.: Constraints on the present day annihilation cross section $\langle\sigma v\rangle_0$. Left: Limits obtained from observations of the radio sky for different annihlation channels, assuming an Einasto profile, the MED propagation modeel, and the MF1 magnetic field configuration, adapted from [116]. Right: Limits obtained from measurements of the neutrino flux performed by IceCube on the $\chi\chi \to \tau^+\tau^-$ annihilation channel assuming an NFW profile for different detector configurations, adapted from [121].

interactions, the detection of the uncharged leptons is challenging. The two mentioned experiments rely on the conversion into charged leptons, and the subsequent detection of these mostly through Cherenkov light. On the one hand, electrons need to scatter several times before reaching the Cherenkov threshold. This worsens the angular resolution, still the energy resolution improves as these events are more likely to be fully contained. On the other hand, muon and tauon events are track-like and the effects on the angular and energy resolution are opposite to those of electrons. Upper limits on the velocity averaged cross section of dark matter annihilation obtained by neutrino observations with different detector configurations [121, 124–129] can reach values down to $\langle\sigma v\rangle \simeq 10^{-22}\,\mathrm{cm}^3\,\mathrm{s}^{-1}$, as shown in the right panel of figure 3.8. We also mention another strategy for the study of dark matter using neutrinos coming from the Sun. This strategy aims to detect dark matter particles which were captured in the gravitational field of the Sun after scattering with nuclei and dropping their velocity below the escape velocity. Then, the annihilation of dark matter would produce SM particles, from which only neutrinos could escape from the core of the Sun. In most theories, an equilibrium between capture and annihilation can be achieved and the dark matter density within the Sun—which is significantly larger than that of the solar neighbourhood—remains constant. In this equilibrium, the annihilation rate is no longer dependent on annihilation cross section $\langle\sigma v\rangle$ but on the scattering cross section σ_N with nuclei instead. For this reason, this strategy is compared with direct detection experiments which are discussed in the next section, therefore we postpone the discussion of the results until then.

3.3.2. Direct strategies

We now turn to a complementary strategy to dark matter indirect detection, namely dark matter direct detection. In contrast to the recently discussed indirect searches, the efforts of direct searches aim at measuring an interaction of dark matter itself with an Earth-bound experiment. Within the WIMP paradigm an interaction with SM particles with a rate comparable to that of weak interactions, as illustrated in figure 3.5, is virtually guaranteed. Furthermore, assuming a local dark matter density of $\rho_0 = 0.4\,\mathrm{GeV}\,\mathrm{cm}^{-3}$, a relative velocity of a few $v \simeq 100\,\mathrm{km}\,\mathrm{s}^{-1}$, and

a mass of $m_\chi \simeq 100\,\mathrm{GeV}$, the incident dark matter flux would be $\Phi_\chi \equiv \rho_0\, v/m_\chi \simeq 10^5\,\mathrm{cm}^{-2}\,\mathrm{s}^{-1}$. This implies, for weak-scale cross sections $\sigma \simeq$ pb, about $\mathcal{O}(10)$ scatterings per year for a detector with a target mass of 1 kg. The essence of direct searches is to measure the nuclear recoil of such scatterings [130].

In this section, we introduce the formalities for a quantitative discussion of dark matter searches using this method. Not unlike indirect detection, both fields, astrophysics and particle physics, play a crucial role in this discussion and need to be addressed. We close this section with a discussion on the experimental efforts based on this technique and the present status of their measurements.

The recoil rate and spectrum

When an incident dark matter particle with a mass m_χ and a non-relativistic velocity v interacts with a resting nucleus with mass m_N through an elastic scattering, it transfers a recoil energy given by [131]

$$E_R = \frac{\mu_N^2\, v^2\, (1-\cos\theta)}{m_N}\,, \quad \text{with} \quad \mu_N = \frac{m_\chi\, m_N}{m_\chi + m_N} \tag{3.19}$$

being the dark matter-nucleus reduced mass, and θ the scattering angle in the centre-of-mass frame. For standard WIMP scenarios, typical recoil energies lie within the range $1 - 100\,\mathrm{keV}$. The fact that nuclei are spatially extended results into a loss of coherence. Then, for the correct consideration of the cross section, we introduce form factors $F(E_R)$, as it is customary in nuclear physics and express the cross section as

$$\frac{\mathrm{d}\sigma_N}{\mathrm{d}E_R}(v, E_R) = \frac{m_N}{2\mu_N^2\, v^2}\,\sigma_N\, F^2(E_R)\,, \tag{3.20}$$

where σ_N is the cross section at zero momentum transfer.

For a given experiment, the differential scattering rate per unit mass of the target nucleus requires both the input from astro- as well as from particle physics. That is, the flux of dark matter particles at Earth with a specific local (time-dependent) speed distribution $f(v,t)$ and the cross section for each specific scattering as [132]

$$\begin{aligned}\frac{\mathrm{d}R}{\mathrm{d}E_R}(E_R, t) &= \frac{\rho_0}{m_N\, m_\chi}\int_{v_\mathrm{min}}^{\infty}\mathrm{d}v\, v\, f(v,t)\,\frac{\mathrm{d}\sigma_N}{\mathrm{d}E_R}(v, E_R)\\ &= \frac{\rho_0}{2m_\chi\,\mu_N^2}\,\sigma_N\, F^2(E_R)\times\int_{v_\mathrm{min}}^{\infty}\mathrm{d}v\,\frac{f(v,t)}{v}\,,\end{aligned} \tag{3.21}$$

where $v_\mathrm{min} = \sqrt{m_N\, E_R/\left(2\mu_N^2\right)}$ is the minimal velocity at which an incoming dark matter particle induces a recoil with energy E_R. In the final expression of equation (3.21) we recognise the key required ingredients related to different properties of dark matter, similarly as in the case of indirect detection. Inputs from astrophysics are: the local dark matter density and the velocity distribution; whereas the dark matter-nucleus elastic scattering cross section is dictated by particle physics. We turn to a discussion of the basic concepts of these two contributions.

Cross section

For the exact computation of the WIMP-nucleus cross section, one has to evaluate the corresponding diagrams and take into account the properties of the precise dark matter model

under scrutiny. However, it is possible to generalise the dominant contributions of almost all frameworks into two different kinds of interactions: *spin-dependent* (SD) and *spin-independent* (SI) scatterings [130]:

$$\sigma_N \, F^2(E_R) = \sigma_N^{\mathrm{SD}} \, F_{\mathrm{SD}}^2(E_R) + \sigma_N^{\mathrm{SI}} \, F_{\mathrm{SI}}^2(E_R) \; . \tag{3.22}$$

On the one hand, the SD component interacts with the spin of the target nucleus and is therefore dependent on the total spin of the nucleus. On the other hand, the SI term is sensitive to the amount of nucleons of the target isotope. As a result, experiments are more sensitive to SI interactions. We discuss these two cases separately and express the cross sections $\sigma_N^{\mathrm{SD,SI}}$ in terms of the cross section of a scattering between a WIMP and a free proton σ_p.

SD Scattering Spin-dependent interactions are mediated e.g. by axial-vectors, which couple dark matter to the total spin of the target nucleus J_N with a cross section given by [133]

$$\sigma_N^{\mathrm{SD}} = \frac{\mu_N^2}{\mu_p^2} \left(\langle S_p \rangle + \frac{a_n}{a_p} \langle S_n \rangle \right)^2 \frac{4}{3} \frac{J_N + 1}{J_N} \, \sigma_p^{\mathrm{SD}} \, , \tag{3.23}$$

where μ_p is the reduced mass of the WIMP-proton system (analogous to that of the WIMP-nucleon system, c.f. equation (3.19)), a_p and a_n are, respectively, the effective spin-dependent WIMP-proton and WIMP-neutron couplings, and $\langle S_p \rangle$ and $\langle S_n \rangle$ are the proton and neutron spin expectation values in the nucleus. From this equation, we read that the SD cross section depends critically on the ratio a_n/a_p. However, the sensitivity of the instrument can be improved if the target material of the experiment are isotopes with unpaired nucleons.

SI Scattering On the contrary, interactions mediated by scalars or vectors are spin independent. In this case, dark matter scatters off a nucleus adding coherently contributions of each of the nucleons. The cross section of such an interaction is given by [133]

$$\sigma_N^{\mathrm{SI}} = \frac{\mu_N^2}{\mu_p^2} \left(\frac{Z \, f^p + (A - Z) \, f^n}{f^p} \right)^2 \sigma_p^{\mathrm{SI}} \, . \tag{3.24}$$

Here, Z and A are the standard proton and mass numbers of the target nucleus, f_p and f_n are the effective spin-independent couplings of dark matter to protons and neutrons, respectively. In specific cases, where $f_n/f_p \simeq 1$—for instance the case where the scattering is Higgs mediated—the cross section becomes proportional to A^2. This illustrates the reason why heavy nuclei are favoured as target materials for experiments e.g., germanium or xenon.

Velocity dispersion and annual modulation

There are two astrophysical properties that come into play when computing the recoil rate from equation (3.21): the local dark matter density and velocity distribution. As introduced in the previous section the local dark matter density is estimated to be around $\rho_0 \simeq 0.4\,\mathrm{GeV\,cm^{-3}}$ [75]. On the other hand, the (time-dependent) speed distribution $f(v,t)$ is rather unknown. It is usually assumed to follow a Maxwell-Boltzmann distribution with a most probable velocity $v_0 = 218 - 244\,\mathrm{km\,s^{-1}}$ [80,134], however possible deviations are not excluded and it is important to keep this source of systematic uncertainty in mind. Furthermore, this implies that positive signals in direct detection experiments would provide useful insight towards dark matter density and velocity distributions in the Milky Way.

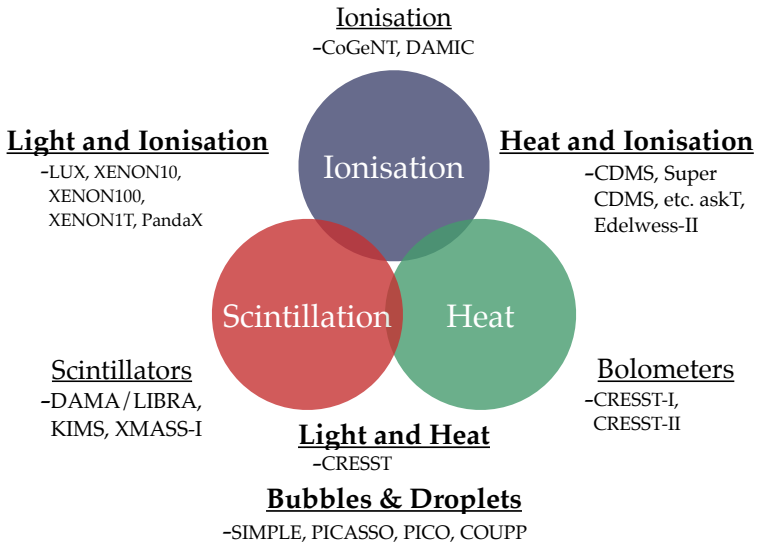

Figure 3.9.: Illustration of the the different direct detection detection methods—scintillation, ionisation, heat, and droplets—employed by different experiments.

The velocity distribution can be decomposed into (Galilean) relative velocities of the Galaxy and Earth:

$$f(\mathbf{v}, t) = f(\mathbf{v}_{\mathrm{G}} + \mathbf{v}_{\mathrm{E}}(t)) \,. \tag{3.25}$$

This parametrisation distinguishes two components: a constant term related to the movement of the Sun around the Galactic centre and a time-dependent term associated to the orbital movement of Earth around the Sun. The latter contribution implies a changing alignment with respect to the dark matter wind. This feature translates into an annual modulation of the recoil rate from equation (3.21), an effect that can be parametrised as [135]

$$\frac{\mathrm{d}R}{\mathrm{d}E_R} = S_0(E_R) + S_m(E_R)\,\cos 2\pi\,(t - t_0)\,, \tag{3.26}$$

where S_0 is the time-averaged event rate, S_m is the modulation amplitude, and t_0 is the phase at which Earth moves with maximum speed against the dark matter wind. Although the fraction S_m/S_0 is usually of a few percent, this modulation is a unique property of WIMPs and can be used as a discrimination technique between dark matter and background.

Experiments are affected by differing velocity distributions in a non-universal way, giving rise to a large set of uncertainties when studying direct detection. The possibility of halo-independent methods as been proposed [136–139], which analyses data from the direct detection experiments without assuming any velocity distribution.

Experimental efforts

Measuring a nuclear recoil originated by a WIMP scattering off a nucleus would be clear empirical evidence for dark matter. Consequently, several international collaborations built experiments designed to detect these interactions. However, as stated previously, the weak interactions predict a low event rate. A large background, exceeding the expected signal by

orders of magnitude, makes this experimental search highly challenging. Effects released by cosmic rays constitute a substantial component, thus the experiments are usually located in underground facilities. Furthermore, the building and surrounding materials of the experiment have to be meticulously controlled, as radioactivity is also a substantial source of background.

Detection techniques

The measurement of these nuclear recoils can be carried out by observing different effects produced by them. Dark matter can interact with nuclei either elastically, allowing experiments to measure the recoil; or inelastically, when dark matter interacts with the orbital electrons or excites the nucleus. The search strategies usually fall into one of three categories: scintillation, ionisation and heat. Scintillation experiments measure the light emitted by the interaction, ionisation experiments look for ions produced by the scatterings, and heat experiments aim to detect small temperature fluctuations caused by incident WIMPs (usually of order μK). Furthermore, some experiments use simultaneously two detection methods in order to strengthen their discrimination power. To date, a large set of collaborations operate direct detection experiments like the scintillation detectors DAMA/LIBRA [140], KIMS [141], and XMASS-I [142]; the ionisation detectors DAMIC [143] and CoGeNT [144]; and the bolometers (heat) CRESST-II [145,146]. As well as XENON [147–149], LUX [150–152], and PandaX [153], which use scintillation and ionisation techniques; CRESST-II [145,146] CRESST [154] which uses heat and ionisation techniques; and finally heat and ionisation bolometers like SuperCDMS [155], CDMSlite [156], and EDELWEISS-II [157]. Finally, we mention superheated droplet detectors like SIMPLE [158], PICASSO [159], PICO [160], and COUPP [161], which use a technique similar to the bubble chambers used around decades of 1950 and 1960. A schematic arrangement of some of the direct detection experiments according to their detection methods is shown in figure 3.9.

Signals and upper limits

Dark matter direct detection has been source of controversy for a long time. On the one hand, some experiments claim to have measured an interaction between WIMPs and the target nuclei of the experiments. Most significant is the 9.3σ claim by the DAMA collaboration of the discovery of an annual modulation, over fourteen annual cycles (1995-2009) [140]. Experiments such as CDMS-Si [163] and CoGeNT [164] have also published results with less significance, claiming the measurement of phenomena of dark matter origin. Furthermore, the phase of the DAMA signal is in concordance to that attributed to the dark matter wind. On the other hand, results from other experiments exclude the parameter space for the interpretation of these signals, giving rise to tensions with the former claims. We display in figure 3.10 a summary of the limits set by different collaborations as well as the regions of the parameter space favoured by the DAMA measurements. In the same figure, we also depict the limits obtained from observations of neutrinos with IceCube, assuming dark matter being captured in the core of the Sun [162] with the method introduced in section 3.3.1. The main annihilation channel assumed for these results are $\chi\chi \to b\bar{b}$ (soft), and $\chi\chi \to \tau^+\tau^-$ for $m_\chi < m_W$ and $\chi\chi \to W^+W^-$ for $m_\chi > m_W$. The strongest limits obtained with this method are on the SD scattering cross section with protons σ_p^{SD} due to the large amount of hydrogen nuclei in the Sun.

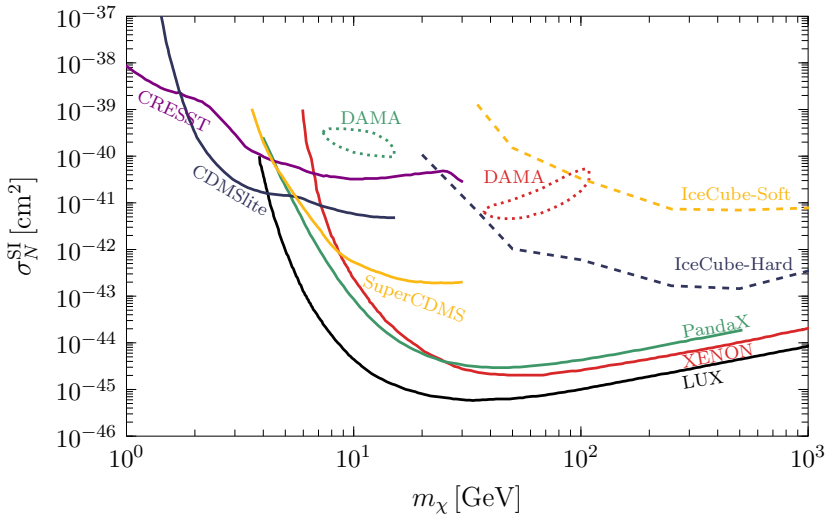

Figure 3.10.: Summary of the experimental status on the spin-independent scattering cross section σ_M^{SI} against the dark matter mass m_χ. The upper limits on the cross section are shown (solid) as obtained using data of different experiments. The favoured parameter space regions for the annual modulation as observed by DAMA are also shown (dotted). Finally, the limits from indirect searches from neutrinos from the Sun are presented as well (dashed). For details and references see text.

Part II.

Gamma-rays as messengers for indirect detection

4. Gamma-rays in astroparticle physics

In this chapter, we discuss high-energy photons or gamma rays within the context of astroparticle physics and dark matter. That is, astrophysical sources yielding a large flux, dark matter as the origin of gamma-rays, and some gamma-ray observatories. In figure 4.1 we present an all-sky survey of the gamma-ray sky performed by the Fermi-LAT observatory, after an observation time of five years for photons with energies $E_\gamma > 1\,\mathrm{GeV}$. This map is dominated by astrophysical sources, however it is possible for a dark matter signal to be concealed within. First, we discuss the main astrophysical sources for gamma-rays, then we summarise

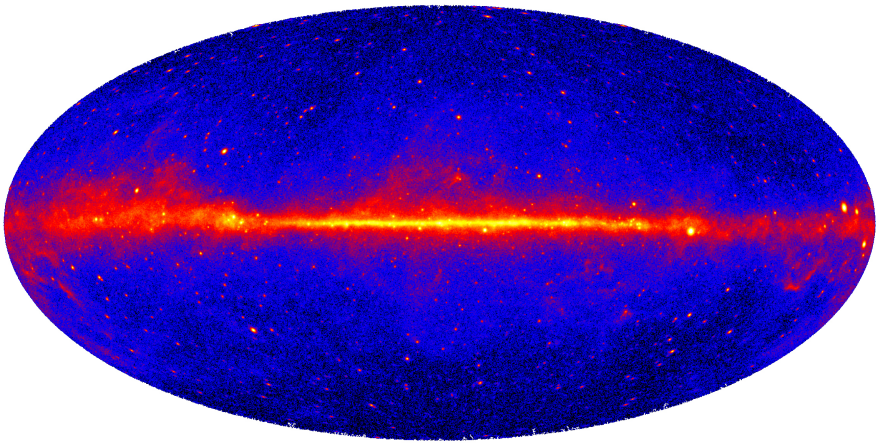

Figure 4.1.: All-sky gamma-ray view for energies larger than $E_\gamma > 1\,\mathrm{GeV}$ based on five years of data taking with the Fermi-LAT telescope. Brighter colours indicate a larger gamma-ray flux. Image credit NASA/DOE/Fermi-LAT collaboration [165].

the method and status of dark matter indirect detection using gamma-rays, and finally we give a brief overview of the experiments.

4.1. Astrophysical gamma-rays

In this section, we discuss astrophysical sources of gamma-rays, which are, to date, the only proven sources of gamma-rays in contrast to other putative sources like dark matter. We can classify these sources into three distinctive categories:

Diffuse Galactic sources. First, we introduce the category with the largest contribution to the total gamma-ray flux: the diffuse Galactic emission. This emission is mainly produced via three effects: inverse Compton scattering (ICS), bremsstrahlung, and π^0 decay. These are the result of cosmic-ray spallation processes with interstellar matter (ISM) or high-energy interactions with the CMB. Since this emission originates from the interactions of ordinary matter, its brightest component is located on the galactic plane and it dims for ascending latitudes.

Point sources. Second, sources, the angular extension of which is smaller than the resolution of the instrument, also contribute to the map. These sources are clearly distinguishable in the all-sky gamma-ray map presented above as bright isolated pixels, hence the name point sources. The main contributions are from active galactic nuclei (AGNs) and pulsars.

Diffuse gamma-ray background. Lastly, we address the isotropic gamma-ray emission populating the full sky. Although its precise nature is not fully understood, it can be interpreted as the cumulative emission of extragalactic sub-threshold sources e.g., Blazars, AGNs, star-forming galaxies, and possibly dark matter. This emission is the remaining contribution of the gamma-ray sky map after the substraction of the two former foregrounds. This contribution is omnidirectional, but not necessarily isotropic.

We explain the first two sources in more detail, while leaving the faint extragalactic diffuse gamma-ray background out of the discussion, since it does not contain substantial information for the pursuits of this work.

4.1.1. Point sources

We introduce some astrophysical phenomena that contribute to the gamma-ray sky as point sources. We remain concise and refer to e.g. [166] for a more comprehensive overview.

Active galactic nuclei

In some cases, galaxies are able to host a super-massive black hole in its core, with masses ranging between $10^5 - 10^9 M_\odot$. These black holes are constantly fuelled by accretion disks, radiating large amounts of energy in form of photons with different wavelengths, among other particles. These objects are called active galactic nuclei, and contribute largely to the total number of point sources. A characteristic property of AGNs is an emission jet pointing out from the poles of the galaxy, where the photons with highest energy are radiated. Therefore, AGNs are classified according to the observation angle in relation to the jets: Blazars are AGNs the jets of which point directly at us (head-on), Seyfert galaxies and quasars lay at an angle towards Earth, and radio galaxies have their jets pointing perpendicularly (edge-on). Since the brightest source of gamma-ray emission are the jets themselves, Blazars are the most relevant when discussing their contribution to the high energy gamma-ray sky. There are two leading models for the emission mechanism: leptonic and hadronic processes. In both cases the low-energy gamma rays are emitted via synchrotron radiation. In the leptonic case, high-energy gamma rays are produced via ICS using the synchrotron emission as seed photons; whereas in the hadronic case neutral π mesons decay into photons and give rise to this emission.

Pulsars

Under certain conditions, the death of a star and the subsequent gravitational collapse may lead to the formation of a neutron star. These are small, highly dense, and highly magnetised bodies made up almost entirely out of neutrons. Due to conservation of angular momentum, some neutron stars rotate at very high velocities, known as pulsating rotating stars or pulsars. The gamma-ray emission mechanism is not yet fully understood. However, most of the existing models agree that high-energy photons within the magnetosphere produce an $e^\pm$ pair which in turn emit a second generation of photons via synchrotron radiation. This process is repeated until the photons fail to meet the energetic requirements to pair produce and are able to escape.

The source of emission is located at the magnetic poles of the star, which are at an off set to the geographical poles. This leads to the characteristic periodic gamma-ray emission, which enabled the Fermi collaboration to identify 117 pulsars from their observations [167, 168].

4.1.2. Galactic diffuse emission

Galactic diffuse emission is the most luminous source of high-energy photons, stemming mainly from the galactic disk, clearly distinguishable in the Fermi-LAT map, from figure 4.1. This component is originated in high-energy spallation processes: cosmic rays collide with ISM producing a large amount of particles which are subject to hadronisation, and decay processes. Among others, neutral π mesons are produced which decay dominantly into high-energy photons. Finally, the remaining charged stable particles diffuse in the galaxy and are subject to several possible interactions e.g., bremsstrahlung and ICS. Let us discuss the main components of the diffuse gamma-ray sky separately in a compact manner. This discussion is based on [166, 169, 170].

Pion decay

Pions are a natural product of all hadronisation processes. Collisions between high-energy protons and ISM produce a large amount of π mesons, $\pi^{\pm}$ and π^0. The charged $\pi^{\pm}$ states decay dominantly into leptons which in turn emit photons in form of bremsstrahlung as discussed later on. On the other hand, the neutral mesons π^0 decay with a branching fraction $\mathrm{BR}\left(\pi^0 \to \gamma\gamma\right) \simeq 0.988$ into photons, providing a large contribution to the total gamma-ray flux. In the rest frame, both photons are emitted with the same monochromatic spectrum, since it is a diphoton emission, with an energy $E_\gamma \simeq 70\,\mathrm{MeV}$. However, the pions have non-zero velocity and the emission has to be boosted correspondingly. Considering a pion source function $Q_{\pi^0}(E_\pi)$ the gamma-ray contribution from π^0 decay is given by

$$q_{\pi^0}(E_\gamma) = 2\int_\epsilon^\infty \mathrm{d}E_\pi\, Q_{\pi^0}(E_\pi)\, \left(E_\pi^2 - m_\pi^2\right)^{-\frac{1}{2}}\,, \tag{4.1}$$

where m_π is the pion mass and $\epsilon = E_\gamma + \left(m_\pi^2/\left(4E_\gamma\right)\right)$ is the minimal energy for a pion to emit a photon with energy E_γ. In the present day, the Universe is completely transparent to photons at these energies, therefore the differential flux at Earth is obtained by performing a line-of-sight integral

$$\frac{\mathrm{d}^2\phi_\gamma^{\pi^0}}{\mathrm{d}E_\gamma\,\mathrm{d}\Omega} \equiv \frac{1}{4\pi}\int_{\mathrm{los}} \mathrm{d}s\, q_{\pi^0}(E_\gamma, s)\,, \tag{4.2}$$

assuming an isotropic velocity distribution of pions.

Bremsstrahlung

In the previous chapter, we briefly addressed the propagation of charged particles through the Galactic magnetic fields to which bremsstrahlung is one of the main effects that lead to energy losses. During this diffusion, charged cosmic rays are subject to interactions with the ISM and emit bremsstrahlung (German for braking radiation). There are two different contributions from bremsstrahlung: the one originated from thermal electrons with typical energies in the X-ray range, and the one originated from non-thermal relativistic electrons, usually from supernova remnants (SNR). Under the assumption of an electron number density

described by a power-law $\mathrm{d}N_e/\mathrm{d}E_e = \kappa\, E_e^{-\nu}$, with $\nu \simeq 1.5$, we obtain a source function for photons radiated as bremsstrahlung

$$q_{\mathrm{br}}\,(E_\gamma) = \int_{E_\gamma}^{\infty} \mathrm{d}E_e\, \frac{\alpha\, n}{E_\gamma} \kappa E_e^{-\nu} = \frac{\alpha\, n\, \kappa}{\nu - 1}\, E_\gamma^{-\nu}\,, \tag{4.3}$$

where α is a parameter depending on the chemical properties of the ISM, and n is the number density of interacting nuclei. The lower integration bound is, as in the case of pion decay, due to kinematical reasons. Again, we perform a line-of-sight integral in order to compute the differential photon flux at Earth

$$\frac{\mathrm{d}^2\phi_\gamma^{\mathrm{br}}}{\mathrm{d}E_\gamma\, \mathrm{d}\Omega} \equiv \frac{1}{4\pi} \int_{\mathrm{los}} \mathrm{d}s\, q_{\mathrm{br}}(E_\gamma, s)\ . \tag{4.4}$$

Inverse Compton scattering

Finally, we discuss inverse Compton scattering as a gamma-ray source. As the name suggests, this effect involves the energy transfer between an electron and a photon $e\gamma \to e\gamma$. Here, an (ultra)relativistic electron—usually produced at SNR—scatters off a low-energy photon resulting in a low-energy electron and a photon in the MeV-GeV range. The low-energy photons are provided by the interstellar radiation field (IRF), the main sources of which are: CMB photons, infrared light from the galactic dust (IR), and starlight (SL). The total energy loss of electrons due to ICS in the Thomson limit, i.e. $\gamma\, E_\gamma \ll m_e$, is given by [171]

$$\frac{\mathrm{d}E}{\mathrm{d}t} = \frac{4}{3} \sigma_{\mathrm{T}}\, u_{\mathrm{bath}}\, \beta^2\, \gamma^2\,, \tag{4.5}$$

where σ_{T} is the Thompson scattering cross section, β and γ are the Lorentz boost factors from the rest frame of the electron to the lab frame, i.e. $E_e = \gamma\, m_e$ and u_{bath} is the energy density of the photon bath. Furthermore, a kinematical analysis shows that a photon with energy E'_γ is scattered off by an electron with energy E_e to an energy

$$E_\gamma = \frac{4}{3} \gamma^2\, E'_\gamma\,. \tag{4.6}$$

This means that the gamma-ray spectrum from ICS depends highly on the low energy photon bath, which can be described by the three components previously mentioned as black-body spectra with temperatures $T_{\mathrm{CMB}} \simeq 2.7255\,\mathrm{K}$, $T_{\mathrm{IR}} \simeq 40\,\mathrm{K}$, and $T_{\mathrm{SL}} \simeq 3500\,\mathrm{K}$—arguing in favour of the usage of the Thompson limit for this description. The ICS source function is obtained as a convolution between the electron number density $\mathrm{d}N_e/\mathrm{d}E_e = \kappa\, E_e^{-\nu}$ and the photon emission power [65]

$$q_{\mathrm{ICS}}\,(E_\gamma) = \int_{m_e}^{\infty} \mathrm{d}E_e\, \mathcal{P}_{\mathrm{ICS}}(E_\gamma, E_e)\ \kappa E_e^{-\nu}\,, \tag{4.7}$$

where $\mathcal{P}_{\mathrm{ICS}}(E_\gamma, E_e) = \sum_i \mathcal{P}^i_{\mathrm{ICS}}(E_\gamma, E_e)$ is the differential power emitted as photons from ICS with $i = \mathrm{CMB}, \mathrm{IR}, \mathrm{SL}$. As usual the differential flux is obtained as

$$\frac{\mathrm{d}^2\phi_\gamma^{\mathrm{ICS}}}{\mathrm{d}E_\gamma\, \mathrm{d}\Omega} \equiv \frac{1}{4\pi} \int_{\mathrm{los}} \mathrm{d}s\, q_{\mathrm{ICS}}(E_\gamma, s)\ . \tag{4.8}$$

We present the resulting Galactic diffuse emission considering the three components in figure 4.2.

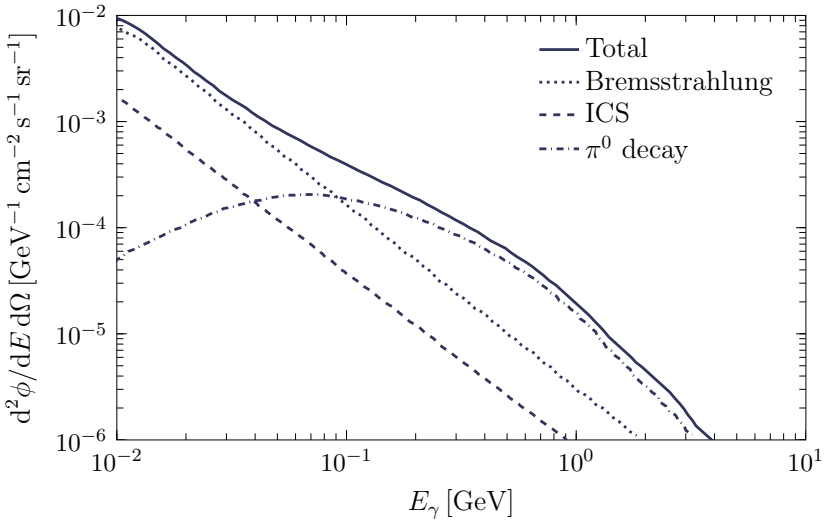

Figure 4.2.: Gamma-ray flux from different sources as observed at Earth. The contributions of ICS (dashed), bremsstrahlung (dotted), and π^0 decay (dotdashed) are shown separately as well as the total flux (solid). The scale of the y-axis is for an arbitrary region and varies depending on the direction of observation. Figure adapted from [170].

4.2. Dark matter indirect detection using gamma-rays

In addition to the discussion on dark matter indirect detection from section 3.3.1, we discuss gamma-rays in the context of indirect searches. Since dark matter is not electrically charged, a direct coupling to photons is not allowed. However, as we argued in the context of indirect searches with radio waves, there are several ways dark matter could produce a sizeable photon flux. Furthermore, gamma rays do not suffer any diffusion effects after their production through the Galaxy and travel in a straight line to Earth. This provides avenues to studies not only on the flux but also on the morphology of the gamma-ray emission. We discuss two separate types of gamma-ray emission from dark matter: direct and secondary emission.

4.2.1. Prompt emission and spectral features

Let us start the discussion with photons emitted directly from dark matter annihilation—usually called prompt emission. Notice that dark matter decay is also a possible source of prompt gamma-rays, however, since the discussions are fairly similar, we focus solely on annihilating dark matter. The path a photon transits between its origin and the telescope is a straight line, which enables the direct derivation of the incoming flux from the emission source, more precisely the sources along the line of sight. We write the differential flux of photons from an angular direction $\mathrm{d}\Omega$ produced by the annihilation of dark matter as

$$\frac{\mathrm{d}^2\Phi_{\mathrm{ann}}}{\mathrm{d}E_\gamma\,\mathrm{d}\Omega} = \frac{1}{8\pi\,\kappa\,m_\chi^2}\sum_c \langle\sigma v\rangle_0^c\,\mathrm{BR}_c\,\frac{\mathrm{d}N^c}{\mathrm{d}E_\gamma}\int_{\mathrm{los}}\mathrm{d}s\,\rho_\chi^2\,, \tag{4.9}$$

where $\kappa = 1$ in the case of self-conjugated particles and $\kappa = 2$ otherwise, $\mathrm{d}N^{\mathrm{c}}/\mathrm{d}E_\gamma$ is the photon spectrum of a channel c produced by an annihilation with a present-day velocity averaged cross section $\langle\sigma v\rangle_0^c$ and a branching ratio BR_c, and ρ_χ the dark matter distribution profile. This equation is one of the main tools we will use when studying prompt gamma-rays from dark

matter. In contrast to other channels, the incoming flux can be clearly splitted into two terms. One term encodes the astrophysical information of dark matter called the J-factor given by the line-of-sight integral

$$J_{\rm ann} \equiv \int_{\rm los} {\rm d}s\, \rho_\chi^2(\mathbf{r}(s)) \ . \tag{4.10}$$

Since instruments have a finite angular resolution, it is useful to define an averaged J-factor of a patch with solid angle $\Delta\Omega$ as $\overline{J}_{\rm ann} \equiv (\Delta\Omega)^{-1} \int_{\Delta\Omega} {\rm d}\Omega\, J_{\rm ann}$. The rest of equation (4.9) describes the microscopic properties of dark matter annihilation and the emission of photons

$$K(E_\gamma) = \frac{1}{8\pi\,\kappa\, m_\chi^2}\, m_\chi \sum_c \langle\sigma v\rangle_0^c\, {\rm BR}_c\, \frac{{\rm d}N^c}{{\rm d}E_\gamma} \, . \tag{4.11}$$

Optical depth

On its path to Earth, gamma-rays can be absorbed by the extragalactic background light due to possible pair-production processes $\gamma\gamma \to e^+e^-$. For this reason it is pertinent for us to review the calculation of the optical depth (see e.g. [172, 173]). First indications of this phenomenon were apparent right after the discovery of the CMB [174–176]. Where the mean free path of photons reaches a minimum of $D \simeq 8\,{\rm kpc}$ for photon energies near $E_\gamma \simeq 2\,{\rm PeV}$. Standard sources for background photons are visible, infrared, and ultraviolet light, CMB photons, and radio waves, with a relevance depending on the energy of the primary photon. Since we are exclusively interested in photons from the local universe—i.e. no redshift ($z = 0$)—there is no necessity to adjust the wavelength of gamma-rays to the expansion of the Universe. The optical depth $\tau(E_\gamma, s)$ for a photon with energy E_γ produced at a distance s is then calculated by convolving the photon number density of the background photons and the $e^\pm$ pair-production cross section $\sigma_{\gamma\gamma}$

$$\tau(E_\gamma, s) \equiv \frac{1}{2} \int_{-1}^{1} {\rm d}\cos\theta\ (1-\cos\theta) \int_{E_{\rm min}}^{\infty} {\rm d}E'_\gamma\, n\big(E'_\gamma, s\big)\ \sigma_{\gamma\gamma}\big(E_\gamma, E'_\gamma, \theta\big) \ , \tag{4.12}$$

where E'_γ is the energy of the background photons, θ is the collision angle between photons, and $E_{\rm min}$ is the threshold energy for pair production. Finally, the effects of the optical depth are accounted by the inclusion of an attenuation factor $\propto e^{-\tau(E_\gamma, s)}$ for photons with an energy E_γ in the formulation of the J-factor

$$J^\tau_{\rm ann}\,(E_\gamma) = \int_{\Delta\Omega} {\rm d}\Omega \int_{\rm los} {\rm d}s\, e^{-\tau(E_\gamma, s, \Omega)}\, \rho^2 \, . \tag{4.13}$$

Gamma-ray fluxes

In the next chapters, we focus on the gamma-ray fluxes produced by dark matter annihilations. Therefore, we discuss the contributions from the term $K(E_\gamma)$ in more detail. Dark matter annihilates into several primary channels mainly consisting of a pair of leptons, quarks, Higgs particles, gluons, electroweak gauge bosons, or gamma-rays. However, the final output of these channels is a product of parton showers and hadronisation, yielding fluxes of electrons, neutrinos, protons, and photons[1]. For the estimation of the output of an annihilation it is customary to use Monte Carlo simulation programs, such as Pythia [177] or Herwig [178].

[1] Deuterons are also a possible final state from dark matter annihilations, however, since these are less common products, we leave them out of this discussion.

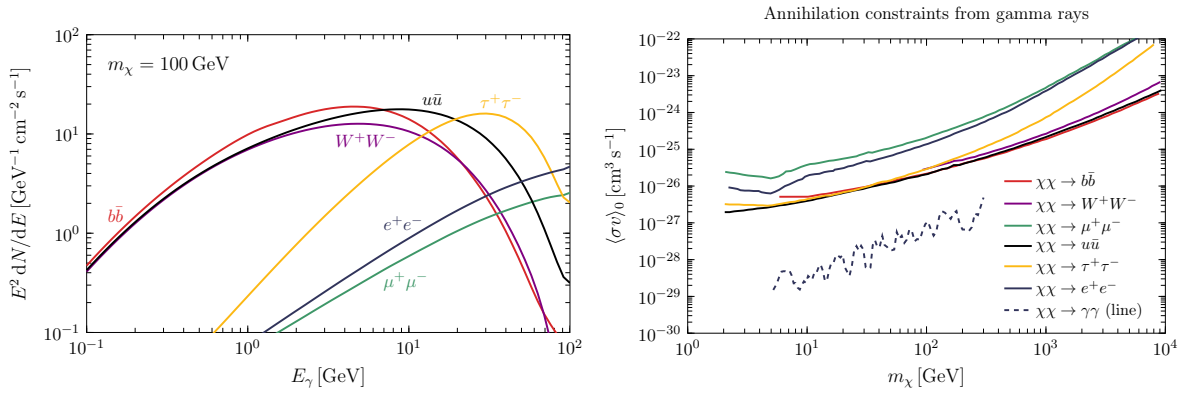

Figure 4.3.: Left: Gamma-ray flux from the prompt emission from annihilation of dark matter with mass $m_\chi = 100\,\mathrm{GeV}$ into different primary channels. Extracted from the tools provided in [65, 179]. Right: Upper limits on the velocity averaged annihilation cross section from observations by the Fermi-LAT on 15 dSph for the same annihilation modes depicted in the left panel, adapted from [180].

Here, we focus on the photons emitted from such processes. We show in the left panel of figure 4.3 a sample gamma-ray output of the annihilation of a $m_\chi = 100\,\mathrm{GeV}$ WIMP into different primary channels, computed using tools provided in references [65, 179]. These fluxes include only prompt gamma-rays, that is they do not include photons emitted by final-state charged particles, three-body annihilations or radiative hadron decays. In the right panel of figure 4.3, we present the corresponding upper limits on the annihilation cross section obtained from the estimation of these fluxes and the observation of dwarf spheroidal galaxies (dSph) for the same channels [181]. This work in particular exploits the directional information of gamma-rays. Dwarf galaxies are celestial bodies which are strongly dominated by dark matter. Therefore, from the non-observation of gamma-ray fluxes from dSph it is possible to derive stringent limits on the dark matter annihilation cross section. It is remarkable that almost every annihilation channel is able to exclude thermal WIMPs with light masses, recalling the target value from equation (3.11). With next generation gamma-ray telescopes in development, high-energy astronomy promises an exciting future.

Recent observations of GC point towards a possible excess in the gamma-ray flux concealed in this region [182–187]. It is possible to interpret this signal as prompt photons from dark matter annihilations, as the morphology of this excess is in agreement with that expected from a contracted NFW profile. Furthermore, depending on the primary channel and on details of the dark matter model, possible masses lay within the regime $m_\chi \simeq 10 - 200\,\mathrm{GeV}$. If indeed the GeV excess from the GC is of dark matter origin, a similar phenomenon should be observed at dSph galaxies, however recent studies do not show signs of such a signal [181].

Spectral features

Another strategy relying on the emission of prompt gamma-rays is the search for gamma-ray spectral features in the sky. These originate in dark matter annihilations and have a characteristic spectrum which makes them particularly easy to distinguish from the otherwise smooth background [188–190]. Furthermore, these features cannot be mimicked by any known astrophysical source, thus being the clearest possible signals which could be attributed to dark matter. The most well known example is the emission of monochromatic photons, usually

via $\chi\chi \to \gamma\gamma$, a processes that suffers a loop suppression since dark matter is not electrically charged. Depending on the specific model, the magnitude of the suppression varies, still due to the extra vertices a factor of $\alpha_{\rm em}^2$ is ensured. Due to their shape—a delta function smeared by the resolution of the instrument—these signals are called gamma-ray lines, which have been object of several studies. Several collaborations [180, 191–194] have performed an active search for these features and, in light of their absence, derived constraints on the annihilation cross section of dark matter. In the right panel of figure 4.3, in addition to the results from other prompt gamma-ray emission, we show the limits derived by the Fermi collaboration [180]. This analysis relies largely on directional analyses of photon emission, and the selection of optimal sky regions in order to maximise the signal-to-noise (S/N) ratio. Finding the best target region is not a trivial task, however it could prove to be a key aspect in the search for gamma-ray spectral features. In fact, some authors hinted the discovery of a line-like signal in the Fermi-LAT data [195, 196]. However, additional data has weaken the claim dropping the significance of this signal [180]. Other possible spectral features have also been studied, such as virtual internal bremsstrahlung [197–199] or gamma-ray boxes and triangles [9, 200]. The former arises from the hard emission of a photon from a two-to-three annihilation and the latter is the product of cascade processes, which shall be discussed extensively in chapters 5, 6, and 7.

4.2.2. Gamma-rays as secondaries

Photons that are not emitted promptly from dark matter annihilations are called secondaries. We already discussed some dark matter secondary emission in the context of indirect detection with radio waves. Secondary gamma-rays are produced via the same three effects we discussed previously—π^0 decay, bremsstrahlung, and ICS—employing cosmic rays originated in dark matter annihilations instead. For this purpose we cast the source functions from equations (4.1),(4.3), and (4.7), and replace the astrophysical inputs $Q_{\pi^0}(E_\gamma)$ and $\mathrm{d}N_e/\mathrm{d}E_e$, with those of dark matter. In contrast to prompt emission, a clear distinction between astrophysical and microscopical contributions is not possible, since the emissivity of secondary gamma-rays depends on both. This can lead to uncertainties on the estimation of the gamma-ray flux.

4.3. Gamma-ray telescopes

This work discusses and analyses dark matter using observations of gamma-rays. Therefore, we devote this section to an introduction of gamma-ray observatories. We focus on the three telescopes that are used in the following chapters: The spaceborne Large Area Telescope aboard the Fermi satellite (Fermi-LAT), the High Energy Stereoscopic System (H.E.S.S.), and the future Cherenkov Telescope Array (CTA), currently in pre-construction phase.

4.3.1. Fermi Large Area Telescope

The Fermi satellite was launched in 2008, with an expected mission duration of up to ten years [201,202]. The Fermi-LAT is a space-borne gamma-ray detector able to scan the complete sky for photons with energies between 20 MeV and 500 GeV. At these energies, the main interaction mode of photons with matter is pair production $\gamma\gamma \to e^+e^-$. It is via this process that the instrument is able to observe gamma rays, using the information obtained from four main subsystems. The purpose of the *tracker* is twofold, it reconstructs the incident direction of the gamma ray using silicon tracking devices and employs tungsten foils as target material

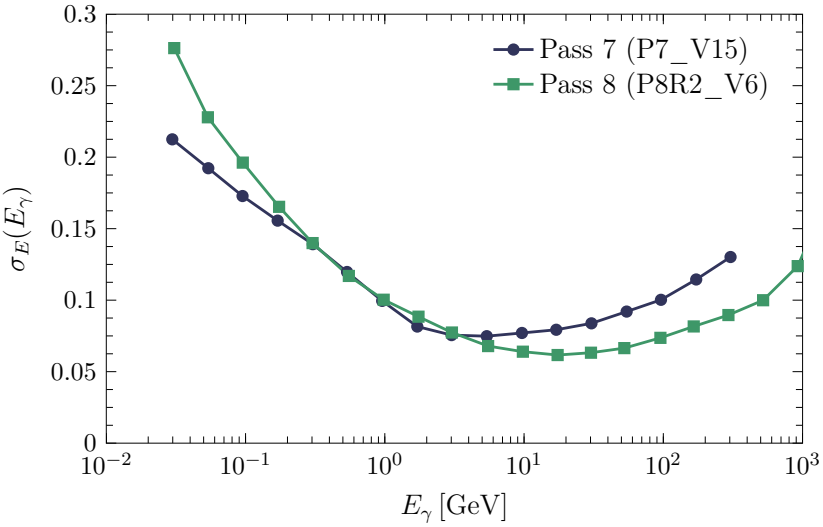

Figure 4.4.: Resolution from the Fermi-LAT instrument using the IRFs P7_V15 (green squares) and P8R2_V6 (blue dots) as a function of the energy.

for the pair production. The energy deposition (of the $e^{\pm}$ pair) is measured by the *calorimeter*, a CsI scintillator placed below the tracker. The large flux of cosmic rays could induce signals misidentifying them as photons. The *anticoincidence detector* and the *data acquisition system* are able to discriminate these from true gamma rays with a rejection efficiency of 99.97%. The Fermi-LAT is currently one of the most important gamma-ray observatories and has a large list of accomplishments: the discovery of a large set of pulsars [167, 168], the discovery of the so-called Fermi bubbles [203]—two gamma-ray emitting lobes extending from the GC to higher latitudes—and the confirmation of the rise of the positron fraction [106], among others. The mapping of the acquired information into detected photon events is performed by the instrument response functions (IRF). These algorithms interpret the data acquired by the hardware of the instrument, reconstruct the events, discriminate backgrounds, and select events according to their quality. Fermi data can be analysed with multiple IRFs allowing a certain flexibility for different studies. The current data is processed using the Pass 8 event-level analysis. We use in latter analyses two different IRFs, namely Pass 7 Version 15 (P7_V15) and Pass 8 Release 2 Version 6 (P8R2_V6), therefore we present in figure 4.4 the energy resolution for these two IRFs.

4.3.2. High Energy Stereoscopic System

The H.E.S.S. telescope is an Earth-bound gamma-ray telescope based in Namibia [204, 205]. This observatory is an imaging atmospheric Cherenkov telescope (IACT), i.e. it observes the Cherenkov light emitted by high-energy charged particles using air as dielectric medium. High energy photons collide with the atmosphere generating cascades of relativistic charged particles, however charged cosmic rays yield to almost identical Cherenkov light producing a substantial part of the background. The detector array consists of four telescopes, built in 2002 (Phase I) and a larger fifth telescope finished in 2012 (Phase II). In contrast to Fermi-LAT, H.E.S.S. is able to point at specific targets, which makes the observation time dependent on the observation angle; regions of special interest, such as the GC, are subject to more extensive observations. The field of view of the instrument has a diameter of 5° and covers an effective area larger than

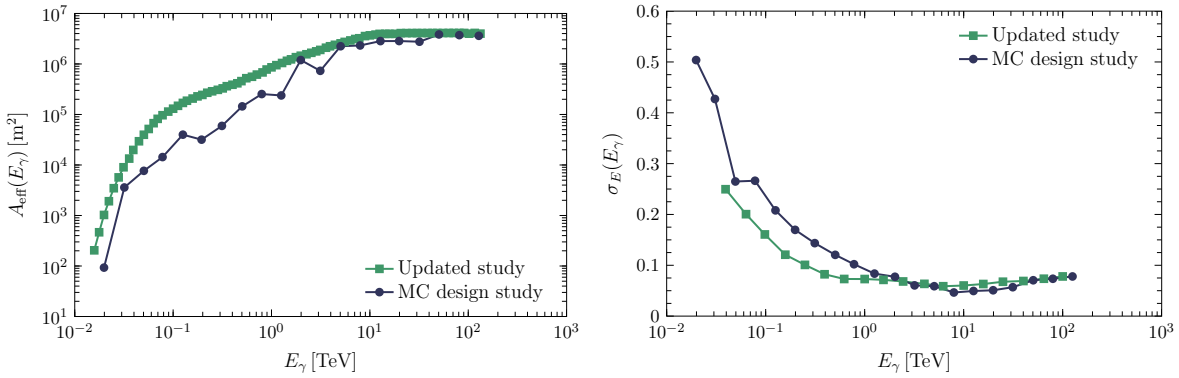

Figure 4.5.: Projected effective area $A_{\rm eff}$ (right) and resolution σ_E (left) of CTA for the southern candidate array I using the baseline MPIK analysis. The blue dots correspond to the Monte Carlo study from reference [208], and the green squares to the updated performance, made available online in [209].

$10^5\,\mathrm{m}^2$. H.E.S.S. is able to investigate photon energies from $\simeq 10\,\mathrm{GeV}$ up to $\simeq 10\,\mathrm{TeV}$. For the interest of this work, the resolution adopted is a log linear variation from 17% at 500 GeV down to 11% at 10 TeV, in line with reference [191].

4.3.3. Cherenkov Telescope Array

Finally, we introduce CTA, a next generation IACT which is expected to start data taking by 2019 [206, 207]. This observatory is currently at a pre-construction phase and will step into the pre-production phase in early 2017. The CTA instrument will be constructed in the northern (Canary Islands, Spain) and in the southern hemisphere (Atacama, Chile), allowing for a better full-sky coverage. According to the current status of the design the north site will consist of 4 large-size and 15 medium-size telescopes covering a total area of $\simeq 0.4\,\mathrm{km}^2$; whereas the south site will consist of 4 large-size, 24 medium-size, and 72 small-size telescopes covering a total area of $\simeq 4\,\mathrm{km}^2$ [207]. However, the final design is still open to changes, therefore the performance of the instrument is subject to recurring upgrades as the analysis algorithms improve and the final construction set-up is fixed, therefore we focus on a specific performance which shall be used in later chapters.

Performance of the instrument

For the purposes of this work, the performance of CTA is modelled after detailed Monte Carlo design studies by the CTA Constortium published in [208]. More precisely, we investigate the southern candidate array I—consisting of 3 large-size, 18 medium-size and 56 small-size telescopes—which is a well-studied and balanced configuration, and use the baseline MPIK analysis. We use the effective area $A_{\rm eff}$ and the energy resolution σ_E depicted in figure 4.5. The energy range covered by the telescope is expected to be remarkably extensive, from 10 GeV to about 100 TeV. As discussed previously, the gamma-ray detection method of IACTs observes the light emitted from showers generated by cosmic photons, which is (almost) indistinguishable from that of cosmic electrons. The photon acceptance is taken to be $\epsilon_\gamma = 1$, therefore the electron acceptance is $\epsilon_e = 1$ as well, since the Cherenkov light of both cases is almost indistinguishable. On the other hand, the proton acceptance is energy dependent and lies in the range $\epsilon_p = 0.01 - 0.20$. Finally, we comment that during the publication process of the original

work this thesis is based on (reference [8]) an updated study on the expected performance of CTA was made available [209]; improving the effective area and energy resolution, as shown in figure 4.5, as well as changing the range of the proton acceptance down to $\epsilon_p = 0.001 - 0.02$. These updates were considered in the following chapters in addition to the analysis done with the design presented in [208].

Together with other next generation gamma-ray telescopes such as the High Altitude Water Cherenkov Experiment (HAWC) [210] or the Hundred Square-km Cosmic Origin Explorer (HiSCORE) [211], CTA shows a promising future for ultra high-energy gamma rays.

5. Gamma-ray emission from cascade processes

As discussed in section 4.2, gamma-ray spectral features enjoy the perks of being clearly distinguishable from the otherwise featureless astrophysical background. Throughout this work we will engage in the discussion of a variety of features which arise from cascade processes. The study of their phenomenology will prove to be far richer than that of the other more simplistic features. The origins of these features are twofold: kinematics and particle physics. We distinguish two main sets of signals which differ depending on the Lorentz representation of the particles involved in the cascade steps: *gamma-ray boxes* if the intermediate states are scalars or Majorana fermions and *gamma-ray triangles* if these states are Dirac fermions. In this chapter, we discuss the main artefacts that give rise to these features and their phenomenology.

5.1. Kinematical considerations

We study the gamma-ray output of dark matter annihilations and decays as a result of a stepped process. For the sake of simplicity, we discuss in detail the case of annihilating dark matter as the conclusions vary only slightly for dark matter decays and are attainable via a simple replacement. We consider the case where dark matter (self-)annihilates into a pair of intermediate states η which decay in turn into at least one photon $\eta \to \gamma X$. These states are supposed to be sufficiently short-lived such that their decays occur effectively in situ—in practice, since we are interested in Galactic scales spanning hundreds of kiloparsec, decay times smaller than $10^2 - 10^3$ yr fulfil the conditions. In the rest frame of the decaying particle η, the spectrum of the radiated photons is monochromatic, with an energy given by

$$E_\gamma^{\mathrm{RF}} = \frac{1}{2}\,\delta_{X\eta}\,m_\eta \qquad \text{with} \qquad \delta_{ij} = 1 - \frac{m_i^2}{m_j^2}\,. \tag{5.1}$$

We introduce the mass-splitting parameter δ_{ij} which shall be used largely for the remainder of this discussion. If we boost equation (5.1) to a frame with relative velocity $\beta = v$, the photon energy reads

$$E_\gamma = \frac{1}{2}\,\delta_{X\eta}\,E_\eta\left(1 + \beta\,\cos\theta^{\mathrm{RF}}\right)\,, \tag{5.2}$$

where θ^{RF} is the angle between the photon momentum in the rest frame of η and the momentum of η in the laboratory frame. An illustration of the emission of photons is depicted in figure 5.1. In the left part of the figure we show the decay of the intermediate particle η in the rest frame; and in the right part, the same process in the boosted frame.

If we consider the case $\chi\chi \to \eta\eta$ followed by $\eta \to \gamma X$, the energy of the intermediate states is half of the total centre-of-mass energy $E_\eta = \sqrt{s}/2$. Then in the laboratory frame—where dark matter is essentially at rest—the total energy budget is twice the dark matter mass, hence

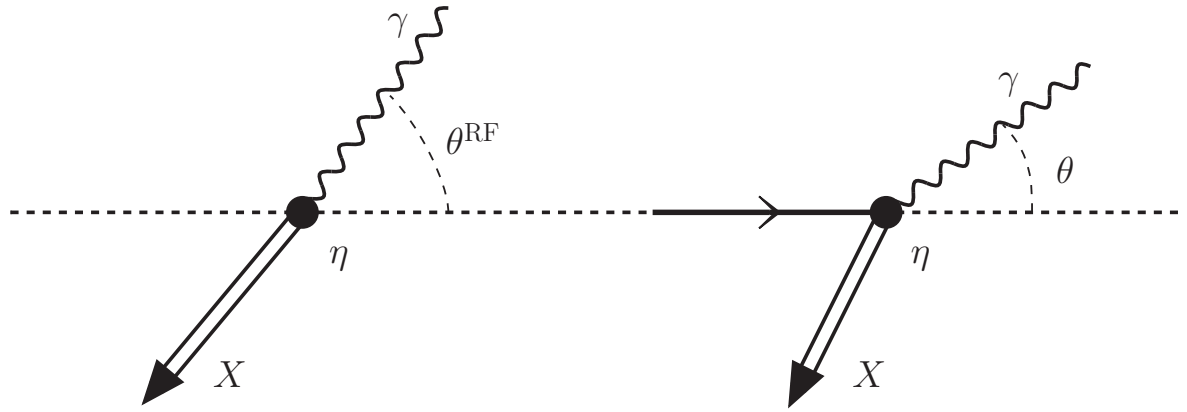

Figure 5.1.: Illustration of the decay of the intermediate particle η. Left: Monochromatic emission in the rest frame with an energy given by equation (5.1). Right: Emission in the laboratory (boosted) frame with an energy dependent on the emission angle as described by equation (5.2).

$\beta = \sqrt{\delta_{\eta\chi}}$[1] and $E_\eta = m_\chi$. At this point and for the remaining of this chapter we introduce the unitless quantity $x = E_\gamma / m_\chi \in [0, 1]$ as a relative energy unit. From the Lorentz transformation in equation (5.2) we read that the photon energy x is restricted to an energy range bounded by the kinematic limits

$$x_\pm = \left(1 \pm \sqrt{\delta_{\eta\chi}}\right) \frac{\delta_{X\eta}}{2} \,, \tag{5.3}$$

related to a forward ($\theta^{\mathrm{RF}} = 0$) and backward ($\theta^{\mathrm{RF}} = \pi$) emission, respectively. We define two new parameters, which will prove to be helpful when addressing the phenomenology, namely the *pivot* $x_\mathrm{c} = (x_+ + x_-)/2$ and the *width* $\Delta x = x_+ - x_-$ of the spectrum. These quantities can be expressed in terms of each of the mass-splitting parameters as

$$x_\mathrm{c} = \frac{1}{2}\delta_{X\eta} \qquad \text{and} \qquad \frac{\Delta x}{x_\mathrm{c}} = 2\sqrt{\delta_{\eta\chi}} \,. \tag{5.4}$$

We want to restate the fact that these considerations were solely kinematical and no assumptions or examination were done at the level of particle physics models. These results can be applied to all cascade processes with the aforementioned characteristics, as are the scenarios within the scope of this work.

5.2. Energy spectrum

In the laboratory frame, the energy of an emitted photon depends on the angle of emission with respect to the momentum of the decaying particle η. Therefore, the shape of the signal within the kinematical bounds is defined by the angular distribution of the emitted photons that can be parametrised as [212]

$$\frac{\mathrm{d}f}{\mathrm{d}\cos\theta^{\mathrm{RF}}} = \frac{1}{2}\left(1 + \alpha\,\cos\theta^{\mathrm{RF}}\right) \,, \tag{5.5}$$

[1] Dark matter could annihilate in two different states $\eta_{1,2}$ with non-equal masses. In this case the velocity is given by $\beta = \sqrt{1 - m_{\eta_1}^2/m_\chi^2 \,\left(1 + (m_{\eta_1} - m_{\eta_2})/4\,m_\chi^2\right)^{-2}}$ where the decay of η_1 into photons is the one being described. With this substitution the rest of the discussion follows analogously.

where $\alpha \in [-1, 1]$ measures the spin polarisation of the decaying particle η, and regulates the *steepness* of the spectrum. Here, the properties of the decaying particle come into play, namely its particular type.

Scalar

In the case of the intermediate state being a scalar the photon emission in the rest frame is isotropic, since there is no preferential emission direction, therefore $\alpha = 0$. Every energy value within the kinematical bounds is equally populated, which produces a flat spectrum between the kinematical bounds.

Majorana fermion

If the intermediate state is Majorana, a preferred direction of emission can be determined, however both chiralities are simultaneously present. This means that although a preferred direction is present, the apparent anisotropic photon emission is effectively cancelled out, therefore $\alpha = 0$.

Dirac fermion

In contrast to the previous cases, if the intermediate state is a Dirac fermion, the spin defines a preferential direction and the chirality is uniquely defined, hence $\alpha \in [-1, 1]$.

For the rest of this work, if the intermediate state is a scalar or a Majorana fermion we denote it with the Greek letter ϕ and refer to the signals as *gamma-ray boxes*, due to their characteristic rectangular shape. If it is a Dirac fermion, then we use the Greek letter ψ and assign the name *gamma-ray triangles* to the spectral feature. To be precise, the shape is trapezoidal, but we classify it as triangular for simplicity of language. Finally, convolving the energy and angular emission spectrum of the photons and boosting to the laboratory frame, we get the normalised photon spectrum

$$\frac{\mathrm{d}N}{\mathrm{d}x} = \frac{N_\gamma}{\delta_{\eta\chi}\,\delta_{X\eta}} \left(\sqrt{\delta_{\eta\chi}} - \alpha + \frac{2\alpha\, x}{\delta_{X\eta}} \right) \Theta\left(x - x_-\right)\, \Theta\left(x_+ - x\right) \,, \tag{5.6}$$

with N_γ the number of photons emitted per annihilation and Θ the Heaviside function. This equation describes the photon emission by a specific gamma-ray production channel. However, physical realisations may posses different cascade processes for the final-state gamma-ray emission, depending on the annihilation and decay channels of each state and the masses of the involved particles. Therefore, the full expression for the gamma-ray emission of cascade processes is given by the sum

$$\frac{\mathrm{d}N_{\mathrm{tot}}}{\mathrm{d}x} = \sum_i \frac{\mathrm{d}N_i}{\mathrm{d}x} \tag{5.7}$$

We would like to comment briefly on cascade scenarios with *decaying* dark matter. As long as a physical realisation is provided, the previous discussion on the phenomenology of cascade processes from dark matter annihilations holds, considering that the centre-of-mass energy is $\sqrt{s} = m_\chi$. Consequently the formalism above holds for the decaying dark matter scenario $\chi \to \eta X_1$ followed by $\eta \to \gamma X_2$ with the pertinent adjustment to N_γ, the replacement $m_\chi \mapsto m_\chi/2$, and the corresponding redefinition of x and $\delta_{\eta\chi}$.

Intermediate states with higher spins

Intermediate states with a spin $S \geq 1$ require a generalisation of equation (5.6). This can be achieved using the Wigner d-functions [213], which describe rotations in the spin space with total angular momentum S as

$$d^S_{m',m}(\theta) = \langle m', S| \, R(\theta) \, |m, S\rangle \tag{5.8}$$

where m is the angular momentum in the rest frame of the intermediate particle η along the boost direction, that is $m = S$; m' is the total angular momentum of the decay products along the angle of emission θ. The angular distribution for any given polarisation m of the decaying particle is then obtained by the addition of the contributions of each mode m' weighted by a model-dependent factor $C_{m'}$

$$\frac{\mathrm{d}f_m}{\mathrm{d}\cos\theta^{\mathrm{RF}}} = n\left(\frac{2S+1}{2}\right)\sum_{m'} C_{m'} \, |d^S_{m',m}\big(\theta^{\mathrm{RF}}\big)\,|^2\,, \tag{5.9}$$

normalised to n photons per annihilation. We note that due to the Landau-Yang theorem [214, 215] a diphoton final state of a decaying vector does not exist. A thorough study on the spectra emitted by particles with spin $S \geq 1$ can be found in [216].

5.3. Phenomenology

In this section we turn to the study of the phenomenology of the signals produced by the formerly explained cascade processes. The three parameters in equation (5.6), (α, $\delta_{\eta\chi}$, $\delta_{X\eta}$) affect the gamma-ray specrum differently. As discussed in equation (5.4), the mass-splitting parameters $\delta_{\eta\chi}$ and $\delta_{X\eta}$ regulate the width and pivot of the signal, whereas the parameter α determines the steepness of the signal, as can be directly read from equation (5.6). We now turn to a thorough examination of these effects.

Steepness

From equation (5.6), we read that the slope of the spectrum depends on the three phenomenological parameters. However, the mass-splitting parameters have further effects on the signal, hence their influence on the steepness ensures a constant spectrum normalisation equal to N_γ. The only parameter which exclusively regulates the slope of the signal is the spin polarisation α, which we will also refer as the steepness parameter. Here we recall that for gamma-ray boxes—where the intermediate state is either scalar or Majorona fermion— we have $\alpha = 0$, therefore the slope remains flat for all scenarios. On the other hand, if we consider the case of gamma-ray triangles—the intermediate state is a Dirac particle—then $\alpha \in [-1, 1]$. We illustrate the effect of altering the value of α on a baseline scenario with the parameters $\delta_{\eta\chi} = 0.25$ and $\delta_{X\eta} = 1$ in the left panel of figure 5.2. It is worth noticing that α can take negative values where the peak of the signal switches from the right x_+ to the left end of the triangle x_-. We name these subcategories up-triangle and down-triangle for $\alpha > 0$ and $\alpha < 0$, respectively.

Width

We now turn to the discussion on the effect of the mass splittings. As outlined in equations (5.2) and (5.4), the relative width of the signal is regulated by the velocity at which η is produced,

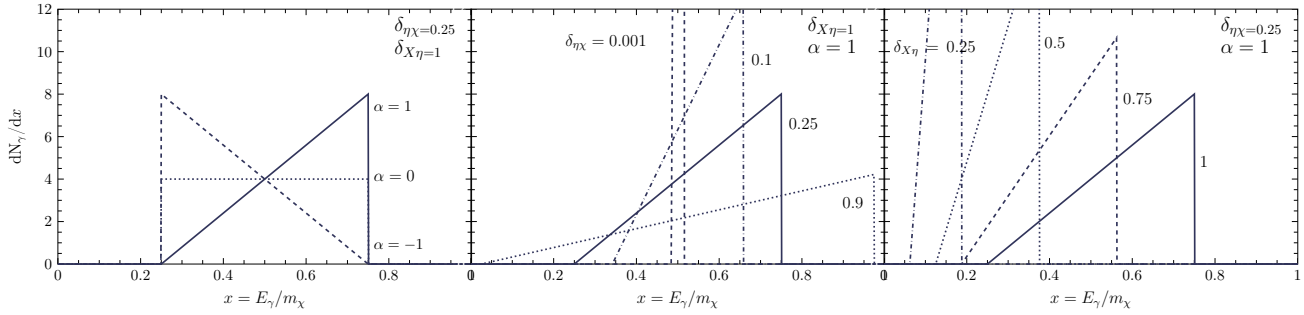

Figure 5.2.: Photon spectra as emitted by a cascade process described by equation (5.6) while varying the three phenomenological parameters. Left: Variation of the steepness parameter α. Centre: Variation of the width parameter $\delta_{\eta\chi}$. Right: Variation of the pivot parameter $\delta_{X\eta}$.

$\Delta x/x_c = 2\sqrt{\delta_{\eta\chi}}$. On the one hand, if this particle is produced essentially at rest ($\delta_{\eta\chi} \to 0$), then the signal becomes sharp and the flux grows in proportion, such that the normalisation is conserved. On the other hand, the larger the velocity of η ($\delta_{\eta\chi} \to 1$), the larger the gap between the kinematical ends is and the spectrum becomes wider and fainter, conserving the spectrum normalisation N_γ, as well. This effect is illustrated in the centre panel of figure 5.2 for baseline parameters $\alpha = 1$ and $\delta_{X\eta} = 1$.

Pivot

Lastly, we address the effect of the mass splitting $\delta_{X\eta}$. This parameter relates the masses of the intermediate state and the final non-photonic state, which dictates the monochromatic energy of the photon in the rest frame of η. It is worth noticing that, in the case of a diphoton emission, this parameter is set by $\delta_{X\eta} = \delta_{\gamma\eta} \equiv 1$. However, due to Lorentz symmetry, this is only possible if the intermediate state is a scalar $\phi \to \gamma\gamma$. Furthermore, if this channel is viable, the decay mode $\phi \to \gamma Z$ is also open if kinematically allowed and in this case $\delta_{X\eta} = \delta_{Z\eta} < 1$. We recall from equation (5.4) that the positioning of the signal is centred at the pivot $x_c = \delta_{X\eta}/2$. This interesting feature enables for scenarios to emit photons with an energy much lower than the mass scale of dark matter, provided that $\delta_{X\eta} \ll 1$ and therefore $x_c \ll 1$. We illustrate the effect of varying the mass splitting $\delta_{X\eta}$ in the right panel of figure 5.2.

There is no *a priori* relation between these parameters and their possible configurations are only constrained by the details of the particular particle physics model under consideration. However, if η is produced at low velocities with a specific chirality, a mass insertion can flip the chiralities cancelling effectively any anisotropic decay and so setting $\alpha \to 0$. On the other hand, if these velocities are relativistic, then such a mass insertion is less likely and the spin polarisation is almost maximal, $\alpha \to 1$. For more details on models see chapter 6.

We showed that cascade annihilations and decays give rise to a rich and interesting phenomenology, regulated by three phenomenological parameters at a scale of the dark matter mass. In the next chapters we address several physical realisations of scenarios that feature this kind of cascade processes and the viability of detecting such signals with state-of-the-art telescopes.

6. Dark matter models

In this chapter, we introduce two different particle physics realisations based on the Peccei-Quinn (PQ) mechanism [217], that produce gamma-ray boxes—labelled A and B— as well as an asymmetric dark matter (ADM) model capable of generating gamma-ray triangles—labelled C. In order to produce these signatures, these models need to fulfil three conditions: provide a stable (or long lived) particle χ as a dark matter candidate, which is supposed to account for (almost) all of the observed relic abundance; include an intermediate state η that couples to χ; and allow η to decay into at least one photon with a sizeable branching ratio. Other models that produce this kind of gamma-ray signatures have been discussed in [216, 218–220].

6.1. Model A: Dark matter with generic Peccei-Quinn mechanism

We discuss the model first introduced in [221–223] and discussed in the context of gamma-ray boxes in [7]. In this model the SSB of an explicitly broken $\mathrm{U}(1)_{\mathrm{PQ}}$ symmetry generates a massive pseudo-Goldstone boson which serves as intermediate state.

The Lagrangian

This model is characterised by the addition of a Dirac dark matter particle χ and a complex scalar S to the SM particle content, and the extension of $\mathrm{G_{SM}}$ by a global $\mathrm{U}(1)_{\mathrm{PQ}}$ symmetry[1]. On the one hand, the added fields are singlets under $\mathrm{G_{SM}}$ and transform under the new symmetry as $\chi \mapsto e^{i\gamma_5\alpha}\chi$ and $S \mapsto e^{-2i\alpha}S$. On the other hand, all SM fields transform trivially under $\mathrm{U}(1)_{\mathrm{PQ}}$ and as usual under $\mathrm{G_{SM}}$. The Lagrangian of model A reads

$$\begin{aligned}
\mathcal{L}_{\mathrm{A}} &= \mathcal{L}_{\mathrm{SM}} + \mathcal{L}_{\chi} + \mathcal{L}_{S} + \mathcal{L}_{\mathrm{int}} \quad \text{with} && (6.1)\\
\mathcal{L}_{\chi} &= i\bar{\chi}\gamma^{\mu}\partial_{\mu}\chi\,, && (6.2)\\
\mathcal{L}_{S} &= \partial_{\mu}S\partial^{\mu}S^{*} - m_{S}^{2}|S|^{2} - \lambda_{S}|S|^{4} + \left(\frac{1}{2}m_{S}'^{2}S^{2} + \mathrm{h.c.}\right)\,, && (6.3)\\
\mathcal{L}_{\mathrm{int}} &= -\lambda_{\chi}\left(S\bar{\chi}P_{L}\chi + S^{*}\bar{\chi}P_{R}\chi\right) - 2\lambda_{H\,S}|H|^{2}|S|^{2}\,. && (6.4)
\end{aligned}$$

Notice that the global $\mathrm{U}(1)_{\mathrm{PQ}}$ symmetry is explicitly broken at a quantum level, and at tree level, if the last mass term $m_S'^2$ in equation (6.3) is non-vanishing[2]. Lastly, we assume that the field S acquires a non-vanishing vev $\langle S\rangle \equiv v_S/\sqrt{2}$, such that this symmetry is also spontaneously broken. This vev allows us to expand the complex scalar field as $S = (v_S + s + i\,a)/\sqrt{2}$. We remark that s is a scalar (CP even) and a is pseudo-scalar (CP odd).

[1] This symmetry resembles the U(1) symmetry from the PQ mechanism, which was introduced in as a possible resolution of the strong CP problem [217]. In this model we invoke this mechanism modifying it to our purposes. The resulting particles are not related with the axion in any fashion.

[2] Such a mass term can originate from a six dimensional operator $\frac{g}{M^2}\Phi^4 S^2 + \mathrm{h.c.}$, where Φ is the Peccei-Quinn breaking field, with $\langle\Phi\rangle = f_a \gg v_S$. In this case, experimental evidence could constrain the parameter space of m_a.

The Lagrangian $\mathcal{L}_{\rm int}$ gives rise to the mass and interaction terms of dark matter, as well as to a mixing term between the scalar s and the Higgs boson h. Assuming, for simplicity, that λ_χ is real, the first term leads to

$$\mathcal{L}_{\rm DM} = -m_\chi\,\overline{\chi}\chi - \frac{1}{\sqrt{2}}\lambda_\chi\, s\,\overline{\chi}\chi + \frac{i}{\sqrt{2}}\lambda_\chi\, a\,\overline{\chi}\gamma^5\chi\,, \tag{6.5}$$

where $m_\chi \equiv \lambda_\chi\, v_S/\sqrt{2}$ is the dark matter mass acquired via the Higgs mechanism using the complex scalar field S as Higgs field instead of the usual SM scalar doublet. From the spontaneous breaking of the PQ symmetry a residual Z_2 symmetry remains—under which only χ is odd—guaranteeing the stability of dark matter. Furthermore, the field a can be identified with the pseudo-Goldstone boson expected from the SSB. The mass of the pseudo-scalar is given by $m_a \simeq m'_S$ plus additional anomaly corrections. These anomalies allow for the particle a to decay into lighter SM particles without affecting the other terms in $\mathcal{L}_{\rm A}$, in particular the stability of dark matter. From here on, we will consider the case where $m'_S \neq 0$.

Simultaneously, the mass operators from the scalar potential generates a mass matrix for the CP-even scalar s and the SM Higgs boson h, which can be diagonalised by the field rotation

$$\begin{aligned} s &= \cos\tilde{\theta}\,\tilde{s} + \sin\tilde{\theta}\,\tilde{h} \\ h &= -\sin\tilde{\theta}\,\tilde{s} + \cos\tilde{\theta}\,\tilde{h} \end{aligned}\,, \quad \text{with} \quad \tan 2\tilde{\theta} = \frac{2\lambda_{H\,S}\, v_S\, v_H}{\lambda_H\, v_H^2 - \lambda_S\, v_S^2}\,, \tag{6.6}$$

where $v_H \simeq 246\,\text{GeV}$ is the Higgs vev and λ_H is the coupling of the quartic Higgs field interaction. This diagonalisation translates into a mixing between these two scalar fields which is particularly important at early stages of the universe for the thermalisation of dark matter with the SM plasma, from which it freezes-out later on, as discussed below.

In this scenario, both states s and a are unstable. For our purposes, the decay of the CP-even scalar s is not of special interest. It suffices to say that s decays into SM particles mainly due to the mixing with the Higgs boson, and, if kinematically allowed, into a pair of dark matter particles or CP-odd scalars a. For a full expression of these decay widths we refer to [221]. On the contrary, we study the decay channels of a in more detail, for it decays into a pair of electroweak gauge bosons via the anomaly loop

$$\mathcal{L}_{\rm int} \supset \sum_{i=1,2} \frac{c_i \alpha_i}{8\pi v_s} a\, F^i_{\mu\nu}\tilde{F}^{i\,\mu\nu} = \sum_{i\leq j} 2\, c_{V_iV_j} a\; F^{\mu\nu}_{V_i}\tilde{F}_{V_j\,\mu\nu}\,, \tag{6.7}$$

where $\alpha_i \equiv g_i^2/4\,\pi$ and $g_{1,2}$ are the coupling constants of $\mathrm{U(1)_Y}$ and $\mathrm{SU(2)_L}$, respectively, c_i are constant parameters that depend on the nature of the anomaly, and $c_{V_iV_j}$ are simply a redefinition of the latter, see equations (6.8). Lastly, $\tilde{F}^X_{\mu\nu} \equiv \frac{1}{2}\epsilon_{\mu\nu\rho\sigma}F^{X\,\rho\sigma}$ and $F^X_{\mu\nu}$ are the dual and standard field strength tensor for the group $X = 1, 2$ or the gauge boson $X = V_i$. The interaction Lagrangian in equation (6.7) can be generated e.g., by extending the model with new heavy fermions, charged under the electroweak groups, that couple to the complex scalar S. In this case the charge assignment would dictate the value of the parameters c_i. We write the non-zero effective couplings $c_{V_iV_j}$ as

$$\begin{aligned} c_{\gamma\gamma} &= \frac{1}{16\pi\, v_S}(c_1\,\alpha_1\,\cos^2\theta_W + c_2\,\alpha_2\,\sin^2\theta_W)\,, \\ c_{Z\gamma} &= \frac{1}{16\pi\, v_S}(c_2\,\alpha_2 - c_1\,\alpha_1)\sin(2\theta_W)\,, \\ c_{ZZ} &= \frac{1}{16\pi\, v_S}(c_2\,\alpha_2\,\cos^2\theta_W + c_1\,\alpha_1\,\sin^2\theta_W)\,, \\ c_{WW} &= \frac{c_2\,\alpha_2}{8\pi\, v_S}\,. \end{aligned} \tag{6.8}$$

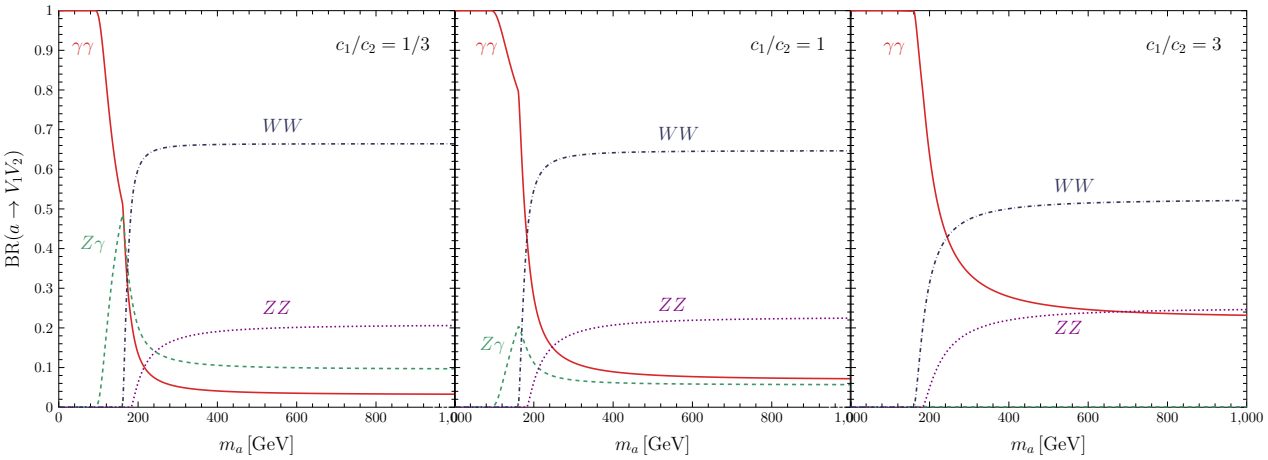

Figure 6.1.: Branching fraction of the pseudo-scalar a of model A as a function of the into a pair of electroweak gauge bosons for a several choices of the ratio c_1/c_2.

Consequently, the decay modes induced by these anomalies are $a \to \gamma\gamma\,, \gamma Z\,, ZZ\,, W^+W^-$, with the corresponding decay rates

$$\begin{aligned}
\Gamma_a(\gamma\gamma) &= \frac{m_a^3}{\pi}|c_{\gamma\gamma}|^2\,, \\
\Gamma_a(Z\gamma) &= \frac{m_a^3}{2\pi}|c_{Z\gamma}|^2\left(1-\frac{m_Z^2}{m_a^2}\right)^3\,, \\
\Gamma_a(ZZ) &= \frac{m_a^3}{\pi}|c_{ZZ}|^2\left(1-\frac{4m_Z^2}{m_a^2}\right)^{3/2}\,, \\
\Gamma_a(W^+W^-) &= \frac{m_a^3}{2\pi}|c_{WW}|^2\left(1-\frac{4m_W^2}{m_a^2}\right)^{3/2}\,.
\end{aligned} \tag{6.9}$$

Other decay modes into other SM fermions are not allowed at tree level.

We report the branching fractions of the pseudo-scalar decay as a function of m_a in figure 6.1 for various choices of the ratio c_1/c_2. At low energies, only the decay into photons $a \to \gamma\gamma$ is allowed leading to a 100% branching ratio. However, at larger masses the decay into a $W^\pm$ pair becomes dominant suppressing the decay channels containing photons down to $\simeq 5\%$. Nevertheless, the other channels remain relevant provided they are kinematically open.

Annihilation cross sections

At tree level, dark matter can annihilate via t-channel diagrams into $\chi\overline{\chi} \to aa, ss, sa$, or via s-channel diagrams into a pair of gauge bosons $\chi\overline{\chi} \to V_iV_j$ if the mediator is the CP-odd scalar a, and into different SM fermions $\chi\overline{\chi} \to f\overline{f}$ if the mediator is the CP-even s. The s-channel modes are loop or mixing suppressed and therefore the annihilation is dominated by the t-channel modes, unless the former are resonantly enhanced, i.e. $m_a, m_s \simeq 2m_\chi$.

We derive the annihilation cross sections times velocity for the t-channel processes under the assumption that the mixing between the Higgs and the s bosons is zero, $\tilde{\theta} \to 0$. A generalisation to a case with non-vanishing mixing angle is then easily obtained using the mass eigenvalues corresponding to $\tilde{s}$ and $\tilde{h}$ from equation (6.6). The generic dark matter annihilation cross

sections times relative velocity for all t-channel modes reads

$$(\sigma v_{\rm rel})_{ij} = \frac{1}{32\pi^2\,\kappa\,s}\left(1-\frac{(m_i-m_j)^2}{s}\right)^{1/2}\left(1-\frac{(m_i+m_j)^2}{s}\right)^{1/2}\int {\rm d}\Omega\overline{|\mathcal{M}|^2_{ij}} \tag{6.10}$$

where $\kappa = 1(2)$ if $ij = as(aa, ss)$. We note that this is not a velocity averaged quantity. Furthermore, we will use for simplicity the Mandelstam variables

$$\begin{aligned}
s &= 4m_\chi^2\left(1-\frac{v_{\rm rel}^2}{4}\right)^{-1} \simeq 4m_\chi^2\left(1+\frac{v_{\rm rel}^2}{4}\right), && (6.11)\\
t &= \frac{1}{2}\left(m_i^2+m_j^2+2m_\chi^2-s\right)+\frac{v_{\rm rel}}{4}\cos\theta\left[\left(m_i^2-m_j^2+s\right)^2-4s\,m_i^2\right]^{1/2}\\
&\simeq \frac{1}{2}\left(m_i^2+m_j^2-2m_\chi^2-m_\chi^2\,v_{\rm rel}^2\right) && (6.12)\\
&\quad +\frac{v_{\rm rel}}{4}\cos\theta\left[\left(m_i^2-m_j^2+4m_\chi^2\right)^2-16m_\chi^2\,m_i^2\right]^{1/2},\\
u &= \frac{1}{2}\left(m_i^2+m_j^2+2m_\chi^2-s\right)-\frac{v_{\rm rel}}{4}\cos\theta\left[\left(m_i^2-m_j^2+s\right)^2-4s\,m_i^2\right]^{1/2}\\
&\simeq \frac{1}{2}\left(m_i^2+m_j^2-2m_\chi^2-m_\chi^2\,v_{\rm rel}^2\right) && (6.13)\\
&\quad -\frac{v_{\rm rel}}{4}\cos\theta\left[\left(m_i^2-m_j^2+4m_\chi^2\right)^2-16m_\chi^2\,m_i^2\right]^{1/2},
\end{aligned}$$

where $v_{\rm rel}$ is the Möller velocity as defined in [224], θ is the angle between the momenta of the incoming dark matter particle and the outgoing (pseudo-)scalar in the centre-of-mass frame. The approximations are valid in a non-relativistic regime up to the order $\mathcal{O}(v_{\rm rel}^2)$ and are useful for the partial wave expansion of (σv). The full squared amplitudes for these three channels are

$$\begin{aligned}
\overline{|\mathcal{M}|^2_{sa}} &= \frac{|\lambda_\chi|^4}{8}\frac{(t+u-2m_\chi^2)^2}{(t-m_\chi^2)^2(u-m_\chi^2)^2}\times\\
&\quad \left[\left(m_s^2+m_\chi^2-t\right)\left(m_s^2+m_\chi^2-u\right)-m_s^2\,s+4m_a^2m_\chi^2\right], && (6.14)\\
\overline{|\mathcal{M}|^2_{aa}} &= \frac{|\lambda_\chi|^4}{8}\left(\frac{1}{t-m_\chi^2}-\frac{1}{u-m_\chi^2}\right)^2\times\\
&\quad \left[\left(m_a^2+m_\chi^2-t\right)\left(m_a^2+m_\chi^2-u\right)-m_a^2\,s\right], && (6.15)\\
\overline{|\mathcal{M}|^2_{ss}} &= \frac{|\lambda_\chi|^4}{8}\frac{1}{(t-m_\chi^2)^2(u-m_\chi^2)^2}\Big[(u-t)^2\Big(\left(m_s^2+m_\chi^2-t\right)\left(m_s^2+m_\chi^2-u\right)-m_s^2\,s\\
&\quad +4m_\chi^2\left(t+u-2m_\chi^2\right)\Big)+4m_\chi^2\left(s-4m_\chi^2\right)(t+u-2m_\chi^2)^2\Big]. && (6.16)
\end{aligned}$$

Finally, by using equation (6.10) we are able to compute the analytic expressions of the anni-

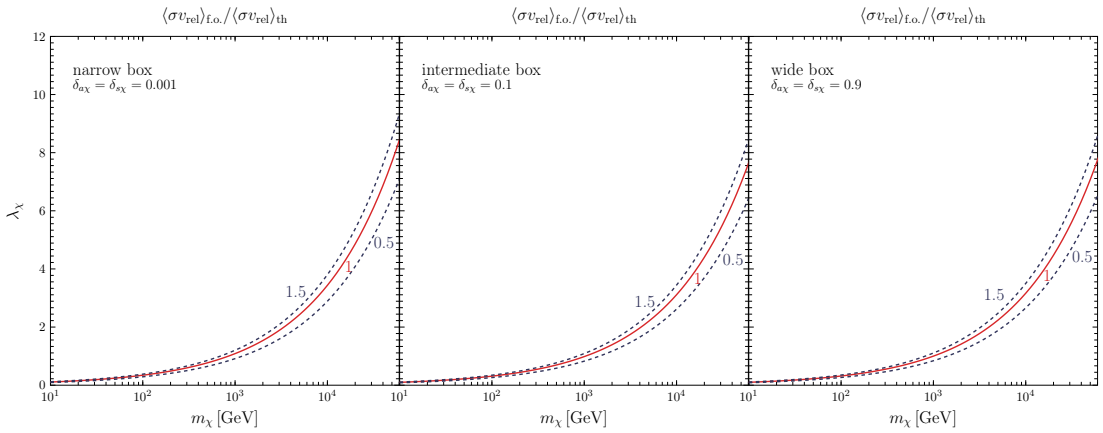

Figure 6.2.: Ratio between the velocity averaged cross section of model A and that for the thermal cross section $\langle\sigma v\rangle_{\rm th}$ for the mass splittings $\delta_{a\chi} = \delta_{s\chi} = 0.001, 0.1, 0.9$ in the $\lambda_\chi - m_\chi$ plane.

hilation cross sections in the non-relativistic limit:

$$(\sigma v_{\rm rel})_{sa} \simeq \frac{|\lambda_\chi|^4}{64\pi m_\chi^2} \frac{\left(m_a^2 - m_s^2 + 4m_\chi^2\right)^2}{\left(m_a^2 + m_s^2 - 4m_\chi^2\right)^2} \left(1 - \frac{(m_a - m_s)^2}{4m_\chi^2}\right)^{1/2} \times \left(1 - \frac{(m_a + m_s)^2}{4m_\chi^2}\right)^{1/2}, \tag{6.17}$$

$$(\sigma v_{\rm rel})_{aa} \simeq \frac{|\lambda_\chi|^4}{96\pi} \frac{m_\chi^6}{\left(m_a^2 - 2m_\chi^2\right)^4} \left(1 - \frac{m_a^2}{m_\chi^2}\right)^{5/2} v_{\rm rel}^2\,, \tag{6.18}$$

$$(\sigma v_{\rm rel})_{ss} \simeq \frac{|\lambda_\chi|^4}{96\pi} \frac{m_\chi^2}{\left(m_s^2 - 2m_\chi^2\right)^4} \left(2\left(m_s^2 - 2m_\chi^2\right)^2 + m_\chi^4\right) \left(1 - \frac{m_s^2}{m_\chi^2}\right)^{1/2} v_{\rm rel}^2\,. \tag{6.19}$$

We can see that the annihilation modes $\chi\overline{\chi} \to aa, ss$ are both p-wave and are therefore suppressed, since $v_{\rm rel} \simeq 10^{-3}$. On the contrary, the process $\chi\overline{\chi} \to as$ does not suffer from this suppression and, if allowed by kinematics, dominates over the other two channels. We can distinguish three cases depending on the mass splitting of m_χ, m_a and m_s

$$\mathrm{BR}(sa, aa, ss) \simeq \begin{cases} (1,0,0) & \text{if} \quad m_a + m_s < 2m_\chi \\ (0,1,0) & \text{if} \quad m_a + m_s > 2m_\chi \text{ and } m_a < m_\chi \\ (0,0,1) & \text{if} \quad m_a + m_s > 2m_\chi \text{ and } m_s < m_\chi\,. \end{cases} \tag{6.20}$$

For the scope of this work, we focus on the case where $m_a < m_\chi$, $m_a = m_s$, and the mixing between the CP-even scalars s and h is small. In this scenario, a discussion of the s-channel annihilations is not of particular interest as they are generically suppressed and do not produce sizeable gamma-ray fluxes[3].

[3]The s-channel annihilation into two Higgs bosons has the correct properties to produce gamma-ray boxes as $\chi\overline{\chi} \to hh$ followed by $h \to \gamma\gamma$. However, this process is heavily suppressed by the branching ratios of dark matter annihilations into h, and of the decay of h into photons.

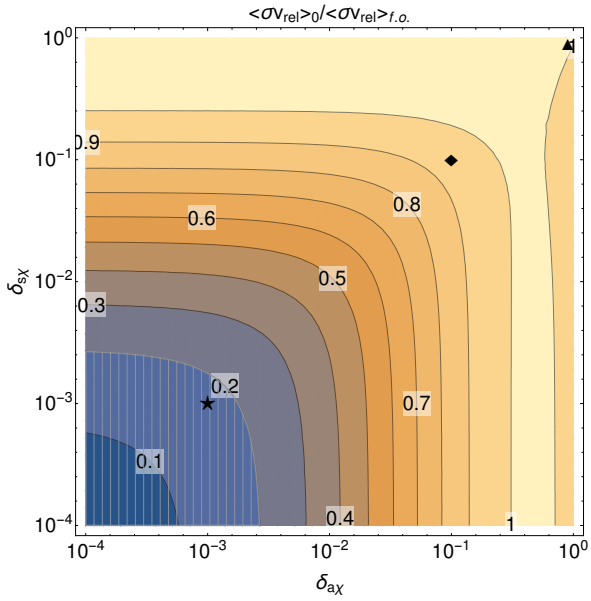

Figure 6.3.: Contour plot of the present-to-thermal annihilation cross section ratio $\langle\sigma v_{\rm rel}\rangle_0/\langle\sigma v_{\rm rel}\rangle_{\rm f.o.}$ in the $\delta_{a\chi}$–$\delta_{s\chi}$ plane. The hatched region delimits the parameter space where the width Δx of the signal is less than 10% or less than the maximum energy of the photons x_+. We show the three benchmark points with $\delta_{a\chi} = \delta_{s\chi} = 0.001$ for the narrow (★), 0.1 for the intermediate (♦), and 0.9 for the wide (▲) box scenarios.

This model introduces dark matter as a thermal relic within the WIMP paradigm and accounts for the dark matter abundance through freeze-out from the thermal bath as discussed in section 3.2.1. The relic density is essentially determined by the velocity-averaged t-channel annihilation processes from equations (6.17), (6.18), and (6.19). The thermal averaging is obtained by applying a full averaging procedure e.g., equation (3.8) from [224]. We show in figure 6.2, that for different mass splittings $\delta_{a\chi}$ the relic density at freeze-out temperatures $T_{\rm f.o.} \simeq m_\chi/25$ can be reproduced for a wide range in dark matter masses with $\lambda_\chi \simeq \mathcal{O}(1)$. Three benchmark points were chosen differing in the width of the signal: narrow ($\delta_{a\chi} = 0.001$), intermediate ($\delta_{a\chi} = 0.1$), and wide box scenarios ($\delta_{a\chi} = 0.9$). These cases will be also a reference point for later chapters. Finally, we report in figure 6.3 the ratio of the present-to-thermal total annihilation cross sections, $\langle\sigma v_{\rm rel}\rangle_0/\langle\sigma v_{\rm rel}\rangle_{\rm f.o.}$. We find that for finer mass splittings ($\delta_{a\chi} \to 0$) the velocity-dependent contribution has a larger impact and the present-to-thermal cross-section ratio decreases, specifically for the benchmark cases

$$\frac{\langle\sigma v_{\rm rel}\rangle_0}{\langle\sigma v_{\rm rel}\rangle_{\rm f.o.}} \simeq \begin{cases} 0.170 & \text{for} \quad \delta_{a\chi} = 0.001 \quad ★ \\ 0.949 & \text{for} \quad \delta_{a\chi} = 0.1 \quad ♦ \\ 1.019 & \text{for} \quad \delta_{a\chi} = 0.9 \quad ▲ \end{cases} . \tag{6.21}$$

This model clearly produces gamma-ray boxes as we read from a comparison with the kinematics described in chapter 5. We identify the intermediate and final states $\phi = a$ and $X = \gamma$ which implies $\delta_{\gamma a} = 1$. Furthermore, considering the discussion on the annihilation and decay modes, the most relevant cascade annihilation in this model is $\chi\overline{\chi} \to as$ followed by $a \to \gamma\gamma$. Consequently, we have for the width and pivot parameters from equation (5.4): $x_{\rm c} = 1/2$ and $\Delta x/x_{\rm c} = 2\sqrt{\delta_{a\chi}}$, and for the steepness parameter $\alpha = 0$ since a has no spin.

6.2. Model B: Dark matter and the axion portal

We discuss the framework discussed in references [225–227], which was established in order to interpret the positron excesses observed by PAMELA [93, 100–102] and AMS-02 [94, 103–105], and confirmed by Fermi-LAT [106]. This framework invokes the usual PQ mechanism and uses the leptonic decay modes of the resulting axion to account for this excess, hence the label "axion portal". However, this pseudo-scalar produces large antiproton, neutrino, and gamma-ray (via ICS) fluxes, and has to be modified in some manner to agree with the respective observations.

We distinguish two concrete models: a minimal axion portal construction (B1) and a leptonic axion portal construction (B2). In both cases, a new $\mathrm{U}(1)_{\mathrm{PQ}}$ symmetry is introduced as well as a vector-like fermion WIMP dark matter field χ and a complex scalar S which can be expanded as $S = \left(f_a + s/\sqrt{2}\right) e^{i\,a/\sqrt{2}f_a}$, with the vev $\langle S\rangle = f_a$. The mass terms m_χ, m_a, and m_s, as well as the dark matter couplings to s and a stem from the Yukawa interaction

$$\mathcal{L}_{\mathrm{B}} \supset -\xi\, S\, \overline{\chi}\, \chi + \text{ h.c.}\,, \tag{6.22}$$

after the breaking of the $\mathrm{U}(1)_{\mathrm{PQ}}$ symmetry. Furthermore, a remaining Z_2 symmetry ensures the stability of dark matter. This opens the three possible annihilation channels $\chi\overline{\chi} \to aa, ss, sa$ through which thermal freeze-out is achieved. However, only the annihilation into as has an s-wave component making this channel dominant at the present-day annihilation rate. We assume the mass hierarchy $m_a \ll m_s \ll m_\chi$ within both constructions. In order to account for the positron excess, and since the scalar s dominantly decays as $s \to aa$, the axion must decay dominantly into a lepton pair, i.e. leptons must carry non-trivial charges under $\mathrm{U}(1)_{\mathrm{PQ}}$. Here, the difference between the models becomes apparent as we now explain.

In the model with minimal axion portal we have

$$\mathcal{L}_{\mathrm{B1}} \supset -\lambda_u^\alpha\, \overline{Q^\alpha}\, h_u\, u_{\mathrm{R}}^\alpha - \lambda_d^\alpha\, \overline{Q^\alpha}\, h_d\, d_{\mathrm{R}}^\alpha - \lambda_\nu^\alpha\, \overline{L^\alpha}\, h_u\, \nu_{\mathrm{R}}^\alpha - \lambda_e^\alpha\, \overline{L^\alpha}\, h_d\, e_{\mathrm{R}}^\alpha + f_q\, S\, h_u\, h_d + \text{ h.c.}\,, \tag{6.23}$$

where h_u and h_d are the Higgs doublets, $\alpha = 1, 2, 3$ label the fermion generation, $Q^\alpha \equiv (u^\alpha, d^\alpha)_{\mathrm{L}}$ and $L^\alpha \equiv (\nu^\alpha, e^\alpha)_{\mathrm{L}}$ are the left-handed quark and lepton doublets, and u_{R}^α, d_{R}^α, ν_{R}^α, and e_{R}^α are the right-handed quark and lepton singlets. From this term it is clear that both Higgs doublets and therefore the leptons and quarks transform non-trivially under the PQ symmetry. This yields to large hadronic couplings of a and constrains the model accordingly. In this realisation, the decay mode into three pions $a \to \pi^+\pi^-\pi^0$ produces large gamma-ray fluxes from the pion decay $\pi^0 \to \gamma\gamma$, setting an upper bound on the axion mass. Furthermore, collider experiments set a lower bound on m_a. For a complete summary of these constraints we refer to [225]. Within the framework B1, the preferred axion mass range is

$$360\,\mathrm{MeV} \lesssim m_a \lesssim 800\,\mathrm{MeV}\,. \tag{6.24}$$

Due to helicity suppression, the primary decay channel of a is into the heaviest kinematically allowed lepton, in this case into a $\mu^\pm$ pair. This leads to some tension with the absence of galactic neutrinos [226].

In contrast, in the model with leptonic axion portal only leptons are charged under a $\mathrm{U}(1)_{\mathrm{X}}$ symmetry and therefore the "axion" does not couple to hadrons[4]. Analogously to the previous case we introduce separate Higgs doublets

$$\mathcal{L}_{\mathrm{B2}} \supset -\lambda_e^\alpha\, \overline{L^\alpha}\, h_e\, e_{\mathrm{R}}^\alpha - \lambda_d^\alpha\, \overline{L^\alpha}\, h_\nu\, \nu_{\mathrm{R}}^\alpha + f_l\, S\, h_e\, h_\nu + \text{ h.c.} \tag{6.25}$$

[4]This "axion" is not related to the standard QCD axion and does not present a solution to the strong CP problem.

with h_e and h_ν being the Higgs doublets. For the Higgs mechanism in the quark sector, at least one additional Higgs field—singlet under the leptonic $\mathrm{U}(1)_\mathrm{X}$ symmetry—is required. Furthermore, if the PQ mechanism in the QCD sector is still desired a new complex scalar S_q and a new hadronic $\mathrm{U}(1)_\mathrm{PQ}$ symmetry are necessary. In this realisation a decays mostly into the heaviest leptonic channel allowed, which constrains the range for the axion mass to

$$2m_e \lesssim m_a \lesssim 2m_\mu \,, \tag{6.26}$$

in order to avoid an overproduction of neutrinos, leading to tensions with observations. Notice that in both cases $\mathcal{L}_{\mathrm{B1,B2}}$ a right-handed neutrino was also introduced, for small neutrino masses to be obtained. Furthermore, these models can be easily embedded into a supersymmetric framework.

Through these distinct portals the necessary leptonic decay modes are enabled for the account of the positron excess. For the purposes of this work, the decay channel into two photons is of particular interest. Previous works [226] found bounds on this channel at $\mathrm{BR}\,(a \to \gamma\gamma) \simeq 10^{-3}$, which we shall use as benchmark value when comparing to experimental observations. Finally, we note that this model experiences a boost factor due to Sommerfeld enhancement [228–230] and the formation of dark matter bound states [231], which are consequences of non-perturbative effects from interactions with s in the range $m_s \ll m_\chi$. This boost factor is of order $B_S \simeq \mathcal{O}(10^3)$ on the present-day annihilation rate.

Just as model A, both variants of model B produce gamma-ray boxes. The intermediate and final states are identified as $\phi = a$ and $X = \gamma$ and therefore $\delta_{\gamma a} = 1$. For both realisations we have the main cascade process $\chi\overline{\chi} \to as$ followed by $a \to \gamma\gamma$. Due to the mass hierarchies, the other mass-splitting parameter is confined to the limit $\delta_{a\chi} \to 1$ and we have $x_\mathrm{c} = 1/2$ and $\Delta x/x_\mathrm{c} \to 2$, and since a as a pseudo-scalar $\alpha = 0$.

6.3. Model C: Asymmetric Dark Matter and gamma-ray triangles

In order to produce gamma-ray triangles there is still one hindrance that the model has to overcome. As argued in section 5.2 the intermediate state has to be a Dirac fermion to allow α to take non-zero values. However, if we consider the case where the intermediate state is produced as a particle-antiparticle pair, each of these particles has the same and opposite chirality as each other. Therefore, the gamma-ray spectra emitted by each Dirac fermion following equation (5.6) are equal up to a relative sign for α. The resulting spectrum, obtained by the addition of both emissions, is then indistinguishable from a gamma-ray box. Using equation (5.6) we have

$$\left.\frac{\mathrm{d}N}{\mathrm{d}x}\right|_{\alpha\to+\alpha} + \left.\frac{\mathrm{d}N}{\mathrm{d}x}\right|_{\alpha\to-\alpha} = 2\,\frac{N_\gamma}{\sqrt{\delta_{\eta\chi}}\,\delta_{X\eta}}\,\Theta\left(x - x_-\right)\,\Theta\left(x_+ - x\right)\,, \tag{6.27}$$

which has no longer a term linear in x. This argument also holds in the case of decaying dark matter, as the decays from particles and antiparticles produce particles with opposite chiralities. For this reason we introduce a simplified Asymmetric Dark Matter (ADM) framework that realises gamma-ray triangles introduced and discussed in [9]. The origins of the asymmetry are not specified, see section 3.2.2 for details.

The Lagrangian

In this model, we consider three additional fields with respect to the SM, two Dirac spinors χ and N_D, and one real scalar field S, which are singlets under $\mathrm{G_{SM}}$. To ensure the stability of

Field	L^i	e^i_{R}	N_D	χ	S
$\mathrm{U(1)_X}$	1	1	1	1	0
Z_2	1	1	1	-1	-1

Table 6.1.: Particle content and charge assignments of the simplified ADM model C. L^i and e^i_{R} are the SM lepton doublets and singlets of generation $i = 1, 2, 3$, respectively.

dark matter we impose a Z_2 symmetry to the overall Lagrangian under which only χ and S are odd. For reasons that will become apparent shortly, we introduce a global $\mathrm{U(1)_X}$ symmetry under which the SM right-handed (left-handed) leptons, e^i_{R} ($L^i \equiv \left(\nu^i, e^i\right)_{\mathrm{L}}$) for the different fermion families $i = 1, 2, 3$, transform non-trivially. We can identify the conserved quantity from this symmetry with the total lepton number. We summarise the particle content and charge assignments in table 6.1.

The Lagrangian of this model reads:

$$\begin{aligned}\mathcal{L}_{\mathrm{C}} &= \mathcal{L}_{\mathrm{SM}} + \frac{1}{2}\partial_\mu S \partial^\mu S + i\overline{\chi}\partial\!\!\!/\chi + i\overline{N_D}\partial\!\!\!/ N_D - \frac{1}{2}\mu_S^2 S^2 - m_\chi \overline{\chi}\chi - m_N \overline{N_D} N_D \\ &\quad - \left(\lambda^i_{LN}\overline{L^i} N_D H^c + f\overline{N_D} P_{L,R}\chi S + \mathrm{h.c.}\right) - V(H,S)\,, \end{aligned} \tag{6.28}$$

where $\mathcal{L}_{\mathrm{SM}}$ is the SM Lagrangian, H is the SM Higgs doublet, and $H^c \equiv \epsilon H^\star$ is the charge-conjugated field. Notice that the Yukawa terms between N_D, χ, and S describe chiral interactions, however the projector is not yet specified, this will be discussed below. Without loss of generality we assume that the coupling constant f is real and positive. Finally, the scalar quartic potential $V(H,S)$ is given by

$$V(H,S) = \lambda_{HS}\left(H^\dagger H\right) S^2 + \lambda_S S^4\,. \tag{6.29}$$

We will assume that the vev of the field S is zero, hence the Z_2 symmetry is not broken. From equation (6.28), we read that χ is not connected to the Higgs sector and does not gain mass through the Higgs mechanism as the SM fermions do. However, its transformation behaviour under $\mathrm{G_{SM}}$ and Z_2 allows for an explicit mass term m_χ in the Lagrangian. On the other hand, the Dirac fermion N_D does couple to the Higgs field, and therefore gets a mass correction $\propto \left(\lambda^i_{LN}\, v_H\right)^2$ to the explicit mass term m_N. The mass of the scalar after the electroweak symmetry breaking is given by

$$m_S = \sqrt{\mu_S + \lambda_{HS}\, v_H^2}\,, \tag{6.30}$$

with the Higgs vev $v_H \simeq 246\,\mathrm{GeV}$.

In this model, the dark matter particle is described by the lightest matter field which is odd under the Z_2 symmetry and therefore stable. This can be identified either with the scalar S or the Dirac fermion χ. In the first case, the dark matter is produced in the early universe via the Higgs portal [232, 233] and phenomenological imprints are possible in both direct and indirect searches, as in other standard WIMP dark matter scenarios [18]. For this study however, the case where dark matter is represented by the Dirac spinor χ, which carries a non-trivial lepton charge, is more relevant.

We assume that the dark matter has a similar origin as ordinary baryonic matter, i.e. a particle-antiparticle asymmetry is generated at a certain time in the early universe. As discussed in section 3.2.2, there are different possible origins for this asymmetry, however we do

not specify a mechanism and instead impose that almost all of dark matter density today consists of the particle χ. Therefore, the self-annihilation dominates over the particle-antiparticle annihilation. The present-day self-annihilation cross section proceeds via s-wave and reads

$$(\sigma v_{\mathrm{rel}})_0 = \frac{f^4}{64\pi\, m_\chi^2} \frac{(1+\delta_{N\chi})\,\sqrt{\delta_{N\chi}}}{(1-\delta_{S\chi}+\delta_{N\chi})^2}\,. \tag{6.31}$$

For a quantitative comparison with other scenarios we have

$$(\sigma v_{\mathrm{rel}})_0 = \begin{cases} 1.86\times10^{-24} f^4\,\mathrm{cm}^3\,\mathrm{s}^{-1} & \text{for } m_N \ll m_\chi \\ 1.67\times10^{-24} f^4\,\mathrm{cm}^3\,\mathrm{s}^{-1} & \text{for } m_N = 20\,\mathrm{GeV} \end{cases}, \tag{6.32}$$

for $m_\chi = 50\,\mathrm{GeV}$ and $m_S = 100\,\mathrm{GeV}$. That is, if the coupling $f \simeq \mathcal{O}(1)$, the annihilation cross section is $\simeq 2$ orders of magnitude larger than the expected thermal annihilation cross section for thermal relics.

Decay of N_D

Since the Dirac fermions N_D are even under the Z_2 symmetry, they decay into lighter SM particles after being produced. These decays occur through Higgs-mediated, charged current (CC), and neutral current (NC) interactions. The effective Lagrangians for these three interactions read:

$$\mathcal{L}^N_{CC} = -\frac{g_2}{2\sqrt{2}}\overline{e^i_{\mathrm{L}}}\gamma_\mu\Theta_i(1-\gamma_5)N_D W^\mu + \mathrm{h.c.}\,, \tag{6.33}$$

$$\mathcal{L}^N_{NC} = -\frac{g_2}{4c_W}\overline{\nu^i_L}\gamma_\mu\Theta_i(1-\gamma_5)N_D Z^\mu + \mathrm{h.c.}\,, \tag{6.34}$$

$$\mathcal{L}^N_{H} = -\frac{g_2\, m_N}{4m_W}\overline{\nu^i_L}\Theta_i(1+\gamma_5)N_D h + \mathrm{h.c.}\,, \tag{6.35}$$

where W and Z denote the electroweak gauge bosons, h is the Higgs boson, g_2 is the weak coupling, c_W is the cosine of the Weinberg angle θ_W, and $\Theta_i \simeq \lambda^i_{LN}\, v_H/m_N \ll 1$ is the mixing between SM neutrinos and N_D. Indirect and direct searches for sterile neutrinos constrain the mixing Θ_i strongly, c.f. [234–236]. We can identify our model with a type I see-saw scenario with two Majorana neutrinos that form a pseudo-Dirac pair—here this corresponds to N_D. In this generalisation the flavour structure of the coupling is fully determined by the neutrino oscillation data (c.f. [237, 238]). Furthermore, the total lepton charge symmetry is slightly broken, effectively suppressed by the light neutrino mass scale [239–244].

The decay modes of N_D consist of at least one lepton, due to the lepton number conservation, and pseudo-scalar/vector mesons and further leptons in the final state. We show the branching ratios for the different decay channels in the left panel of figure 6.4 under the assumption that N_D couples solely to the third lepton flavour τ. At low energies—when $e^\pm$-pair production is kinematically forbidden ($m_N \lesssim 1\,\mathrm{MeV}$)—the decay channel into three neutrinos $N_D \to 3\nu$ clearly dominates over the second open loop-induced channel $N_D \to \nu_\tau\gamma$. The decay rate of these channels are [236, 245]

$$\Gamma(N_D \to \nu^i\nu^j\overline{\nu^j}) = \frac{G_F^2}{96\pi^3}|\Theta_i|^2 m_N^5\,, \tag{6.36}$$

$$\Gamma(N_D \to \nu^i\gamma) = \frac{9\alpha_{\mathrm{em}}G_F^2}{512\pi^4}|\Theta_i|^2 m_N^5\,, \tag{6.37}$$

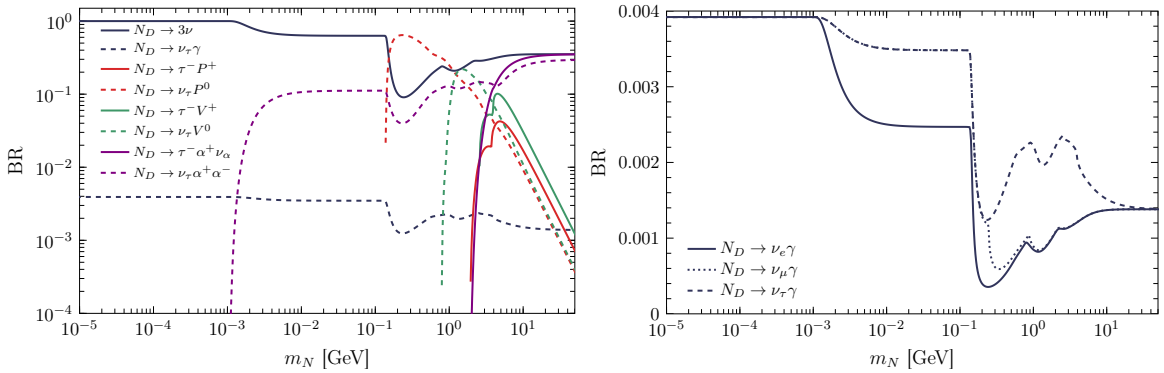

Figure 6.4.: Branching ratios of the (semi-)leptonic decays of the Dirac fermion N_D into SM particles. Left: Here, N_D couples only to the third lepton family. $P^{0,+}$ ($V^{0,+}$) denote kinematically accessible pseudo-scalar (vector) mesons (see e.g. [236]). Right: Radiative decays of N_D for a coupling to each lepton family.

where $G_F \equiv \sqrt{2}g^2/\left(8m_W^2\right)$ is the Fermi coupling constant, α_{em} is the fine-structure constant, and the Dirac fermion N_D couples exclusively to one lepton flavour i. We display in the right panel of figure 6.4 the branching fraction of the radiative decay of N_D for $m_N \leq 50\,\text{GeV}$ for the three cases $i = 1, 2, 3$. The asymptotic values are

$$\text{BR}\left(N_D \to \nu^i\gamma\right) \simeq \begin{cases} 0.0039 & \text{for } m_N \lesssim 1\,\text{MeV} \\ 0.0014 & \text{for } m_\tau \ll m_N \ll 100\,\text{GeV} \end{cases} . \tag{6.38}$$

For $m_N \gg 50\,\text{GeV}$, the decay channels into $W^\pm$, Z, and h are dominant and the channels of interest with a final-state photon are thus suppressed. However, this mass regime opens different indirect detection channels such as soft gamma-ray continuums, positrons, protons, and neutrinos which can reach reasonable fluxes for the corresponding experiments. This analysis presents a promising study and has not yet been carried out.

Spin polarisation α

The spin polarisation α has to be computed from the Lagrangian in equation (6.28) for which we choose, for the sake of simplicity, the left-handed chiral projector P_L. Under this consideration the dark matter annihilation produces mainly right-handed (positive helicity) Dirac fermions N_D. The cross sections in leading order in the dark matter velocity, in the case of fully polarised fermions in the initial and final states, are

$$\sigma v_{\times\times,--} = \frac{f^4}{64\pi m_\chi^2} \frac{\left(1-\sqrt{\delta_{N\chi}}\right)^2 \sqrt{\delta_{N\chi}}}{\left(1-\delta_{S\chi}+\delta_{N\chi}\right)^2} , \tag{6.39}$$

$$\sigma v_{\times\times,++} = \frac{f^4}{64\pi m_\chi^2} \frac{\left(1+\sqrt{\delta_{N\chi}}\right)^2 \sqrt{\delta_{N\chi}}}{\left(1-\delta_{S\chi}+\delta_{N\chi}\right)^2} , \tag{6.40}$$

where the subscripts represent the helicity state of the initial and final particles, with the plus (minus) sign referring to positive (negative) helicities and the cross representing either one.

Following the angular distribution from equation (5.9) and the photon flux from equation (5.6), the radiative decay of a polarised Dirac fermion N_D with positive (negative) helicity

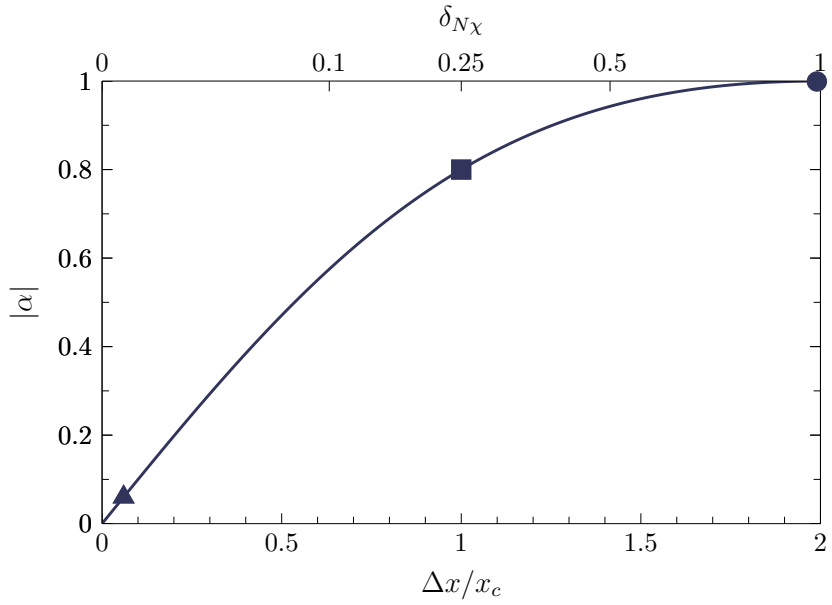

Figure 6.5.: Relation between the mass splitting $\delta_{N\chi}$, or equivalently the relative width of the photon spectrum, with the spin polarisation of the decaying Dirac fermion N_D. We mark the three benchmark scenarios that were used in figure 5.2 and shall be used in the following chapter as reference points for the comparison with model independent limits. These are: $(\delta_{N\chi}, \alpha) = (0.25, 0.8)$ (square), $(\delta_{N\chi}, \alpha) = (0.99, \approx 1)$ (circle) and $(\delta_{N\chi}, \alpha) = (0.001, 0.06 \approx 0)$ (triangle). For the sake of simplicity, we assume a vanishing α for the third benchmark.

produces a photon flux with $\alpha = -1$ ($\alpha = 1$). Therefore, the probability $\mathcal{P}_\pm$ of producing a fermion with positive or negative helicity, considering equations (6.39) and (6.40) is given by

$$\mathcal{P}_\pm = \frac{1}{4}\frac{\sigma v_{--,\pm\pm} + \sigma v_{++,\pm\pm}}{(\sigma v)_0} = \frac{1}{2} \pm \frac{\sqrt{\delta_{N\chi}}}{1+\delta_{N\chi}}\,. \tag{6.41}$$

Notice that this expression is independent of the parameter $\delta_{S\chi}$. Consequently, the resulting photon angular distribution as in equation (5.9) is

$$\begin{aligned}\frac{\mathrm{d}f}{\mathrm{d}\cos\theta^{\mathrm{RF}}} &= \frac{1}{2}\mathcal{P}_+\left(1-\cos\theta^{\mathrm{RF}}\right) + \frac{1}{2}\mathcal{P}_-\left(1+\cos\theta^{\mathrm{RF}}\right) \\ &\equiv \frac{1}{2}\left(1+\alpha\cos\theta^{\mathrm{RF}}\right)\,.\end{aligned} \tag{6.42}$$

This argument follows analogously had we considered the right handed chiral projector P_R in the Lagrangian with the corresponding expressions of equations (6.39) and (6.40). Conclusively, we can express the spin polarisation α in terms of the mass-splitting parameter as

$$\alpha = \pm\frac{2\sqrt{\delta_{N\chi}}}{1+\delta_{N\chi}}\,, \tag{6.43}$$

where the plus (minus) sign corresponds to the chiral Yukawa interaction term with the projector P_R (P_L). We illustrate in figure 6.5 the relation between $|\alpha|$ and $\delta_{N\chi}$, shown in the upper axis, and $\Delta x/x_c$, shown in the lower axis. We highlight the three benchmark points

that used when comparing the model to the model-independent limits derived in the following chapter. Notice that if the Dirac fermion N_D is produced essentially at rest, the photon spectrum flattens: $\delta_{N\chi} \simeq 0 \Rightarrow \alpha \simeq 0$. In this regime however, the spectrum resembles a line since $\Delta x/x_{\rm c} = 2\sqrt{\delta_{N\chi}}$ and is hardly sensitive to α. In contrast if the intermediate fermion is emitted with relativistic velocities the spectrum spans over the full possible range and the spin polarisation is almost maximal $\delta_{N\chi} \simeq 1 \Rightarrow |\alpha| \simeq 1$.

Finally, we discuss the kinematics of this model in the context of gamma-ray boxes and triangles. We identify the intermediate state with the Dirac fermion $\psi = N_D$ and the final state fermion with the neutrinos $X = \nu^i$. This model features an annihilation $\chi\overline{\chi} \to N_D\overline{N_D}$ and a self-annihilation $\chi\chi \to N_D N_D$ mode, the former emitting effectively gamma-ray boxes and the latter triangles[5]. However, due to the particle-antiparticle asymmetry the self-annihilation is dominant and, therefore, the cascade annihilation for this models proceeds as $\chi\chi \to N_D N_D \Rightarrow N_D \to \gamma\nu$. At the energies considered here ($m_\chi \gtrsim 1\,\mathrm{GeV}$) neutrinos are effectively massless, therefore $\delta_{\nu N} = 1$. Furthermore, the other mass-splitting parameter $\delta_{N\chi}$ remains free. In this manner, the pivot $x_{\rm c} = 1/2$ and width parameters $\Delta x/x_{\rm c} = 2\sqrt{\delta_{N\chi}}$ from equation (5.4) are defined, as well as the steepness parameter α in equation (6.43).

[5]In the case of dark matter being mostly composed by the state $\overline{\chi}$, the mirrored self-annihilation channel $\overline{\chi}\,\overline{\chi} \to \overline{N_D}\,\overline{N_D} \Rightarrow \overline{N_D} \to \overline{\nu_i}\gamma$ would be the one give rise to the photon spectrum.

7. Confronting models with gamma-ray data

After discussing the phenomenology of gamma-ray boxes and triangles and the possibility for physical models to realise them, we turn to the discussion on the detectability of these signals in the gamma-ray sky. We focus on the measurements performed by Fermi-LAT and H.E.S.S. and on the projected performance of CTA. Using advanced statistical methods—that we explain at the start of this chapter—we investigate the data within the context of boxes and triangles. We are able to derive strong constraints on the dark matter annihilation cross section from existing experiments. We close this chapter with the projected results on the next generation of IACT.

7.1. Statistical methods

We confront several dark matter signal configurations, against different data sets. For this purpose, we perform a profile likelihood analysis [195,196,246–248] for putative fluxes consisting of a background and a dark matter signal, and derive 95%C.L. upper limits on the dark matter annihilation cross section. This is achieved by analysing different dark matter configurations, constructed by the three phenomenological parameters $(\alpha, \delta_{\eta\chi}, \delta_{X\eta})$ and the dark matter mass m_χ, together with of an educated guess of the total background.

For a proper consideration of the dark matter flux at Earth as seen by a specific telescope we have to account for three separate factors: the field of view, the injection spectrum and the energy resolution of the instrument. From the former two we can calculate the incoming differential gamma-ray flux from dark matter annihilations with a strength set by $S = \langle\sigma v\rangle_0$., observed at a specific region of interest (ROI) observed, as introduced in section 4.2, described by

$$\frac{\mathrm{d}^2\tilde{\Phi}_{\rm ann}}{\mathrm{d}E_\gamma\,\mathrm{d}\Omega}(E_\gamma|S) = \frac{\langle\sigma v\rangle_0}{8\pi\,\kappa\,m_\chi^2}\,m_\chi\,\frac{\mathrm{d}N}{\mathrm{d}E_\gamma}\,\overline{J}_{\rm ann}\,, \tag{7.1}$$

$$\overline{J}_{\rm ann} \equiv \frac{J_{\rm ann}}{\Delta\Omega} \equiv \frac{1}{\Delta\Omega}\int_{\Delta\Omega}\mathrm{d}\Omega\int_{\rm los}\mathrm{d}s\,\rho^2_{\rm dm}\,, \tag{7.2}$$

where $\kappa = 1$ for annihilations between identical particles or $\kappa = 2$ for a particle-antiparticle annihilation, $\mathrm{d}N/\mathrm{d}E_\gamma \equiv m_\chi^{-1}\,\mathrm{d}N/\mathrm{d}x$ is the injection spectrum (c.f. equation (5.6)), $\overline{J}_{\rm ann}$ is the averaged J-factor for a region with solid angle $\Delta\Omega$. Furthermore, we parametrise the injection spectrum of the background background as a function of energy with a generic parameter vector $\mathbf{p}$, the dimension of which depends on the complexity of the background under consideration. Finally, in order to account for the energy and angular reconstruction capabilities of the instrument, discussed in section 4.3, we make a convolution between the incoming flux of the above equation and the resolution of the instrument $R\big(E_\gamma, E'_\gamma\big)$ and multiply by $\Delta\Omega$

$$\frac{\mathrm{d}\Phi_{\rm tot}}{\mathrm{d}E_\gamma}(E_\gamma|\,\mathbf{p}, S) = \int\mathrm{d}E'_\gamma\,R\big(E_\gamma, E'_\gamma\big)\;\Delta\Omega\left(\frac{\mathrm{d}^2\tilde{\Phi}_{\rm ann}}{\mathrm{d}E_\gamma\,\mathrm{d}\Omega}\big(E'_\gamma|\,S\big) + \frac{\mathrm{d}^2\tilde{\Phi}_{\rm bck}}{\mathrm{d}E_\gamma\,\mathrm{d}\Omega}\big(E'_\gamma|\,\mathbf{p}\big)\right), \tag{7.3}$$

where E'_γ is the true energy of the photon, E_γ is the reconstructed energy, and $\mathrm{d}\tilde{\Phi}_{\rm bck}/\mathrm{d}E_\gamma$ is the incoming background flux. We remark that if the width of the gamma-ray box or triangle drops below the resolution of the instrument, their signals are indistinguishable from that of gamma-ray lines; we refer to these cases as line-like boxes or triangles. We show in figure 7.1 the flux as it would be measured by Fermi-LAT with using the IRF P8R2_V6 for different benchmarks. We consider an annihilation cross section of $\langle\sigma v\rangle_0^{2\gamma} = 3\times10^{-26}\,\mathrm{cm}^3\,\mathrm{s}^{-1}$ and the ROI R16 defined later on.

In the likelihood analysis, we compare the measurements of the instrument with the expected flux from equation (7.3). Therefore, we estimate the number of expected counts $n_{\rm exp}$ a telescope with an exposure $\mathcal{E}(E)$ would measure for each bin i, and compare it to the number of observed counts $n_{\rm obs}$. We compute $n_{\rm exp}$ from a photon flux given by $\mathrm{d}\tilde{\Phi}_{\rm tot}/\mathrm{d}E_\gamma = \mathrm{d}\tilde{\Phi}_{\rm bck}/\mathrm{d}E_\gamma + \mathrm{d}\tilde{\Phi}_{\rm ann}/\mathrm{d}E_\gamma$ for bin i using

$$n^i_{\rm exp}(\mathbf{p},S) = \int_{\Delta E_i}\mathrm{d}E_\gamma \int \mathrm{d}E'_\gamma\, R\big(E_\gamma,E'_\gamma\big)\;\mathcal{E}\big(E'_\gamma\big)\;\frac{\mathrm{d}\tilde{\Phi}_{\rm tot}}{\mathrm{d}E_\gamma}\big(E'_\gamma|\,\mathbf{p},S\big)\;. \tag{7.4}$$

Therefore, we perform a profile likelihood analysis with a total of $1+\dim(\mathbf{p})$ degrees of freedom: S and $\mathbf{p}$. For some analyses, we consider only a subset of all the energy bins, those lying within a window of width ϵ defined as

$$E\in\left[\bar{E}/\sqrt{\epsilon},\bar{E}\,\sqrt{\epsilon}\right], \tag{7.5}$$

where the centre $\bar{E}$ is set in a specific position relative to the scales of the dark matter signal.. This technique is called sliding energy window. The likelihood is computed as a product of Poisson probability distributions over the bins under scrutiny

$$\mathcal{L} = \prod_i P\big(n^i_{\rm obs}|n^i_{\rm exp}\big) = \prod_i \frac{(n^i_{\rm exp})^{n^i_{\rm obs}}\exp(-n^i_{\rm exp})}{n^i_{\rm obs}!} \tag{7.6}$$

or

$$-2\,\ln\mathcal{L} = -2\sum_i n^i_{\rm obs}\ln n^i_{\rm exp} - n^i_{\rm exp}\,. \tag{7.7}$$

Since we are interested in maximising the likelihood, we dropped the term $-\ln n^i_{\rm obs}!$ in the last expression, as it is not dependent on $\mathbf{p}$ or S. We define the best fit as the minimum over all parameters of the likelihood $-2\,\ln\mathcal{L}$ and denote it $-2\,\ln\mathcal{L}_{\rm bf}$ with the corresponding parameters $(\mathbf{p}_{\rm bf},S_{\rm bf})$. Furthermore, we also define a profile likelihood $-2\,\ln\mathcal{L}_{\rm prof}(S)$ by minimising the quantity $-2\,\ln\mathcal{L}$ over $\mathbf{p}$ for each value of S, i.e. $-2\,\ln\mathcal{L}_{\rm prof}(S_{\rm bf}) = -2\,\ln\mathcal{L}_{\rm bf}$ is the global minimum of this function. From this profile likelihood, we extract the one-sided 95% confidence level (C.L.) upper limit on the signal strength $S_{\rm ul}$ as $-2\ln\mathcal{L}_{\rm prof}(S_{\rm ul}) = -2\ln\mathcal{L}_{\rm bf}+2.71$, provided $S_{\rm ul} > S_{\rm bf}$ [249]. The best fit of a background-only hypothesis can be obtained straightforwardly as $-2\,\ln\mathcal{L}^0_{\rm bf} = -2\,\ln\mathcal{L}_{\rm prof}(S=0)$. In addition, we compute the test statistic in order to determine the significance of a potential signal

$$TS = -2\left(\ln\mathcal{L}^0_{\rm bf} - \ln\mathcal{L}_{\rm bf}\right)\,. \tag{7.8}$$

In the following sections, we will use these methods in the analysis of potential gamma-ray boxes and triangles in light of existing data or projections for future experiments. Depending on the data under consideration, the details of this analysis may vary, however the essence remains the same.

7.2. Current constraints

In this section, we derive model independent limits on gamma-ray boxes and triangles by performing a profile likelihood analysis using real data from Fermi-LAT and H.E.S.S.. First, we derive model independent limits for a handful of benchmarks described by the phenomenological parameters $(\alpha, \delta_{\eta\chi}, \delta_{X\eta})$ for several dark matter masses m_χ. Then, we study these limits within the context of the models introduced in the previous chapter and discuss the results.

7.2.1. Measurements by Fermi-LAT and H.E.S.S.

For the dark matter profile, we restrict ourselves to an Einasto profile as defined in equation (3.17), recalling the parameters $\alpha = 0.17$, $r_s = 20\,\mathrm{kpc}$, $\rho_0 = 0.4\,\mathrm{GeV\,cm^{-3}}$, and $R_0 = 8.5\,\mathrm{kpc}$. We remark that the dark matter density distribution is a major source of uncertainties for indirect detection. However, a comprehensive analysis on the impact of differing profiles lies outside the scope of this work, instead we work with the fiducial Einasto profile for the sake of simplicity. For our purposes, we studied the following data sets from Fermi-LAT and H.E.S.S..

Fermi-LAT 2011 [202,246]. We investigate the ROI labelled "Center" defined in table 1 of reference [246], for which the averaged J-factor is given by $\overline{J}_{\mathrm{ann}} = 1.11 \times 10^{23}\,\mathrm{GeV^2\,cm^{-5}}$. We employ gamma-ray data between 1 and 300 GeV with a mean exposure of $\langle \mathcal{E} \rangle = 7.9 \times 10^{10}\,\mathrm{cm^2\,s\,sr}$, obtained during 2.3 yrs of data taking between the years 2008 and 2011. The resolution of the instrument for this specific data set is modelled after the Pass7_V15 performance, as described in reference [250], which features typical values between 6.8% and 11%.

Fermi-LAT 2015 [251, 252]. Using the publicly available Fermi-LAT gamma-ray data [251], we extract three different data sets corresponding to different ROIs. These data sets encompass energy values between 1 and 500 GeV and were taken between Aug 4, 2008 (MET 239557414) and Aug 5, 2014 (MET 428889603)[1]. The events that enter our main analysis are taken from the PASS 8 SOURCE event class. During our data selection processes, we also employ standard cuts for diffuse analysis including zenith angle $< 90°$, as well as the quality cut filter "DATA-QUAL = 1, LATCONFIG = 1". Then we use Fermi Science Tools (v10r0p5) [253] to calculate the corresponding exposure maps. The three different ROIs are: a squared $2° \times 2°$ region centred at the GC (2x2), a circular $3°$ region around the GC (R3), and a circular $16°$ region around the GC with with $|b| \leq 5°$ and $|l| \geq 6°$ masked out (R16). Region 2x2 will be helpful for a comparison with the estimated prospects for CTA derived in the following section, whereas regions R3 and R16 are inspired by analyses performed by the Fermi-LAT collaboration [254]. The averaged J-factors for the regions 2x2, R3, and R16 read $\overline{J}_{\mathrm{ann}} = 8.36 \times 10^{24}\,\mathrm{GeV^2\,cm^{-5}}$, $\overline{J}_{\mathrm{ann}} = 3.51 \times 10^{24}\,\mathrm{GeV^2\,cm^{-5}}$, and $\overline{J}_{\mathrm{ann}} = 5.12 \times 10^{23}\,\mathrm{GeV^2\,cm^{-5}}$. The mean exposures of the data sets are $\langle \mathcal{E} \rangle = 2.94 \times 10^8\,\mathrm{cm^2\,s\,sr}$, $\langle \mathcal{E} \rangle = 2.18 \times 10^9\,\mathrm{cm^2\,s\,sr}$ and $\langle \mathcal{E} \rangle = 4.69 \times 10^{10}\,\mathrm{cm^2\,s\,sr}$ for the regions 2x2, R3 and R16, respectively. The resolution of the Fermi-LAT adopted for the study of these data sets follows the Pass8_R2_V6 performance as described in reference [250], which features typical values between 6.2% and 27.7%.

H.E.S.S. 2013 [191, 255]. For the data based on the observations performed by H.E.S.S., we investigate the Central Galactic Halo (CGH) defined by a circular $1°$ region around the GC

[1] We thank Xiaoyuan Huang for kindly facilitating the access to this data sets using the Fermi Science Tools.

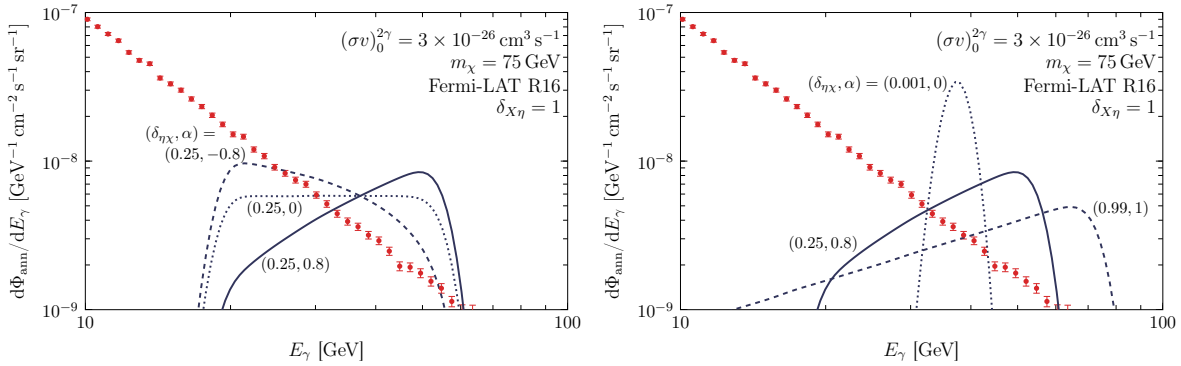

Figure 7.1.: Photon flux from dark matter annihilations of the form $\chi\chi \to \eta\eta \to 2\gamma$ for different benchmarks of the phenomenological parameters, a strength $(\sigma v)_0^{2\gamma} = 3 \times 10^{-26}\,\mathrm{cm^3 s^{-1}}$, and mass $m_\chi = 75\,\mathrm{GeV}$. Notice that some of these values are taken from figure 5.2. In contrast, the Fermi-LAT data is shown from region R16 as described in the text. For the correct consideration of the signal, a convolution is performed between the emitted flux and the resolution of the instrument using the IRF P8R2_V6.

with $|b| > 0.3°$. The averaged J-factor for this region is $\overline{J}_{\mathrm{ann}} = 7.78 \times 10^{24}\,\mathrm{GeV^2\,cm^{-5}}$. This data set complements the ones from Fermi-LAT in the high energy regime, extending from 500 GeV up to 25 TeV, with a mean exposure of $\langle \mathcal{E} \rangle = 2.20 \times 10^{11}\,\mathrm{cm^2\,s\,sr}$. The resolution of H.E.S.S. is assumed to vary log-linearly from 17% at 500 GeV down to 11% at 10 TeV, in accordance with reference [255].

7.2.2. Upper limits

After introducing the details on the experimental part, we set out to derive upper limits on the velocity averaged annihilation cross section using the profile likelihood method. Concretely, we analyse the process $\chi\chi \to \eta\eta$ followed by $\eta \to X\gamma$, the latter with a branching fraction of 100%. The total amount of photons per annihilation is then $N_\gamma = 2$, we denote the cross section in the present day universe for this particular process as $\langle \sigma v \rangle_0^{2\gamma}$. For illustration purposes, we plot in figure 7.1 the flux as measured by Fermi-LAT for the region R16 and box and triangle signals, properly convolved, for several dark matter benchmarks, with a nominal cross-section. Here, it is evident that gamma-ray boxes and triangles differ starkly from the standard measurements usually approximated as power laws. Even the less evident falling down-triangle, which is much softer than its counterparts, displays a harder spectrum than the measured one. Furthermore, we see the cross section used for these signals is clearly excluded, which is of particular interest for particle physics models where dark matter is described as a thermal relic.

For the likelihood analysis with the Fermi-LAT data, we assume a simple power-law background with normalisation A and power index γ

$$\frac{\mathrm{d}\tilde{\Phi}_{\mathrm{bck}}^{\mathrm{LAT}}}{\mathrm{d}E_\gamma} = A \left(\frac{E_\gamma}{1\,\mathrm{GeV}} \right)^{-\gamma} . \tag{7.9}$$

Furthermore, we make use of the sliding window technique and position the windows at the right end of the unresolved signal $\bar{E} = E^+ \equiv m_\chi\, x^+$, with a width given by $\epsilon = 1.5, 2.0, 2.3$ which correspond to 2σ intervals for instruments with energy resolution between 10% up to 20%. We make use of this technique because the complete energy range of Fermi-LAT is

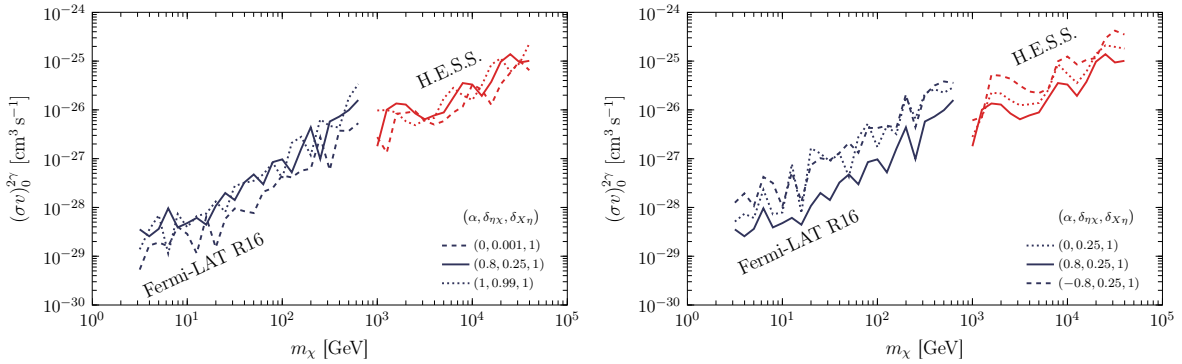

Figure 7.2.: One-sided 95% CL upper limits on the dark matter annihilation cross section into two photons against the dark matter mass. We use the same benchmark parameters $(\alpha, \delta_{\eta\chi}, \delta_{X\eta})$ as in figure 7.1. The blue and red lines correspond to limits derived using Fermi-LAT and H.E.S.S. data, respectively. The style of the lines as described in the legend applies for both sets.

not well fitted by a single power law, however smaller fractions are well described by such a parametrisation.

The likelihood analysis for the H.E.S.S. data is performed using a seven-parameter modulated power law background adapted from reference [191], given by

$$\frac{\mathrm{d}\Phi_{\mathrm{bck}}^{\mathrm{HESS}}}{\mathrm{d}E_\gamma} = a_0 \left(\frac{E_\gamma}{1\,\mathrm{TeV}}\right)^{-\gamma} \left[P(x) + \beta\, G\,(x)\right] , \tag{7.10}$$

with

$$P(x) = \exp\left(a_1\, x + a_2\, x^2 + a_3\, x^3\right) , \tag{7.11}$$

$$G\,(x) = \frac{1}{\sigma_x\,\sqrt{2\pi}} \exp\left(-\frac{(x-\mu_x)^2}{2\sigma_x^2}\right) , \tag{7.12}$$

and $x = \log_{10}\left(E_\gamma/1\,\mathrm{TeV}\right)$. This parametrisation models the background as observed by the instrument, therefore the convolution with the response of the instrument from equation 7.3 is only needed for the dark matter signal. For this analysis we use the full energy range without energy windows. We remark that performing the sliding energy window method using a simple power-law background on the H.E.S.S. data yields results very similar (within a factor $\simeq 2$) to those obtained by the more complex modulated power law.

Model independent limits

We present in figure 7.2 the 95%C.L. upper limits on the annihilation cross section $\langle\sigma v\rangle_0^{2\gamma}$ for the benchmarks presented in figure 7.1. These are gamma-ray boxes and triangles with varying width and slope. The limits depicted here were done using the Fermi-LAT R16, and the H.E.S.S. data sets as introduced previously. The robustness of these results for differing window widths and positionings was tested showing that no strong dependence on this parameters is present. Therefore, we restrict ourselves to a window width $\epsilon = 2.0$ and a centre the windows at $\bar{E} = E^+$. We also derived limits for the other data sets, R3, 2x2, and Fermi 2011, however these results were weaker up to a factor $\simeq 50$ To avoid cluttering, we present only the

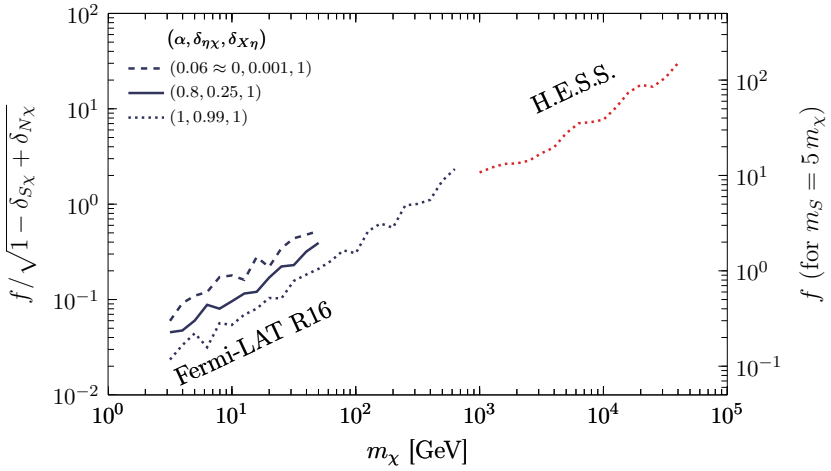

Figure 7.3.: One-sided 95% CL upper limits on the coupling f of model C, for the same phenomenological parameters $(\alpha, \delta_{\eta\chi}, \delta_{X\eta})$ as in the left panel of figure 7.2. The left axis shows limits for a generic value of $\delta_{S\chi}$. Furthermore, the annihilation cross section is proportional to this full expression, c.f. equation (6.31). The right axis shows the scale for the particular case $m_S = 5\,m_\chi$. In this case, the coupling f becomes non-perturbative for $m_\chi \gtrsim 1.3\,\text{TeV}$.

(strongest) results, from the analysis of R16. The complementarity between both Fermi-LAT and H.E.S.S. is remarkable covering almost five orders of magnitude of the dark matter mass range, from a few times 1 GeV up to several tens of TeV, without gaps. Due to usual statistical fluctuations, the limits derived with the profile likelihood analysis present jagged features.

The values for the phenomenological parameters are inspired in the ADM model C as introduced in the previous chapter, where a relation between α and $\delta_{\eta\chi}$ is established by equation (6.43). For the sake of simplicity, we consider a constant value for the the mass splitting parameter $\delta_{X\eta} = 1$. In the left panel, we show limits on signals with different width, and the corresponding steepness. In the right panel, we present limits with varying steepness and a constant width. We see that the strongest constraints are derived from the configuration $(\alpha, \delta_{\eta\chi}, \delta_{X\eta}) = (0, 0.001, 1)$, that is a line-like gamma-ray box/triangle. This is an intuitive result, since sharp features are also the most prominent ones, as shown in figure 7.1. Notice that in practice, line-like boxes or triangles are indistinguishable from another, since the slope is washed out by the resolution of the instrument. However, the limits for wider signals do not worsen significantly, despite their dimmer flux. This is due to the fact that wider signals extend to higher energies, where the expected background flux is far fainter. Therefore, the resulting limits are also rather strong. In the right panel of figure 7.2, we recognise that up-triangles lead to the strongest results. Again, this is an intuitive result, since up-triangles predict a larger flux at higher energies, an effect clearly visible in figure 7.1. Although the signals of the down-triangle and box scenarios are not as hard as in the up-triangle case, the limits obtained from these set-ups are still quite strong. These results are remarkable, ranging from $\langle \sigma v_{\text{rel}} \rangle_0^{2\gamma} \simeq 10^{-29}\,\text{cm}^3\,\text{s}^{-1}$ for low dark matter masses up to $\langle \sigma v \rangle_0^{2\gamma} \simeq 10^{-25}\,\text{cm}^3\,\text{s}^{-1}$ at several tens of TeV masses. Finally, we remark that an active search of gamma-ray boxes and triangles was performed, by computing the TS value. Some configurations with small dark matter masses $m_\chi < 10\,\text{GeV}$ yielded a TS value larger 23.7, which corresponds to a local significance $> 5\sigma$ [246]. Still, considering the large amount of trials, the global significance of these occurrences is small. Furthermore, the effect smeared for narrower energy windows.

Limits on specific models

We show in figure 7.3 the upper bound on the coupling f of model C from equation (6.31), described in the previous chapter. These constraints are obtained using our analysis on the Fermi-LAT and H.E.S.S. observations, under the assumption that the Dirac fermion N_D couples with the same strength to all neutrino flavours. In the left vertical axis we report a quantity which depends on the parameters f, $\delta_{N\chi}$, and $\delta_{S\chi}$, to which the cross section is proportional. In the right vertical axis, we assume $m_S = 5m_\chi$ ($\delta_{S\chi} = -24$) and present the limits on the coupling f. The limits shown in the right panel of figure 7.2 are well suited for the analysis of model C as the parameters α and $\delta_{\eta\chi}$ fulfil equation (6.43). Let us notice that the limits in this figure also consider a branching fraction into photons, i.e. in the current notation

$$(\sigma v_{\rm rel})_0^{2\gamma} = (\sigma v_{\rm rel})_0 \sum_i \mathrm{BR}(N_D \to \nu_i \gamma) \ . \tag{7.13}$$

The decay modes of N_D into photons is strongly dependent on its mass as observed in figure 6.4, therefore we impose $m_N \leq 50\,\mathrm{GeV}$ in order to close kinematically the decay modes into electroweak gauge bosons. Since we consider cases with constant $\delta_{N\chi}$, this has immediate repercussions on the range of the dark matter mass m_χ. Therefore, we have $m_\chi \lesssim 50(58)\,\mathrm{GeV}$ for $\delta_{N\chi} \simeq 0(0.25)$, the limits of which are shown as a dashed(solid) line in figure 7.3. Conversely, for the wide case ($\delta_{N\chi} \simeq 1$) the full mass range is allowed since the the Dirac neutrino remains effectively massless. In contrast to the model independent limits, the strongest limits for the coupling f come from the cases where $\delta_{N\chi} \simeq 1$. This can be explained by the dependence of the cross section on this mass-splitting parameter as $(\sigma v_{\rm rel})_0^{2\gamma} \propto (\sigma v_{\rm rel})_0 \propto \sqrt{\delta_{N\chi}} \propto |\alpha|$. Finally, we remark that in the case $m_S = 5m_\chi$ shown in the right axis of the figure the coupling becomes non-perturbative, $f \gtrsim 4\pi$, for $m_\chi \gtrsim 1.3\,\mathrm{TeV}$.

7.3. Prospects for future experiments

As introduced in chapter 4, the upcoming CTA [206, 207]—a next-generation IACT—promises a major improvement on the very high energy gamma-ray astronomy. Using existing designs and projections for the performance of the instrument (for details see section 4.3.3) and sensible modelling of the background, we derive a realistic sensitivity reach and upper limits as expected for the CTA instrument on the dark matter annihilation cross section into photons. In particular, we focus on the production of gamma-ray boxes via the process $\chi\chi \to \phi\phi$ followed by $\phi \to \gamma\gamma$, i.e. a total of $N_\gamma = 4$ photons per annihilation and a fixed parameter $\delta_{X\eta} = \delta_{\gamma\phi} \equiv 1$. We denote the cross section for this particular scenario as $(\sigma v_{\rm rel})_0^{4\gamma}$. For this study, we use the 2x2 region defined in the previous section, i.e. $|l| \leq 1^\circ$ and $|b| \leq 1^\circ$. Furthermore, we assume an observation time of $\Delta t = 100\,\mathrm{h}$—a sensible amount of time given the general interest on this region—, and an effective area and resolution, both depicted in figure 4.5. We adopt the Einasto, NFW, cuspy, and cored profiles as defined in equations (3.16) and (3.17), with J-factors $\overline{J}_{\rm ann} = 1.02 \times 10^{22}, 6.34 \times 10^{24}, 3.63 \times 10^{22}, 1.60 \times 10^{20}\,\mathrm{GeV^2\,sr\,cm^{-5}}$, respectively. In the following sections, we discuss in detail the background we modelled for this study and the results of the analysis.

7.3.1. Background modelling

Indirect searches performed with IACTs are hindered by three kinds of backgrounds: gamma-rays of astrophysical origin, electrons and misidentified hadronic cosmic rays. We estimate, in

a conservative manner, the fluxes of these particles as expected to be observed by CTA, based on measurements carried out by other experiments.

Hadronic cosmic rays Showers triggered by cosmic nuclei—most of them protons—emit Cherenkov light which can be misread as if it were originated by an inbound photon (or electron). Although it is possible to discriminate between hadronic and electromagnetic showers—for a 70% gamma-ray acceptance typical hadron acceptances lie between 1% and 20% [256]—the proton flux largely outnumbers that of photons, contributing considerably to the background. We parametrise the proton flux as a power law, following reference [257], as

$$\frac{\mathrm{d}^2\Phi_p}{\mathrm{d}E_p\,\mathrm{d}\Omega} = 8.73\times10^{-6}\left(\frac{E_p}{\mathrm{TeV}}\right)^{-2.71}\mathrm{TeV}^{-1}\,\mathrm{cm}^{-2}\,\mathrm{s}^{-1}\,\mathrm{sr}^{-1}\,, \tag{7.14}$$

which provides a well suited description to a wide set of data prior to 2002 for a wide energy range starting at 10 GeV up to 1 EeV. Considerations on the latest proton data [258] show that this parametrisation remains valid, differing minimally from a best-fit for these data. The reconstructed photon energy from a misread proton does not correspond to the true energy of the proton, giving way to a disagreement of a factor $\rho \simeq 2-3$ at a primary energies of $E_0 = 100\,\mathrm{GeV}$. This is due to the Cherenkov yield of the different showers, both of which are proportional to E_0 [259]. In other words, a shower initiated by a proton with an energy E_p can be accidentally interpreted as a photon with a primary energy $E_\gamma \simeq E_p/\rho$. Although possible, a strict discrimination between these showers is far more complex and requires the analysis of a larger set of parameters [259]. Bearing this in mind, we use a constant factor $\rho = 3$ for the rest of this work.

Electrons and positrons Electrons and positrons induce showers which are nearly indistinguishable from those initiated by photons with the same energy. Only a tiny displacement of the shower maxima can discriminate one case from the other [260]. Therefore, the large electron-positron flux contributes substantially to the gamma-ray background as observed by IACTs. We parametrise this background based on precision measurements carried out by AMS-02 [261] and by H.E.S.S. [260], the former for energies below several hundred GeV and the latter at TeV energies. Both parametrisations are described by power laws with different norms and power indices; we have for the energies above 30.2 GeV

$$\frac{\mathrm{d}^2\Phi_e^{\mathrm{le}}}{\mathrm{d}E_e\,\mathrm{d}\Omega} = 9.93\times10^{-9}\left(\frac{E_e}{\mathrm{TeV}}\right)^{-3.17}\mathrm{TeV}^{-1}\,\mathrm{cm}^{-2}\,\mathrm{s}^{-1}\,\mathrm{sr}^{-1} \tag{7.15}$$

in agreement with AMS-02 data. For higher energies we use

$$\frac{\mathrm{d}^2\Phi_e^{\mathrm{he}}}{\mathrm{d}E_e\,\mathrm{d}\Omega} = 1.17\times10^{-8}\left(\frac{E_e}{\mathrm{TeV}}\right)^{-3.9}\mathrm{TeV}^{-1}\,\mathrm{cm}^{-2}\,\mathrm{s}^{-1}\,\mathrm{sr}^{-1}\,, \tag{7.16}$$

in agreement with H.E.S.S. data. The full-range description is obtained using the generalised mean with exponent $p = -2$ of both parametrisations

$$\frac{\mathrm{d}^2\Phi_e}{\mathrm{d}E_e\,\mathrm{d}\Omega} = \left[\left(\frac{\mathrm{d}^2\Phi_e^{\mathrm{le}}}{\mathrm{d}E_e\,\mathrm{d}\Omega}\right)^{-2} + \left(\frac{\mathrm{d}^2\Phi_e^{\mathrm{he}}}{\mathrm{d}E_e\,\mathrm{d}\Omega}\right)^{-2}\right]^{-\frac{1}{2}}\,, \tag{7.17}$$

ensuring a smooth transition between the two regimes.

Astrophysical gamma rays Lastly, we address the gamma-ray flux of astrophysical origin CTA is expected to observe, which limits the capability to pinpoint gamma-rays originated from dark matter processes. This contribution is highly dependent on the election of the ROI, and can only be reduced by a wise choice of the target field of view and analysis technique. As stated previously, this work studies the gamma-ray emission of a $2^\circ \times 2^\circ$ region centred at the GC, a ROI where the two main gamma-ray sources are the Galactic Ridge (GR) emission concealed in the region defined by $|l| < 0.8^\circ$ and $|b| < 0.3^\circ$ and a point source coincident with the GC. The former has been measured by H.E.S.S. [262] to which the parametrisation

$$\frac{\mathrm{d}^2\Phi_{\gamma,\mathrm{gr}}}{\mathrm{d}E_\gamma\,\mathrm{d}\Omega} = 1.73\times10^{-8}\left(\frac{E_\gamma}{\mathrm{TeV}}\right)^{-2.29}\ \mathrm{TeV}^{-1}\,\mathrm{cm}^{-2}\,\mathrm{s}^{-1}\,\mathrm{sr}^{-1}\,. \tag{7.18}$$

provides a good description. The latter is a point source that within the resolution of the instruments is coincidental to the GC, which has been observed by H.E.S.S. and Fermi-LAT. In the range $5-100\,\mathrm{GeV}$, the energy spectrum is well fitted by [263]

$$\frac{\mathrm{d}\Phi^{\mathrm{le}}_{\gamma,\mathrm{gc}}}{\mathrm{d}E_\gamma} = 1.11\times10^{-12}\left(\frac{E_\gamma}{\mathrm{TeV}}\right)^{-2.68}\ \mathrm{TeV}^{-1}\,\mathrm{cm}^{-2}\,\mathrm{s}^{-1}\,; \tag{7.19}$$

and in the range $160\,\mathrm{GeV}-30\,\mathrm{TeV}$ by [264]

$$\frac{\mathrm{d}\Phi^{\mathrm{he}}_{\gamma,\mathrm{gc}}}{\mathrm{d}E_\gamma} = 2.34\times10^{-12}\left(\frac{E_\gamma}{\mathrm{TeV}}\right)^{-2.25}\ \mathrm{TeV}^{-1}\,\mathrm{cm}^{-2}\,\mathrm{s}^{-1}\,. \tag{7.20}$$

Similar to the case of electrons, we use a generalised mean, with exponent $p=5$ to describe the spectrum over full energy range as

$$\frac{\mathrm{d}\Phi_{\gamma,\mathrm{gc}}}{\mathrm{d}E_\gamma} = \left[\left(\frac{\mathrm{d}\Phi^{\mathrm{le}}_{\gamma,\mathrm{gc}}}{\mathrm{d}E_\gamma}\right)^5 + \left(\frac{\mathrm{d}\Phi^{\mathrm{he}}_{\gamma,\mathrm{gc}}}{\mathrm{d}E_\gamma}\right)^5\right]^{\frac{1}{5}}\,. \tag{7.21}$$

Lastly, the resulting total background from the different sources as discussed above, is described by

$$\begin{aligned}\frac{\mathrm{d}\Phi_{\mathrm{bkg}}}{\mathrm{d}E_\gamma}(E_\gamma) &= \Delta\Omega_{2\times2}\left(\epsilon_p(E_\gamma)\rho\frac{\mathrm{d}^2\Phi_p}{\mathrm{d}E_p\,\mathrm{d}\Omega}(\rho E_\gamma) + \epsilon_e\frac{\mathrm{d}^2\Phi_e}{\mathrm{d}E_e\,\mathrm{d}\Omega}(E_\gamma) + \epsilon_\gamma\frac{\mathrm{d}^2\Phi_{\gamma,\mathrm{gr}}}{\mathrm{d}E_\gamma\,\mathrm{d}\Omega}(E_\gamma)\right)\\ &+ \epsilon_\gamma\frac{\mathrm{d}\Phi_{\gamma,\mathrm{gc}}}{\mathrm{d}E_\gamma}(E_\gamma)\,,\end{aligned} \tag{7.22}$$

where $\Delta\Omega_{2\times2} = 1.22\times10^{-3}\,\mathrm{sr}$ is the solid angle of the 2x2 region. We remark that equation (7.22) is a conservative up-scale of the modelled flux for the Galactic ridge to our target field of view, assuming the same output per unit solid angle. The cosmic-ray background rate described by the equation above is in agreement with the one reported in figure 16 of reference [208] within a factor $1.5-3$ if we take an energy dependent proton acceptance described by $\epsilon_p(E_\gamma) = 0.01 + 0.02\,(E_\gamma/20\,\mathrm{TeV})^{1.4}$—i.e. a proton acceptance $\epsilon_p(1\,\mathrm{TeV}) \simeq 0.01$ that scales up to $\epsilon_p(100\,\mathrm{TeV}) \simeq 0.20$. Considering an updated performance [209], the same result is obtained with a proton acceptance of $\epsilon_p(E_\gamma) = 0.001 + 0.002\,(E_\gamma/20\,\mathrm{TeV})^{1.4}$. Finally, we note that this modelled background is also in agreement with that of reference [265], performed by a full CTA simulation. We show in the left panel of figure 7.4 the background as modelled in the

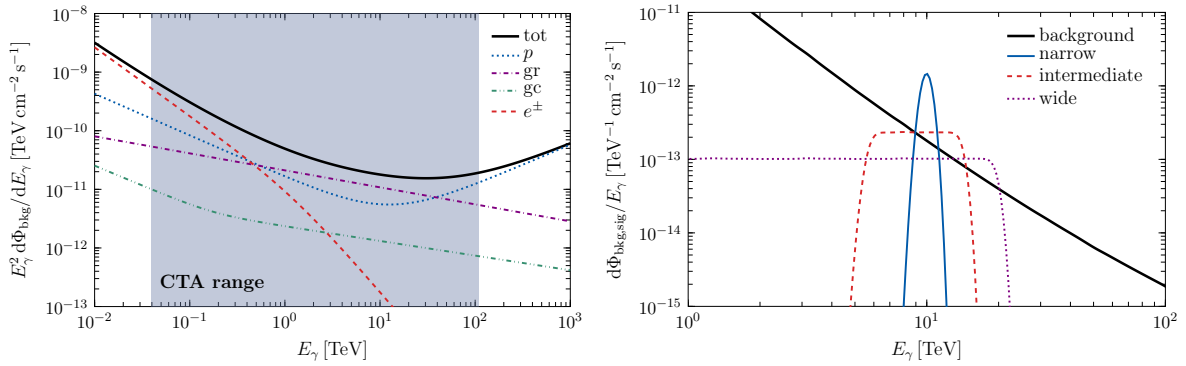

Figure 7.4.: Modelled background as it would be observed by CTA within the 2x2 region as described by equation (7.22). Left: Breakdown of the total background into protons, electrons, and gamma rays, for details see text. Right: Total background and gamma-ray boxes as produced by dark matter models with $m_\chi = 20\,\mathrm{TeV}$, $\delta_{\phi\chi} = 0.002, 0.19, 0.99$, and $\alpha = 0$, assuming an annihilation cross section $\langle\sigma v\rangle_0^{4\gamma} = 10^{-24}\,\mathrm{cm}^3\,\mathrm{s}^{-1}$ and an Einasto density distribution. Both signals are depicted under the consideration of the energy resolution of the instrument from the Monte Carlo design study [208]. Figures taken from [8].

previous paragraphs and summarised in equation (7.22). The contributions of each separate source as well as the total sum are depicted. At lower energies the background is dominated by the contribution from electrons and positrons. This holds up to a few TeV where the diffuse emission from the galactic ridge and eventually cosmic protons overshadow the other sources. For comparison with the signals produced by gamma-ray boxes—that shall be studied further down—, we present in the right panel of figure 7.4 this background with the flux predicted by a cascade scenario producing boxes with the parameters $m_\chi = 20\,\mathrm{TeV}$, $\langle\sigma v\rangle_0^{4\gamma} = 10^{-24}\,\mathrm{cm}^3\,\mathrm{s}^{-1}$ and mass splittings of $\delta_{\phi\chi} = 0.002, 0.19, 0.99$.

7.3.2. Upper limits and sensitivity

From the considerations above and using the profile likelihood method, we can infer the prospects for CTA in the search for gamma-ray boxes. In the case of a non-observation, we estimate the upper limits on the annihilation cross section and the sensitivity reach otherwise. For the estimation of the upper limits, we generate 300 sets of mock data based on the background-only hypothesis—drawn from a Poisson distribution with a mean n_{exp}, given by equation (7.4). Using the profile likelihood method, we draw one-sided 95%C.L. limits on benchmark scenarios described by the parameters $(m_\chi, \delta_{\phi\chi})$. For the estimation of the sensitivity reach, we generate 300 sets of mock data, calculated assuming non-zero signal (with fixed parameters $(m_\chi, \delta_{\phi\chi})$) and background. Starting with a very small signal strength, we increase its normalisation repeatedly, calculating each time the TS value from equation (7.8), over all 300 realisations. Then, we obtain the 5σ sensitivity reach given by the smallest annihilation cross section for which the averaged TS value is larger than 23.7, (see e.g. [246]).

Considering the energy regime of CTA, we simulate mock data for energies within the range $E_\gamma = 40\,\mathrm{GeV} - 110\,\mathrm{TeV}$. Then, we bin the resulting data into $N_b = 200$ energy bins per decade. This simulation is performed using the effective area A_{eff} and energy resolution σ_E as presented in figure 4.5. Further details on the particular CTA set-up considered are presented in section 4.3.3.

In order to distinguish a putative signal from the background, it is crucial to ensure a proper

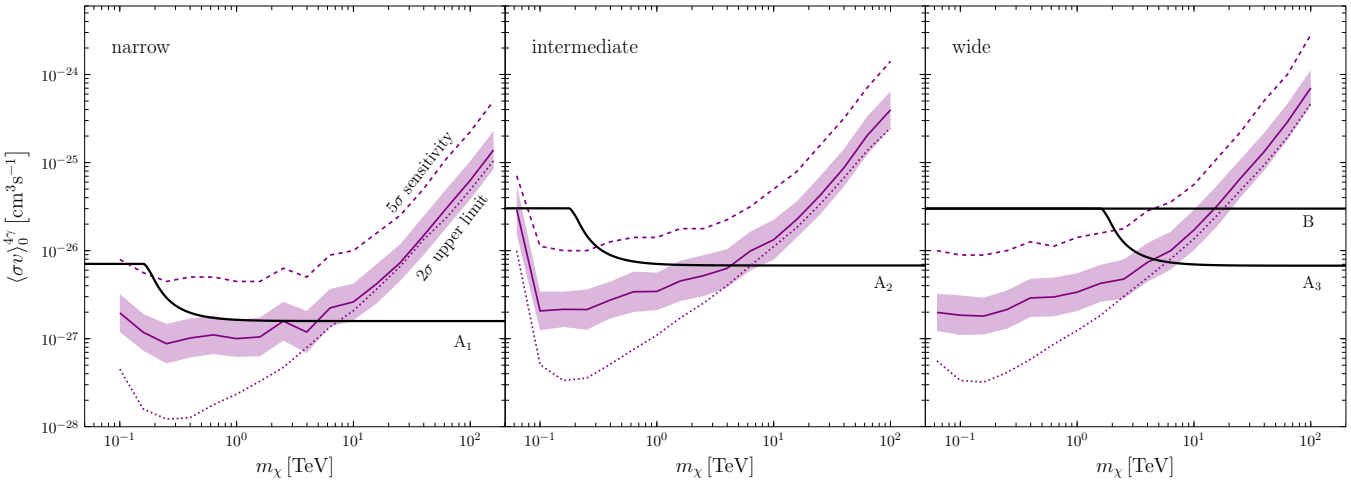

Figure 7.5.: Upper limits and sensitivity reach for gamma-ray boxes expected from $\Delta t = 100\,\mathrm{h}$ of observations performed by CTA of region 2x2, assuming an Einasto dark matter profile, a vanishing gamma-ray optical depth and a window width ϵ_2 The different panels refer to narrow, intermediate, and wide cases from left to right. The violet solid lines depict the average 95% CL upper limits on the annihilation cross section over 300 mock data sets, and the band the corresponding standard deviation. The 5σ sensitivities are indicated by the dashed lines. These results were obtained using the performance from the design study [208]. The 95% CL upper limits using the updated CTA performance [209] is depicted as dotted lines. The thick solid lines represent the target cross sections for thermal relics in models $\mathrm{A}_{1,2,3}$ and B.

model for the simulated mock data. Since, a simple power-law parametrisation provides no good fit throughout the full energy range, we make use of the sliding window energy technique on the binned data. The windows are centred at the right end of the unconvolved dark matter signal $\bar{E} = E^+$, as were the limits drawn using Fermi-LAT data. For the estimation of proper window sizes, we examine widths within the range $\epsilon = 1.2 - 10$ centred over the complete CTA energy range. We compute the χ^2 values of all 300 sets of background-only mock-data sets—derived using the background as modelled in equation (7.22)—for the best-fit power laws. Then, we test whether this distribution could be drawn by a χ^2 distribution, and reject widths for which the p-value of this distribution test is less than 0.01. We choose as our default window width $\epsilon_2 = 2$, being the largest one which fulfils this criterion and, for completeness, we also study $\epsilon_{1.2} = 1.2$ and $\epsilon_{1.5} = 1.5$.

The effects of the non-transparency of the universe to high-energy gamma rays are also examined by including in the analysis an energy dependent J-factor as well. For this we recall the discussion on the optical depth from section 4.2.1 and cast the energy dependent J-factor J^τ_{ann} from equation (4.13). We invoke the ISF as found in [266, 267] at Galactocentrc radii $R = 0, 4, 12, 16\,\mathrm{kpc}$. The considerations of this effect—in this study—lead to ratios between the modified and usual J-factors of $J^\tau_{\mathrm{ann}}/J_{\mathrm{ann}} \simeq 1, 0.99, 0.75, 0.35$ for $E_\gamma = 10\,\mathrm{GeV}, 1\,\mathrm{TeV}, 100\,\mathrm{TeV}, 1000\,\mathrm{TeV}$. Lastly, we restrict our study to three dark matter benchmark scenarios, given by $\delta_{\phi\chi} = 0.002, 0.19, 0.99$, labelled narrow, intermediate, and wide, respectively. These box cases are the ones depicted in the right panel of figure 7.4.

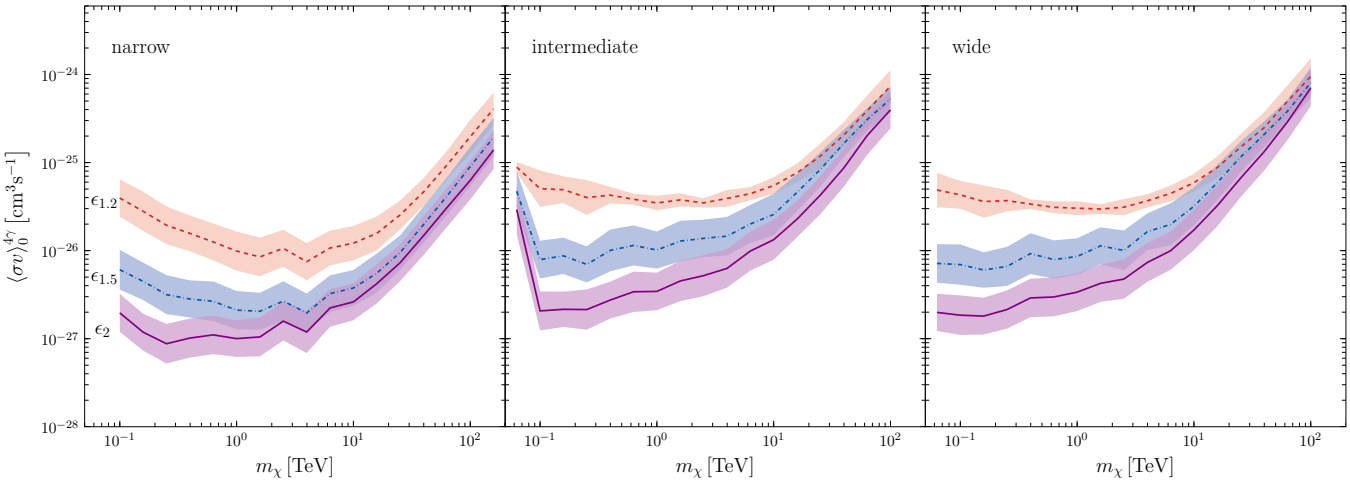

Figure 7.6.: Effects of the variation of the window width on the upper limits from the profile likelihood analysis. The panels, read from left to right, correspond to narrow, intermediate, and wide boxes. Each panel shows the results for the window widths $\epsilon_{1.2}$, $\epsilon_{1.5}$, and ϵ_2. Further details mimic the ones adopted in figure 7.5 for the CTA performance from [208].

Results

We start our discussion on the results with the limits for each scenario and the 5σ sensitivity reach expected for CTA, shown in figure 7.5. The default energy window width ϵ_2 and the Einasto profile are used. The curves represent the logarithmic mean of the results obtained from the 300 mock-data sets on the one-sided 95%C.L. upper limits, and the band the standard deviation—which turned out to be within a factor of $2-3$ above or below the mean—based on the performance of reference [208] for a vanishing gamma-ray optical depth. The limits are the strongest for dark matter masses between 100 GeV and $10-20$ TeV, excluding annihilation cross sections above a few times $10^{-27}\,\mathrm{cm}^3\,\mathrm{s}^{-1}$. For most of the remaining mass range, the upper limits cover values for $(\sigma v_{\mathrm{rel}})_0^{4\gamma}$ smaller than a few times $10^{-26}\,\mathrm{cm}^3\,\mathrm{s}^{-1}$ for the narrow case, and a few times $10^{-25}\,\mathrm{cm}^3\,\mathrm{s}^{-1}$ for the intermediate and wide cases. The dashed lines represent the 5σ sensitivity reach, which lay a factor $3-5$ above the 95%C.L. upper limits for the full mass range. At face value, the three benchmarks are very similar, as argued when discussing the results derived from data drawn by Fermi-LAT and H.E.S.S.. The reason remains the same, being the interplay and compensation between the sharpness of the narrow boxes against the extension of the dimmer intermediate and wide boxes. We confront these results with the ones obtained by considering an updated performance as introduced in reference [209] depicted in all three panels as a dotted line. These limits are an improvement on the former by a factor of $\simeq 8$ (5.6) at low masses for narrow (wide) boxes and up to a maximum of $\simeq 1.6$ above 4 TeV for all box sizes. We leave the discussion on the solid black lines, related to the models, for the following section.

We now proceed to verify the robustness of these results. We start by analysing the effect of the specific choice of the window, depicted in figure 7.6. At first glance, the effect of varying the width of the sliding window has sizeable repercussions and is crucial to benefit most by the available gamma-ray data. Smaller windows fail to capture a significant part of the intermediate and wide boxes, softening the contribution from the dark matter signal. Although this is less evident for the narrow boxes, the energy resolution smears the signal to a wider shape leading

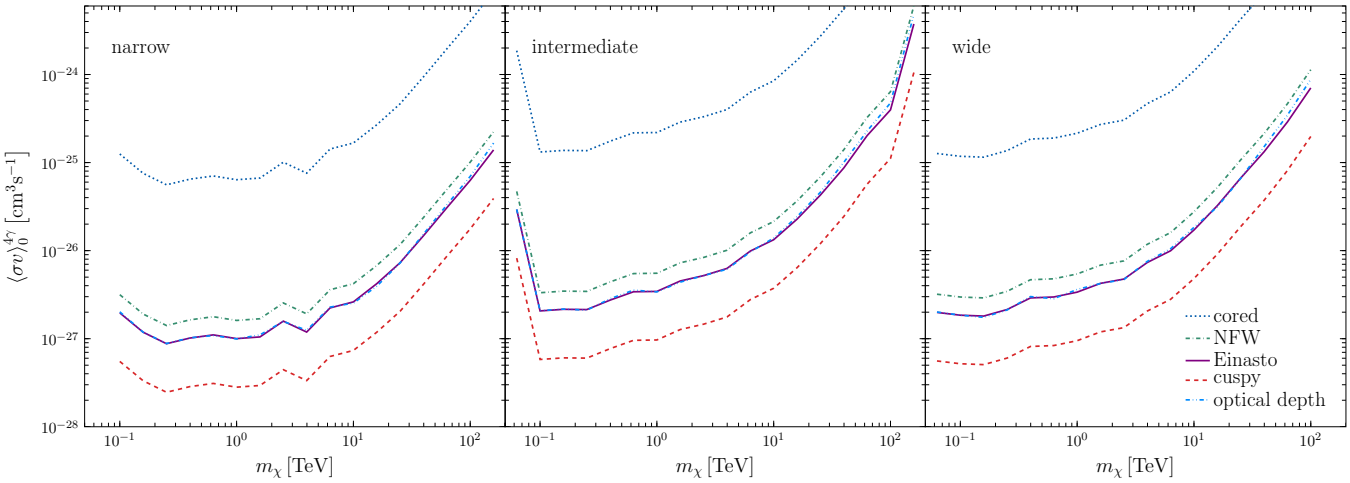

Figure 7.7.: Effects of the variation of the assumed dark matter density distribution profile on the upper limits from the profile likelihood analysis. The panels, read from left to right, correspond to narrow, intermediate, and wide boxes. Each panel shows the results for the different profiles as explained in the legend. Further details mimic the ones adopted in figure 7.5 for the CTA performance from [208].

to a similar effect as in the former cases. From these results, we see that a wise choice of the window can improve the limits as much as a factor 25. Furthermore, limits can improve up to a factor $1.5 - 2$ by positioning the window centre at a different energy $\bar{E}$.

The importance of the density distribution profile has already been addressed. In figure 7.7 we show the average limits obtained with the same method for different dark matter profiles. Starting from the benchmark profile (Einasto), the upper limits improve by a factor $\simeq 4$ if we consider the generalised cuspy profile with slope $\gamma = 1.2$ defined in table 3.1. On the contrary, considering the generalised cored profile, defined in the same table, weakens the results by almost two orders of magnitude. We also display the effect of the gamma-ray optical depth, which translates into an energy-dependent J-factor (c.f. equation (4.13). The impact of this consideration is a weakening of the 95%C.L. upper limits by around 20%.

We close this section with a brief discussion on the impact of the variation of other, less significant, assumptions. The calculations were repeated for other binnings ($N_b = 100$ and $N_b = 50$), where we found no significant deviation from the baseline results. As our results on the 95%C.L. upper limits on the annihilation cross section were derived under a background-only hypothesis, we expect the constraints to scale as $1/\sqrt{\Delta t}$. Indeed, with an additional run with an observation time of $\Delta t = 50\,\mathrm{h}$, this behaviour was verified within the expected margins. The effect of systematic uncertainties was also studied following the method described in [265, 268]. Bearing in mind that these estimates are still subject to change—depending on the final design of CTA—, we found that at low masses, where the uncertainties are dominated by systematics, the impact on the results are sizeable, whereas at high masses practically negligible. Furthermore, the prospects can be improved by a more complex analysis e.g., an optimised morphological analysis [265, 268, 269].

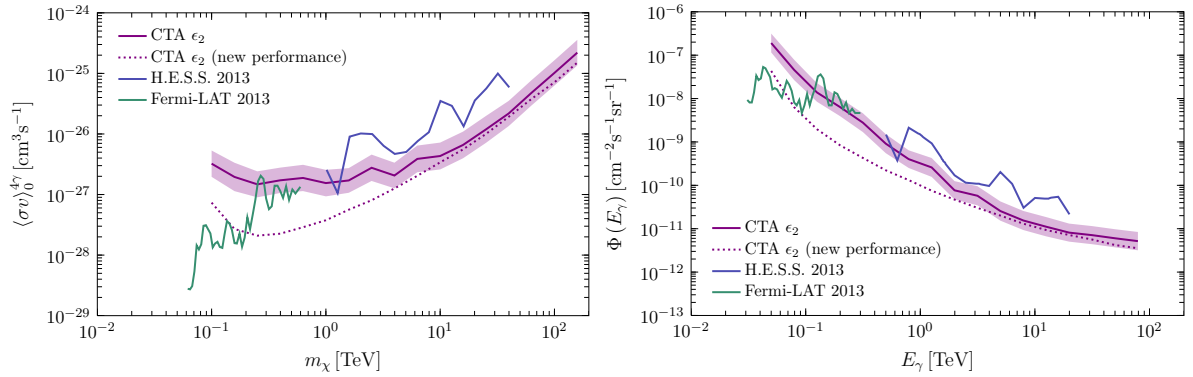

Figure 7.8.: Comparison of the expected 95% CL upper limits from CTA for narrow boxes with current Fermi-LAT [254] and H.E.S.S. [191] line searches, rescaled to be compared with narrow boxes. Left: upper limits on the cross section into four photons. Right: displays the flux upper limits for a monochromatic signal generated at a given energy. The colour and line coding is adopted from figure 7.5, the violet solid lines and bands correspond to the average upper limits obtained with the CTA performance of Ref. [208], while the dotted lines are for the updated performance [209].

Comparison with existing telescopes

It is an illustrative exercise to compare the prospects from CTA to the limits obtained by Fermi-LAT and H.E.S.S.. We consider the results on gamma-ray lines from references [191,254], properly scaled for narrow boxes, with the results of our analysis on CTA in figure 7.8. On the left panel, we show the 95%C.L. upper limits on the dark matter annihilation cross section, and on the right panel on the integrated gamma-ray flux. Since H.E.S.S. is also an IACT and shares a similar energy range, we performed a new calculation on the upper limits adopting the same set-ups of that analysis: An observation time of $\Delta t = 112\,\mathrm{h}$, an Einasto dark matter profile and the CGH field of view (c.f. section 7.2). We recall the corresponding J-factor $\overline{J}_{\mathrm{ann}} = 7.78 \times 10^{24}\,\mathrm{GeV^2\,cm^{-5}}$. The limits derived by the Fermi collaboration were calculated based on $\Delta t = 3.7\,\mathrm{yr}$ of observation on the R3 region assuming an NFW contracted profile, and a J-factor $J_{\mathrm{ann}} = 1.39 \times 10^{23}\,\mathrm{GeV^2\,sr\,cm^{-5}}$. The prospects on CTA for the 95%C.L. upper limits for both performances are presented figure 7.5. For this comparison, a new set of limits for CTA was derived assuming the same observation time, profile, region of interest and J-factor the observation time and region from H.E.S.S.. Our results suggests that at GeV energies, the limits derived by CTA will not be able to compete with those derived using Fermi-LAT data. However, at TeV energies CTA may supersede the H.E.S.S. performance, being able to constrain values for the cross section up to an order of magnitude smaller. We close this paragraph by stating that CTA shows a promising future for the search of gamma-ray boxes and triangles. No existing instrument is able to encompass such a huge span of energy values. Furthermore, the performance of the final design could present major improvements on the analysis.

Limits on models A and B

In this last section, we address the physical models capable of producing dark matter boxes. In chapter 6 we introduced some independent physical models that are able of producing gamma-

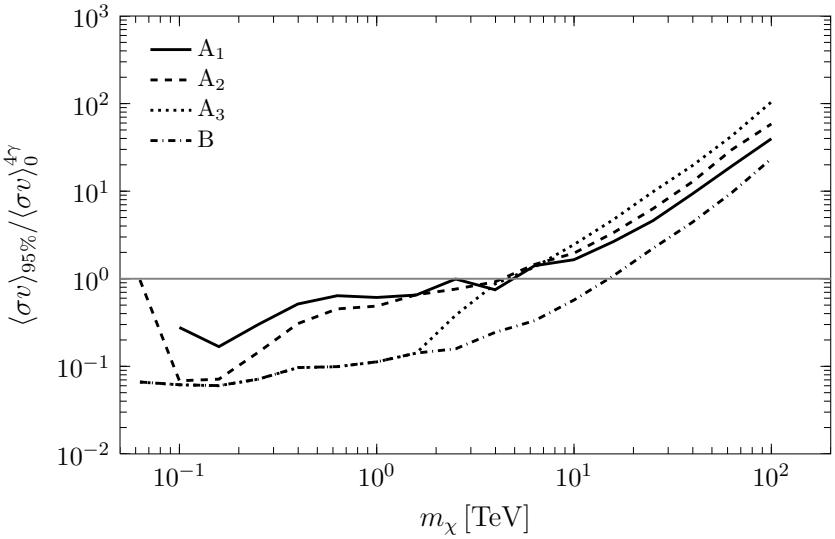

Figure 7.9.: The ration between average 95% CL upper limit expected for CTA and the target cross section of a thermal dark matter candidate in models $A_1, 2, 3$ and B against the dark matter mass. Further details mimic the ones adopted in figure 7.5 for the CTA performance from [208].

ray boxes and triangles. We discuss models A and B, since the constraints were derived for cases where the steepness and one of the two mass-splitting parameters were fixed, $\alpha = 0$ and $\delta_{X\eta} = \delta_{\gamma\phi} = 1$. Furthermore, we refer to both models B1 and B2 simultaneously as B, since for our purposes they are equivalent and we consider only the wide benchmark, due to the limits on the mass of the intermediate state. On the contrary, we analyse three benchmark scenarios for model A, namely for narrow, intermediate, and wide boxes, for the parameters $\delta_{\phi\chi} = 0.002, 0.19, 0.99$, labeled A_1, A_2, and A_3, respectively. In these two models, dark matter is interpreted as a WIMP, this means that the cross section at thermal freeze-out is fixed. However, we need to adjust it to the temperature of the present-day universe. For model A we use the ratios $\langle\sigma v_{\rm rel}\rangle_0/\langle\sigma v_{\rm rel}\rangle_{\rm f.o.}$ from equation (6.21), and for model B we have this ratio equal to unity. In both cases, the cascade process is described by $\chi\overline{\chi} \to as$ followed by $a \to \gamma\gamma$. We also take into account the branching fraction $\mathrm{BR}(a \to \gamma\gamma)$ and the boost factor present for model B, $B_S \simeq 10^3$. Then, considering the nature of these models, the target cross sections for experiments is calculated by

$$\langle\sigma v_{\rm rel}\rangle_0^{4\gamma} = B_S \, \frac{\langle\sigma v_{\rm rel}\rangle_0}{2} \, \mathrm{BR}(a \to \gamma\gamma) \; . \tag{7.23}$$

These values are depicted as solid black lines in figure 7.5 for the four benchmarks (A_1, A_2, A_3, and B). The step-wise behaviour of models $A_{1,2,3}$ is due to the decreasing branching fraction into photons of the pseudo scalar $\mathrm{BR}(a \to \gamma\gamma)$ due to the decay mode $a \to W^+W^-$, which opens at masses $m_a \gtrsim 2m_W$. In all cases, it is possible to exclude a large fraction of the parameter space. For the A_1 and A_2 scenarios, dark matter masses below 10 TeV are excluded, whereas for models A_3 and B it is possible to surpass this value up to a few times 10 TeV. We provide an alternative illustration for this results in figure 7.9. Here, we simply present the ratio of the 95%C.L. upper limits to the target annihilation cross section expected from thermal relics as realised in the concrete scenarios $A_{1,2,3}$ and B.

Part III.

Outlook and reach

8. Conclusion

In the first part, we reviewed the most important evidences which that point to the existence of dark matter. Not only is this compelling evidence present at different scales, but the simplicity of the concept of dark matter, addressing successfully the issues raised, is remarkable . Still, no details on the particle nature of dark matter have been unambiguously determined, which motivates further experimental efforts in their pursuit. We presented different detection methods and focussed on dark matter indirect detection, a search strategy that relies on the production of SM particles from annihilating or decaying dark matter. We also argued in favour of using gamma-rays as messengers for the possible observation of a positive signal.

In the second part of this work, we presented two new kinds of gamma-ray spectral features, which rise as a natural results of dark matter 1-step cascade processes. In the case of the intermediate state being a scalar or a Majorana fermion, gamma-ray boxes are produced; extended features of varying width and positioning which depend on the mass ratios of the involved particles. Gamma-ray triangles arise in the case of Dirac fermion intermediate states, and are have an extra phenomenological parameter which dictates the steepness of the signal. This property of the signal depends on the exact details of the particle physics model under consideration and the helicity of the intermediate state. However, for this signal not to be compensated by mirrored emissions of the same process, an underlying asymmetry in the dark sector is required. These two signatures are described by a set of three parameters, the dark matter mass, and the strength of the signal, allowing for a rich phenomenology. Moreover, they display, in all possible scenarios, a sharp cut-off, strikingly different from all known sources of background. A possible detection of such signals could be considered as a clean evidence of dark matter. Furthermore, in the case of the detection of a gamma-ray triangle this would additionally point towards a scenario where dark matter is also subject to an asymmetry, as ordinary matter is. As we showed, it is possible to construct a model that displays either a gamma-ray box or a triangle. These models can be successfully tested using current data drawn from gamma-ray telescopes such as Fermi-LAT and H.E.S.S., allowing for the derivation of strong upper limits. Furthermore, the annihilation cross section in WIMP scenarios can be tested below the thermal target using gamma-ray boxes, provided they are able to produce such a signature. Finally, we studied the prospects of the sensitivity of CTA towards gamma-ray boxes. Although CTA presents a major improvement extending the possibility of box and triangle searches to a larger energy regime, the sensitivity analysed in this work is not significantly better than the one provided by existing experiments. However, we remark that CTA is still prone to modifications in design and analysis algorithms enhancing the performance CTA will provide.

By introducing gamma-ray boxes and triangles we opened new possibilities of studies of dark matter. Although we performed detailed analyses using existing and simulated gamma-ray data, there are still other investigation strategies to be exploited. We hope that future studies address different facets of this particular class of dark matter scenarios.

Acknowledgements

Mi sincero e infinito agradecimiento a mi supervisor de tesis Alejandro Ibarra, por ayudarme y guiarme, por sus consejos y por su gran amistad. Este camino habría sido infinitamente más difícil de recorrer sin su apoyo. It is not obvious to find such an inspiring and patient colleague as Miguel Pato. I am a thousand times in debt with you for your help, guidance, friendship, advice, and honesty. For that and many other things, a thousand and one times thank you. My good friend, office mate, chauffeur, secretary, bank, etc. Sebastian Wild, for the laughter, distraction, help, and unconditional friendship, thank you. The past five years would have been extremely dull without letting me throw paper balls at you.

A mis grandes amistades, las viejas y las nuevas, que me sacan o meten en quilombos y despioles en los momentos más adecuados: gracias por ser siempre la fuerza que aleja a la soledad. No puedo olvidar a mi segunda familia, la familia Adler Yañez, quienes siempre me dieron un lugar en sus círculos más íntimos y proporcionaron el cariño y el afecto que tanto he apreciado, quedo siempre suyo. *familia*

excellence cluster

Bibliography

[1] J. C. Kapteyn, *First Attempt at a Theory of the Arrangement and Motion of the Sidereal System*, *Astrophys. J.* **55** (1922) 302–328.

[2] J. H. Jeans, *The motions of stars in a Kapteyn universe*, *Monthly Notices of the Royal Astronomical Society* **82** (Jan., 1922) 122–132.

[3] J. H. Oort, *The force exerted by the stellar system in the direction perpendicular to the galactic plane and some related problems*, *Bulletin of the Astronomical Institutes of the Netherlands* **6** (Aug., 1932) 249.

[4] F. Zwicky, *Die Rotverschiebung von extragalaktischen Nebeln*, *Helv. Phys. Acta* **6** (1933) 110–127.

[5] V. C. Rubin and W. K. Ford, Jr., *Rotation of the Andromeda Nebula from a Spectroscopic Survey of Emission Regions*, *Astrophys. J.* **159** (1970) 379–403.

[6] D. Clowe, M. Bradac, A. H. Gonzalez, M. Markevitch, S. W. Randall, C. Jones, and D. Zaritsky, *A direct empirical proof of the existence of dark matter*, *Astrophys. J.* **648** (2006) L109–L113, [astro-ph/0608407].

[7] A. Ibarra, H. M. Lee, S. López Gehler, W.-I. Park, and M. Pato, *Gamma-ray boxes from axion-mediated dark matter*, *JCAP* **1305** (2013) 016, [arXiv:1303.6632]. [Erratum: JCAP1603,no.03,E01(2016)].

[8] A. Ibarra, A. S. Lamperstorfer, S. López-Gehler, M. Pato, and G. Bertone, *On the sensitivity of CTA to gamma-ray boxes from multi-TeV dark matter*, *JCAP* **1509** (2015), no. 09 048, [arXiv:1503.06797].

[9] A. Ibarra, S. Lopez-Gehler, E. Molinaro, and M. Pato, *Gamma-ray triangles: a possible signature of asymmetric dark matter in indirect searches*, arXiv:1604.01899.

[10] T. P. Cheng and L. F. Li, *Gauge Theory Of Elementary Particle Physics*. 1984.

[11] M. E. Peskin and D. V. Schroeder, *An Introduction to quantum field theory*. 1995.

[12] S. P. Martin, *A Supersymmetry primer*, hep-ph/9709356. [Adv. Ser. Direct. High Energy Phys.18,1(1998)].

[13] **Super-Kamiokande**, Y. Fukuda *et. al.*, *Evidence for oscillation of atmospheric neutrinos*, *Phys. Rev. Lett.* **81** (1998) 1562–1567, [hep-ex/9807003].

[14] **SNO**, Q. R. Ahmad *et. al.*, *Measurement of the rate of $\nu_e + d \to p + p + e^-$ interactions produced by ^8B solar neutrinos at the Sudbury Neutrino Observatory*, *Phys. Rev. Lett.* **87** (2001) 071301, [nucl-ex/0106015].

[15] **SNO**, Q. R. Ahmad *et. al.*, *Direct evidence for neutrino flavor transformation from neutral current interactions in the Sudbury Neutrino Observatory*, *Phys. Rev. Lett.* **89** (2002) 011301, [nucl-ex/0204008].

[16] E. W. Kolb and M. S. Turner, *The Early Universe*, *Front. Phys.* **69** (1990) 1–547.

[17] **Planck**, P. A. R. Ade *et. al.*, *Planck 2015 results. XIII. Cosmological parameters*, arXiv:1502.01589.

[18] G. Bertone, D. Hooper, and J. Silk, *Particle dark matter: Evidence, candidates and constraints*, *Phys. Rept.* **405** (2005) 279–390, [hep-ph/0404175].

[19] T. S. van Albada, J. N. Bahcall, K. Begeman, and R. Sancisi, *The Distribution of Dark Matter in the Spiral Galaxy NGC-3198*, *Astrophys. J.* **295** (1985) 305–313.

[20] F. Iocco, M. Pato, and G. Bertone, *Evidence for dark matter in the inner Milky Way*, *Nature Phys.* **11** (2015) 245–248, [arXiv:1502.03821].

[21] M. Milgrom, *A Modification of the Newtonian dynamics as a possible alternative to the hidden mass hypothesis*, *Astrophys. J.* **270** (1983) 365–370.

[22] **MACHO**, C. Alcock *et. al.*, *The MACHO project: Microlensing results from 5.7 years of LMC observations*, *Astrophys. J.* **542** (2000) 281–307, [astro-ph/0001272].

[23] A. N. Taylor, S. Dye, T. J. Broadhurst, N. Benitez, and E. van Kampen, *Gravitational lens magnification and the mass of abell 1689*, *Astrophys. J.* **501** (1998) 539, [astro-ph/9801158].

[24] **Planck**, R. Adam *et. al.*, *Planck 2015 results. I. Overview of products and scientific results*, arXiv:1502.01582.

[25] **Particle Data Group**, K. A. Olive *et. al.*, *Review of Particle Physics*, *Chin. Phys.* **C38** (2014) 090001.

[26] **Supernova Cosmology Project**, S. Perlmutter *et. al.*, *Measurements of Omega and Lambda from 42 high redshift supernovae*, *Astrophys. J.* **517** (1999) 565–586, [astro-ph/9812133].

[27] **Supernova Cosmology Project**, S. Perlmutter *et. al.*, *Cosmology from Type Ia supernovae*, *Bull. Am. Astron. Soc.* **29** (1997) 1351, [astro-ph/9812473].

[28] **Supernova Search Team**, A. G. Riess *et. al.*, *Observational evidence from supernovae for an accelerating universe and a cosmological constant*, *Astron. J.* **116** (1998) 1009–1038, [astro-ph/9805201].

[29] **SDSS**, D. J. Eisenstein *et. al.*, *Detection of the baryon acoustic peak in the large-scale correlation function of SDSS luminous red galaxies*, *Astrophys. J.* **633** (2005) 560–574, [astro-ph/0501171].

[30] **SDSS**, K. N. Abazajian *et. al.*, *The Seventh Data Release of the Sloan Digital Sky Survey*, *Astrophys. J. Suppl.* **182** (2009) 543–558, [arXiv:0812.0649].

[31] C. S. Frenk and S. D. M. White, *Dark matter and cosmic structure*, *Annalen Phys.* **524** (2012) 507–534, [arXiv:1210.0544].

[32] S. Dodelson, *The Real Problem with MOND*, *Int. J. Mod. Phys.* **D20** (2011) 2749–2753, [arXiv:1112.1320].

[33] G. Gelmini and P. Gondolo, *DM Production Mechanisms*, arXiv:1009.3690.

[34] K. M. Zurek, *Asymmetric Dark Matter: Theories, Signatures, and Constraints*, *Phys. Rept.* **537** (2014) 91–121, [arXiv:1308.0338].

[35] K. Petraki and R. R. Volkas, *Review of asymmetric dark matter*, *Int. J. Mod. Phys.* **A28** (2013) 1330028, [arXiv:1305.4939].

[36] A. D. Sakharov, *Violation of CP Invariance, c Asymmetry, and Baryon Asymmetry of the Universe*, *Pisma Zh. Eksp. Teor. Fiz.* **5** (1967) 32–35. [Usp. Fiz. Nauk161,61(1991)].

[37] M. Blennow, B. Dasgupta, E. Fernandez-Martinez, and N. Rius, *Aidnogenesis via Leptogenesis and Dark Sphalerons*, *JHEP* **03** (2011) 014, [arXiv:1009.3159].

[38] D. Hooper, J. March-Russell, and S. M. West, *Asymmetric sneutrino dark matter and the Omega(b) / Omega(DM) puzzle*, *Phys. Lett.* **B605** (2005) 228–236, [hep-ph/0410114].

[39] D. E. Kaplan, M. A. Luty, and K. M. Zurek, *Asymmetric Dark Matter*, *Phys. Rev.* **D79** (2009) 115016, [arXiv:0901.4117].

[40] N. Cosme, L. Lopez Honorez, and M. H. G. Tytgat, *Leptogenesis and dark matter related?*, *Phys. Rev.* **D72** (2005) 043505, [hep-ph/0506320].

[41] E. J. Chun, *Minimal Dark Matter and Leptogenesis*, *JHEP* **03** (2011) 098, [arXiv:1102.3455].

[42] C. Arina, R. N. Mohapatra, and N. Sahu, *Co-genesis of Matter and Dark Matter with Vector-like Fourth Generation Leptons*, *Phys. Lett.* **B720** (2013) 130–136, [arXiv:1211.0435].

[43] H. An, S.-L. Chen, R. N. Mohapatra, and Y. Zhang, *Leptogenesis as a Common Origin for Matter and Dark Matter*, *JHEP* **03** (2010) 124, [arXiv:0911.4463].

[44] M. Fukugita and T. Yanagida, *Baryogenesis Without Grand Unification*, *Phys. Lett.* **B174** (1986) 45–47.

[45] I. Affleck and M. Dine, *A New Mechanism for Baryogenesis*, *Nucl. Phys.* **B249** (1985) 361–380.

[46] M. Dine, L. Randall, and S. D. Thomas, *Baryogenesis from flat directions of the supersymmetric standard model*, *Nucl. Phys.* **B458** (1996) 291–326, [hep-ph/9507453].

[47] C. Cheung and K. M. Zurek, *Affleck-Dine Cogenesis*, *Phys. Rev.* **D84** (2011) 035007, [arXiv:1105.4612].

[48] C. Cheung and Y. Zhang, *Electroweak Cogenesis*, *JHEP* **09** (2013) 002, [arXiv:1306.4321].

[49] G. R. Farrar and G. Zaharijas, *Dark matter and the baryon asymmetry*, *Phys. Rev. Lett.* **96** (2006) 041302, [hep-ph/0510079].

[50] N. Haba and S. Matsumoto, *Baryogenesis from Dark Sector*, *Prog. Theor. Phys.* **125** (2011) 1311–1316, [arXiv:1008.2487].

[51] J. Shelton and K. M. Zurek, *Darkogenesis: A baryon asymmetry from the dark matter sector*, *Phys. Rev.* **D82** (2010) 123512, [arXiv:1008.1997].

[52] A. G. Cohen and D. B. Kaplan, *SPONTANEOUS BARYOGENESIS*, *Nucl. Phys.* **B308** (1988) 913–928.

[53] A. G. Cohen, D. B. Kaplan, and A. E. Nelson, *Spontaneous baryogenesis at the weak phase transition*, *Phys. Lett.* **B263** (1991) 86–92.

[54] A. G. Cohen, D. B. Kaplan, and A. E. Nelson, *Diffusion enhances spontaneous electroweak baryogenesis*, *Phys. Lett.* **B336** (1994) 41–47, [hep-ph/9406345].

[55] J. March-Russell and M. McCullough, *Asymmetric Dark Matter via Spontaneous Co-Genesis*, *JCAP* **1203** (2012) 019, [arXiv:1106.4319].

[56] K. Kamada and M. Yamaguchi, *Asymmetric Dark Matter from Spontaneous Cogenesis in the Supersymmetric Standard Model*, *Phys. Rev.* **D85** (2012) 103530, [arXiv:1201.2636].

[57] T. Banks, S. Echols, and J. L. Jones, *Baryogenesis, dark matter and the Pentagon*, *JHEP* **11** (2006) 046, [hep-ph/0608104].

[58] Y. Mambrini, Talk at the "IBS-MultiDark Joint Workshop on Dark Matter", 2015. http://www.ymambrini.com/My_World/Conference_files/Madrid.pdf".

[59] J. Silk *et. al.*, *Particle Dark Matter: Observations, Models and Searches*. 2010.

[60] P. Sikivie, *Axions*, in *In *Bertone, G. (ed.): Particle dark matter* 204-227*, 2010.

[61] M. Shaposhnikov, *Sterile neutrinos*, in *In *Bertone, G. (ed.): Particle dark matter* 228-248*, 2010.

[62] G. Servant, *Dark matter at the electroweak scale: Non-supersymmetric candidates*, in *In *Bertone, G. (ed.): Particle dark matter* 164-189*, 2010.

[63] J. Ellis and K. A. Olive, *Supersymmetric Dark Matter Candidates*, arXiv:1001.3651.

[64] M. Cirelli, *Status of Indirect (and Direct) Dark Matter searches*, arXiv:1511.02031.

[65] M. Cirelli, G. Corcella, A. Hektor, G. Hutsi, M. Kadastik, P. Panci, M. Raidal, F. Sala, and A. Strumia, *PPPC 4 DM ID: A Poor Particle Physicist Cookbook for Dark Matter Indirect Detection*, *JCAP* **1103** (2011) 051, [arXiv:1012.4515]. [Erratum: JCAP1210,E01(2012)].

[66] J. F. Navarro, C. S. Frenk, and S. D. M. White, *The Structure of cold dark matter halos*, *Astrophys. J.* **462** (1996) 563–575, [astro-ph/9508025].

[67] J. F. Navarro, C. S. Frenk, and S. D. M. White, *A Universal density profile from hierarchical clustering*, *Astrophys. J.* **490** (1997) 493–508, [astro-ph/9611107].

[68] A. W. Graham, D. Merritt, B. Moore, J. Diemand, and B. Terzic, *Empirical models for Dark Matter Halos. I. Nonparametric Construction of Density Profiles and Comparison with Parametric Models*, *Astron. J.* **132** (2006) 2685–2700, [astro-ph/0509417].

[69] J. F. Navarro, A. Ludlow, V. Springel, J. Wang, M. Vogelsberger, S. D. M. White, A. Jenkins, C. S. Frenk, and A. Helmi, *The Diversity and Similarity of Cold Dark Matter Halos*, *Mon. Not. Roy. Astron. Soc.* **402** (2010) 21, [arXiv:0810.1522].

[70] J. Diemand, B. Moore, and J. Stadel, *Convergence and scatter of cluster density profiles*, *Mon. Not. Roy. Astron. Soc.* **353** (2004) 624, [astro-ph/0402267].

[71] L. Hernquist, *An Analytical Model for Spherical Galaxies and Bulges*, *Astrophys. J.* **356** (1990) 359.

[72] J. N. Bahcall and R. M. Soneira, *The Universe at faint magnetidues. 2. Models for the predicted star counts*, *Astrophys. J. Suppl.* **44** (1980) 73–110.

[73] K. G. Begeman, A. H. Broeils, and R. H. Sanders, *Extended rotation curves of spiral galaxies: Dark haloes and modified dynamics*, *Mon. Not. Roy. Astron. Soc.* **249** (1991) 523.

[74] P. Mollitor, E. Nezri, and R. Teyssier, *Baryonic and dark matter distribution in cosmological simulations of spiral galaxies*, *Mon. Not. Roy. Astron. Soc.* **447** (2015), no. 2 1353–1369, [arXiv:1405.4318].

[75] R. Catena and P. Ullio, *A novel determination of the local dark matter density*, *JCAP* **1008** (2010) 004, [arXiv:0907.0018].

[76] P. Salucci, F. Nesti, G. Gentile, and C. F. Martins, *The dark matter density at the Sun's location*, *Astron. Astrophys.* **523** (2010) A83, [arXiv:1003.3101].

[77] S. Gillessen, F. Eisenhauer, S. Trippe, T. Alexander, R. Genzel, F. Martins, and T. Ott, *Monitoring stellar orbits around the Massive Black Hole in the Galactic Center*, *Astrophys. J.* **692** (2009) 1075–1109, [arXiv:0810.4674].

[78] K. Ando, T. Nagayama, T. Omodaka, T. Handa, H. Imai, A. Nakagawa, H. Nakanishi, M. Honma, H. Kobayashi, and T. Miyaji, *Astrometry of Galactic Star-Forming Region ON2N with VERA: Estimation of the Galactic Constants*, *Publ. Astron. Soc. Jap.* **63** (2011) 45, [arXiv:1012.5715].

[79] Z. Malkin, *The current best estimate of the Galactocentric distance of the Sun based on comparison of different statistical techniques*, arXiv:1202.6128.

[80] M. J. Reid *et. al.*, *Trigonometric Parallaxes of High Mass Star Forming Regions: the Structure and Kinematics of the Milky Way*, *Astrophys. J.* **783** (2014) 130, [arXiv:1401.5377].

[81] O. Y. Gnedin, A. V. Kravtsov, A. A. Klypin, and D. Nagai, *Response of dark matter halos to condensation of baryons: Cosmological simulations and improved adiabatic contraction model*, *Astrophys. J.* **616** (2004) 16–26, [astro-ph/0406247].

[82] F. Prada, A. Klypin, J. Flix Molina, M. Martinez, and E. Simonneau, *Dark Matter Annihilation in the Milky Way Galaxy: Effects of Baryonic Compression*, *Phys. Rev. Lett.* **93** (2004) 241301, [astro-ph/0401512].

[83] J. S. Bullock, T. S. Kolatt, Y. Sigad, R. S. Somerville, A. V. Kravtsov, A. A. Klypin, J. R. Primack, and A. Dekel, *Profiles of dark haloes. Evolution, scatter, and environment*, *Mon. Not. Roy. Astron. Soc.* **321** (2001) 559–575, [astro-ph/9908159].

[84] R. H. Wechsler, J. S. Bullock, J. R. Primack, A. V. Kravtsov, and A. Dekel, *Concentrations of dark halos from their assembly histories*, *Astrophys. J.* **568** (2002) 52–70, [astro-ph/0108151].

[85] A. V. Maccio', A. A. Dutton, and F. C. v. d. Bosch, *Concentration, Spin and Shape of Dark Matter Haloes as a Function of the Cosmological Model: WMAP1, WMAP3 and WMAP5 results*, *Mon. Not. Roy. Astron. Soc.* **391** (2008) 1940–1954, [arXiv:0805.1926].

[86] D. H. Zhao, Y. P. Jing, H. J. Mo, and G. Boerner, *Accurate universal models for the mass accretion histories and concentrations of dark matter halos*, *Astrophys. J.* **707** (2009) 354–369, [arXiv:0811.0828].

[87] A. D. Ludlow, J. F. Navarro, M. Boylan-Kolchin, P. E. Bett, R. E. Angulo, M. Li, S. D. M. White, C. Frenk, and V. Springel, *The Mass Profile and Accretion History of Cold Dark Matter Halos*, *Mon. Not. Roy. Astron. Soc.* **432** (2013) 1103, [arXiv:1302.0288].

[88] F. Prada, A. A. Klypin, A. J. Cuesta, J. E. Betancort-Rijo, and J. Primack, *Halo concentrations in the standard LCDM cosmology*, *Mon. Not. Roy. Astron. Soc.* **423** (2012) 3018–3030, [arXiv:1104.5130].

[89] M. A. Sánchez-Conde and F. Prada, *The flattening of the concentration–mass relation towards low halo masses and its implications for the annihilation signal boost*, *Mon. Not. Roy. Astron. Soc.* **442** (2014), no. 3 2271–2277, [arXiv:1312.1729].

[90] A. Moliné, M. A. Sánchez-Conde, S. Palomares-Ruiz, and F. Prada, *Characterization of subhalo structural properties and implications for dark matter annihilation signals*, arXiv:1603.04057.

[91] C. Evoli, D. Gaggero, D. Grasso, and L. Maccione, *Cosmic-Ray Nuclei, Antiprotons and Gamma-rays in the Galaxy: a New Diffusion Model*, *JCAP* **0810** (2008) 018, [arXiv:0807.4730]. [Erratum: JCAP1604,no.04,E01(2016)].

[92] A. E. Vladimirov, S. W. Digel, G. Johannesson, P. F. Michelson, I. V. Moskalenko, P. L. Nolan, E. Orlando, T. A. Porter, and A. W. Strong, *GALPROP WebRun: an internet-based service for calculating galactic cosmic ray propagation and associated photon emissions*, *Comput. Phys. Commun.* **182** (2011) 1156–1161, [arXiv:1008.3642].

[93] O. Adriani *et. al.*, *Measurement of the flux of primary cosmic ray antiprotons with energies of 60-MeV to 350-GeV in the PAMELA experiment*, *JETP Lett.* **96** (2013) 621–627. [Pisma Zh. Eksp. Teor. Fiz.96,693(2012)].

[94] A. Kounine, Talk at the "AMS Days at CERN", 2015. http://indico.cern.ch/event/381134. Accessed: 2016-04-08.

[95] N. Fornengo, L. Maccione, and A. Vittino, *Constraints on particle dark matter from cosmic-ray antiprotons*, *JCAP* **1404** (2014), no. 04 003, [arXiv:1312.3579].

[96] M. Cirelli, D. Gaggero, G. Giesen, M. Taoso, and A. Urbano, *Antiproton constraints on the GeV gamma-ray excess: a comprehensive analysis*, *JCAP* **1412** (2014), no. 12 045, [arXiv:1407.2173].

[97] H.-B. Jin, Y.-L. Wu, and Y.-F. Zhou, *Upper limits on dark matter annihilation cross sections from the first AMS-02 antiproton data*, *Phys. Rev.* **D92** (2015), no. 5 055027, [arXiv:1504.04604].

[98] G. Giesen, M. Boudaud, Y. Génolini, V. Poulin, M. Cirelli, P. Salati, and P. D. Serpico, *AMS-02 antiprotons, at last! Secondary astrophysical component and immediate implications for Dark Matter*, *JCAP* **1509** (2015), no. 09 023, [arXiv:1504.04276].

[99] **HEAT**, S. W. Barwick *et. al.*, *Measurements of the cosmic ray positron fraction from 1-GeV to 50-GeV*, *Astrophys. J.* **482** (1997) L191–L194, [astro-ph/9703192].

[100] **PAMELA**, O. Adriani *et. al.*, *PAMELA results on the cosmic-ray antiproton flux from 60 MeV to 180 GeV in kinetic energy*, *Phys. Rev. Lett.* **105** (2010) 121101, [arXiv:1007.0821].

[101] **PAMELA**, O. Adriani *et. al.*, *An anomalous positron abundance in cosmic rays with energies 1.5-100 GeV*, *Nature* **458** (2009) 607–609, [arXiv:0810.4995].

[102] **PAMELA**, O. Adriani *et. al.*, *Cosmic-Ray Positron Energy Spectrum Measured by PAMELA*, *Phys. Rev. Lett.* **111** (2013) 081102, [arXiv:1308.0133].

[103] **AMS**, M. Aguilar *et. al.*, *First Result from the Alpha Magnetic Spectrometer on the International Space Station: Precision Measurement of the Positron Fraction in Primary Cosmic Rays of 0.5–350 GeV*, *Phys. Rev. Lett.* **110** (2013) 141102.

[104] **AMS**, L. Accardo *et. al.*, *High Statistics Measurement of the Positron Fraction in Primary Cosmic Rays of 0.5–500 GeV with the Alpha Magnetic Spectrometer on the International Space Station*, *Phys. Rev. Lett.* **113** (2014) 121101.

[105] **AMS**, M. Aguilar *et. al.*, *Electron and Positron Fluxes in Primary Cosmic Rays Measured with the Alpha Magnetic Spectrometer on the International Space Station*, *Phys. Rev. Lett.* **113** (2014) 121102.

[106] **Fermi-LAT**, M. Ackermann *et. al.*, *Measurement of separate cosmic-ray electron and positron spectra with the Fermi Large Area Telescope*, *Phys. Rev. Lett.* **108** (2012) 011103, [arXiv:1109.0521].

[107] I. Cholis and D. Hooper, *Dark Matter and Pulsar Origins of the Rising Cosmic Ray Positron Fraction in Light of New Data From AMS*, *Phys. Rev.* **D88** (2013) 023013, [arXiv:1304.1840].

[108] P. Mertsch and S. Sarkar, *Testing astrophysical models for the PAMELA positron excess with cosmic ray nuclei*, *Phys. Rev. Lett.* **103** (2009) 081104, [arXiv:0905.3152].

[109] M. Ahlers, P. Mertsch, and S. Sarkar, *On cosmic ray acceleration in supernova remnants and the FERMI/PAMELA data*, *Phys. Rev.* **D80** (2009) 123017, [arXiv:0909.4060].

[110] I. Cholis and D. Hooper, *Constraining the origin of the rising cosmic ray positron fraction with the boron-to-carbon ratio*, *Phys. Rev.* **D89** (2014), no. 4 043013, [arXiv:1312.2952].

[111] D. Hooper, P. Blasi, and P. D. Serpico, *Pulsars as the Sources of High Energy Cosmic Ray Positrons*, *JCAP* **0901** (2009) 025, [arXiv:0810.1527].

[112] L. Bergstrom, T. Bringmann, I. Cholis, D. Hooper, and C. Weniger, *New limits on dark matter annihilation from AMS cosmic ray positron data*, *Phys. Rev. Lett.* **111** (2013) 171101, [arXiv:1306.3983].

[113] A. Ibarra, A. S. Lamperstorfer, and J. Silk, *Dark matter annihilations and decays after the AMS-02 positron measurements*, *Phys. Rev.* **D89** (2014), no. 6 063539, [arXiv:1309.2570].

[114] N. Fornengo, R. A. Lineros, M. Regis, and M. Taoso, *Galactic synchrotron emission from WIMPs at radio frequencies*, *JCAP* **1201** (2012) 005, [arXiv:1110.4337].

[115] N. Fornengo, R. Lineros, M. Regis, and M. Taoso, *Cosmological Radio Emission induced by WIMP Dark Matter*, *JCAP* **1203** (2012) 033, [arXiv:1112.4517].

[116] M. Cirelli and M. Taoso, *Updated galactic radio constraints on Dark Matter*, arXiv:1604.06267.

[117] J. Buch, M. Cirelli, G. Giesen, and M. Taoso, *PPPC 4 DM secondary: A Poor Particle Physicist Cookbook for secondary radiation from Dark Matter*, *JCAP* **1509** (2015), no. 09 037, [arXiv:1505.01049].

[118] N. Fornengo, R. A. Lineros, M. Regis, and M. Taoso, *The isotropic radio background revisited*, *JCAP* **1404** (2014) 008, [arXiv:1402.2218].

[119] https://www.skatelescope.org/.

[120] http://www.lofar.org/.

[121] **IceCube**, M. G. Aartsen *et. al.*, *All-flavour Search for Neutrinos from Dark Matter Annihilations in the Milky Way with IceCube/DeepCore*, arXiv:1606.00209.

[122] **IceCube**, J. Ahrens *et. al.*, *Icecube - the next generation neutrino telescope at the south pole*, *Nucl. Phys. Proc. Suppl.* **118** (2003) 388–395, [astro-ph/0209556]. [,388(2002)].

[123] **Super-Kamiokande**, Y. Fukuda *et. al.*, *The Super-Kamiokande detector*, *Nucl. Instrum. Meth.* **A501** (2003) 418–462.

[124] **IceCube**, M. G. Aartsen *et. al.*, *Improved limits on dark matter annihilation in the Sun with the 79-string IceCube detector and implications for supersymmetry*, *JCAP* **1604** (2016), no. 04 022, [arXiv:1601.00653].

[125] **IceCube**, M. G. Aartsen *et. al.*, *Multipole analysis of IceCube data to search for dark matter accumulated in the Galactic halo*, *Eur. Phys. J.* **C75** (2015), no. 99 20, [arXiv:1406.6868].

[126] **IceCube**, M. G. Aartsen *et. al.*, *Search for Dark Matter Annihilation in the Galactic Center with IceCube-79*, *Eur. Phys. J.* **C75** (2015), no. 10 492, [arXiv:1505.07259].

[127] **Super-Kamiokande**, K. Choi *et. al.*, *Search for neutrinos from annihilation of captured low-mass dark matter particles in the Sun by Super-Kamiokande*, *Phys. Rev. Lett.* **114** (2015), no. 14 141301, [arXiv:1503.04858].

[128] R. Kappl and M. W. Winkler, *New Limits on Dark Matter from Super-Kamiokande*, *Nucl. Phys.* **B850** (2011) 505–521, [arXiv:1104.0679].

[129] **Super-Kamiokande**, S. Desai *et. al.*, *Search for dark matter WIMPs using upward through-going muons in Super-Kamiokande*, *Phys. Rev.* **D70** (2004) 083523, [hep-ex/0404025]. [Erratum: Phys. Rev.D70,109901(2004)].

[130] M. W. Goodman and E. Witten, *Detectability of Certain Dark Matter Candidates*, *Phys. Rev.* **D31** (1985) 3059.

[131] D. G. Cerdeno and A. M. Green, *Direct detection of WIMPs*, arXiv:1002.1912.

[132] J. D. Lewin and P. F. Smith, *Review of mathematics, numerical factors, and corrections for dark matter experiments based on elastic nuclear recoil*, *Astropart. Phys.* **6** (1996) 87–112.

[133] G. Jungman, M. Kamionkowski, and K. Griest, *Supersymmetric dark matter*, *Phys. Rept.* **267** (1996) 195–373, [hep-ph/9506380].

[134] J. Bovy *et. al.*, *The Milky Way's circular velocity curve between 4 and 14 kpc from APOGEE data*, *Astrophys. J.* **759** (2012) 131, [arXiv:1209.0759].

[135] K. Freese, M. Lisanti, and C. Savage, *Colloquium: Annual modulation of dark matter*, *Rev. Mod. Phys.* **85** (2013) 1561–1581, [arXiv:1209.3339].

[136] P. J. Fox, J. Liu, and N. Weiner, *Integrating Out Astrophysical Uncertainties*, *Phys. Rev.* **D83** (2011) 103514, [arXiv:1011.1915].

[137] M. T. Frandsen, F. Kahlhoefer, C. McCabe, S. Sarkar, and K. Schmidt-Hoberg, *Resolving astrophysical uncertainties in dark matter direct detection*, *JCAP* **1201** (2012) 024, [arXiv:1111.0292].

[138] P. Gondolo and G. B. Gelmini, *Halo independent comparison of direct dark matter detection data*, *JCAP* **1212** (2012) 015, [arXiv:1202.6359].

[139] F. Ferrer, A. Ibarra, and S. Wild, *A novel approach to derive halo-independent limits on dark matter properties*, *JCAP* **1509** (2015), no. 09 052, [arXiv:1506.03386].

[140] R. Bernabei *et. al.*, *Final model independent result of DAMA/LIBRA-phase1*, *Eur. Phys. J.* **C73** (2013) 2648, [arXiv:1308.5109].

[141] S. C. Kim *et. al.*, *New Limits on Interactions between Weakly Interacting Massive Particles and Nucleons Obtained with CsI(Tl) Crystal Detectors*, *Phys. Rev. Lett.* **108** (2012) 181301, [arXiv:1204.2646].

[142] **XMASS**, K. Abe *et. al.*, *Direct dark matter search by annual modulation in XMASS-I*, *Phys. Lett.* **B759** (2016) 272–276, [arXiv:1511.04807].

[143] **DAMIC**, J. Barreto *et. al.*, *Direct Search for Low Mass Dark Matter Particles with CCDs*, *Phys. Lett.* **B711** (2012) 264–269, [arXiv:1105.5191].

[144] **CoGeNT**, C. E. Aalseth *et. al.*, *Search for An Annual Modulation in Three Years of CoGeNT Dark Matter Detector Data*, arXiv:1401.3295.

[145] **CRESST-II**, G. Angloher *et. al.*, *Results on low mass WIMPs using an upgraded CRESST-II detector*, *Eur. Phys. J.* **C74** (2014), no. 12 3184, [arXiv:1407.3146].

[146] **CRESST**, G. Angloher *et. al.*, *Results on light dark matter particles with a low-threshold CRESST-II detector*, *Eur. Phys. J.* **C76** (2016), no. 1 25, [arXiv:1509.01515].

[147] **XENON100**, E. Aprile *et. al.*, *Dark Matter Results from 225 Live Days of XENON100 Data*, *Phys. Rev. Lett.* **109** (2012) 181301, [arXiv:1207.5988].

[148] **XENON100**, E. Aprile *et. al.*, *Limits on spin-dependent WIMP-nucleon cross sections from 225 live days of XENON100 data*, *Phys. Rev. Lett.* **111** (2013), no. 2 021301, [arXiv:1301.6620].

[149] **XENON10**, J. Angle *et. al.*, *A search for light dark matter in XENON10 data*, *Phys. Rev. Lett.* **107** (2011) 051301, [arXiv:1104.3088]. [Erratum: Phys. Rev. Lett.110,249901(2013)].

[150] **LUX**, D. S. Akerib *et. al.*, *First results from the LUX dark matter experiment at the Sanford Underground Research Facility*, *Phys. Rev. Lett.* **112** (2014) 091303, [arXiv:1310.8214].

[151] **LUX**, D. S. Akerib *et. al.*, *Improved Limits on Scattering of Weakly Interacting Massive Particles from Reanalysis of 2013 LUX Data*, *Phys. Rev. Lett.* **116** (2016), no. 16 161301, [arXiv:1512.03506].

[152] **LUX**, D. S. Akerib *et. al.*, *Results on the Spin-Dependent Scattering of Weakly Interacting Massive Particles on Nucleons from the Run 3 Data of the LUX Experiment*, *Phys. Rev. Lett.* **116** (2016), no. 16 161302, [arXiv:1602.03489].

[153] **PandaX**, A. Tan *et. al.*, *Dark Matter Search Results from the Commissioning Run of PandaX-II*, arXiv:1602.06563.

[154] G. Angloher *et. al.*, *Results from 730 kg days of the CRESST-II Dark Matter Search*, *Eur. Phys. J.* **C72** (2012) 1971, [arXiv:1109.0702].

[155] **SuperCDMS**, R. Agnese *et. al.*, *Search for Low-Mass Weakly Interacting Massive Particles with SuperCDMS*, *Phys. Rev. Lett.* **112** (2014), no. 24 241302, [arXiv:1402.7137].

[156] **SuperCDMS**, R. Agnese *et. al.*, *New Results from the Search for Low-Mass Weakly Interacting Massive Particles with the CDMS Low Ionization Threshold Experiment*, *Phys. Rev. Lett.* **116** (2016), no. 7 071301, [arXiv:1509.02448].

[157] **EDELWEISS**, E. Armengaud *et. al.*, *A search for low-mass WIMPs with EDELWEISS-II heat-and-ionization detectors*, *Phys. Rev.* **D86** (2012) 051701, [arXiv:1207.1815].

[158] M. Felizardo *et. al.*, *Final Analysis and Results of the Phase II SIMPLE Dark Matter Search*, *Phys. Rev. Lett.* **108** (2012) 201302, [arXiv:1106.3014].

[159] **PICASSO**, S. Archambault *et. al.*, *Constraints on Low-Mass WIMP Interactions on ^{19}F from PICASSO*, *Phys. Lett.* **B711** (2012) 153–161, [arXiv:1202.1240].

[160] **PICO**, C. Amole *et. al.*, *Improved dark matter search results from PICO-2L Run 2*, *Phys. Rev.* **D93** (2016), no. 6 061101, [arXiv:1601.03729].

[161] **COUPP**, E. Behnke *et. al.*, *First Dark Matter Search Results from a 4-kg CF_3I Bubble Chamber Operated in a Deep Underground Site*, *Phys. Rev.* **D86** (2012), no. 5 052001, [arXiv:1204.3094]. [Erratum: Phys. Rev.D90,no.7,079902(2014)].

[162] **IceCube**, M. G. Aartsen *et. al.*, *Search for dark matter annihilations in the Sun with the 79-string IceCube detector*, *Phys. Rev. Lett.* **110** (2013), no. 13 131302, [arXiv:1212.4097].

[163] **CDMS**, R. Agnese *et. al.*, *Silicon Detector Dark Matter Results from the Final Exposure of CDMS II*, *Phys. Rev. Lett.* **111** (2013), no. 25 251301, [arXiv:1304.4279].

[164] C. E. Aalseth *et. al.*, *Maximum Likelihood Signal Extraction Method Applied to 3.4 years of CoGeNT Data*, arXiv:1401.6234.

[165] http://fermi.gsfc.nasa.gov/ssc/observations/types/allsky/. Accessed: 2016-06-25.

[166] R. Schlickeiser, *Cosmic ray astrophysics*. 2002.

[167] **Fermi-LAT**, A. A. Abdo *et. al.*, *The First Fermi Large Area Telescope Catalog of Gamma-ray Pulsars*, *Astrophys. J. Suppl.* **187** (2010) 460–494, [arXiv:0910.1608]. [Erratum: Astrophys. J. Suppl.193,22(2011)].

[168] **Fermi-LAT**, A. A. Abdo *et. al.*, *The Second Fermi Large Area Telescope Catalog of Gamma-ray Pulsars*, *Astrophys. J. Suppl.* **208** (2013) 17, [arXiv:1305.4385].

[169] M. S. Longair, ed., *High-energy astrophysics. Vol. 1: Particles, photons and their detection*. 1992.

[170] M. S. Longair, *High-energy astrophysics. Vol. 2: Stars, the galaxy and the interstellar medium*. 1994.

[171] G. R. Blumenthal and R. J. Gould, *Bremsstrahlung, synchrotron radiation, and compton scattering of high-energy electrons traversing dilute gases*, *Rev. Mod. Phys.* **42** (1970) 237–270.

[172] A. De Angelis, G. Galanti, and M. Roncadelli, *Transparency of the Universe to gamma rays*, *Mon. Not. Roy. Astron. Soc.* **432** (2013) 3245–3249, [arXiv:1302.6460].

[173] P. Madau and E. S. Phinney, *Constraints on the Extragalactic Background Light from Gamma-Ray Observations of High-Redshift Quasars*, *Astrophys.J.* **456** (Jan., 1996) 124.

[174] R. J. Gould and G. Schréder, *Opacity of the Universe to High-Energy Photons*, *Physical Review Letters* **16** (Feb., 1966) 252–254.

[175] R. J. Gould and G. P. Schréder, *Opacity of the Universe to High-Energy Photons*, *Physical Review* **155** (Mar., 1967) 1408–1411.

[176] J. V. Jelley, *High-Energy γ-Ray Absorption in Space by a 3.5*deg*K Microwave Field*, *Physical Review Letters* **16** (Mar., 1966) 479–481.

[177] T. Sjostrand, S. Mrenna, and P. Z. Skands, *A Brief Introduction to PYTHIA 8.1*, *Comput. Phys. Commun.* **178** (2008) 852–867, [arXiv:0710.3820].

[178] G. Corcella, I. G. Knowles, G. Marchesini, S. Moretti, K. Odagiri, P. Richardson, M. H. Seymour, and B. R. Webber, *HERWIG 6: An Event generator for hadron emission reactions with interfering gluons (including supersymmetric processes)*, *JHEP* **01** (2001) 010, [hep-ph/0011363].

[179] http://www.marcocirelli.net/PPPC4DMID.html.

[180] **Fermi-LAT**, M. Ackermann *et. al.*, *Updated search for spectral lines from Galactic dark matter interactions with pass 8 data from the Fermi Large Area Telescope*, *Phys. Rev.* **D91** (2015), no. 12 122002, [arXiv:1506.00013].

[181] **Fermi-LAT**, M. Ackermann *et. al.*, *Searching for Dark Matter Annihilation from Milky Way Dwarf Spheroidal Galaxies with Six Years of Fermi Large Area Telescope Data*, *Phys. Rev. Lett.* **115** (2015), no. 23 231301, [arXiv:1503.02641].

[182] F. Calore, I. Cholis, and C. Weniger, *Background model systematics for the Fermi GeV excess*, *JCAP* **1503** (2015) 038, [arXiv:1409.0042].

[183] T. Daylan, D. P. Finkbeiner, D. Hooper, T. Linden, S. K. N. Portillo, N. L. Rodd, and T. R. Slatyer, *The characterization of the gamma-ray signal from the central Milky Way: A case for annihilating dark matter*, *Phys. Dark Univ.* **12** (2016) 1–23, [arXiv:1402.6703].

[184] K. N. Abazajian and M. Kaplinghat, *Detection of a Gamma-Ray Source in the Galactic Center Consistent with Extended Emission from Dark Matter Annihilation and Concentrated Astrophysical Emission*, *Phys. Rev.* **D86** (2012) 083511, [arXiv:1207.6047]. [Erratum: Phys. Rev.D87,129902(2013)].

[185] D. Hooper and T. Linden, *On The Origin Of The Gamma Rays From The Galactic Center*, *Phys. Rev.* **D84** (2011) 123005, [arXiv:1110.0006].

[186] D. Hooper and L. Goodenough, *Dark Matter Annihilation in The Galactic Center As Seen by the Fermi Gamma Ray Space Telescope*, *Phys. Lett.* **B697** (2011) 412–428, [arXiv:1010.2752].

[187] L. Goodenough and D. Hooper, *Possible Evidence For Dark Matter Annihilation In The Inner Milky Way From The Fermi Gamma Ray Space Telescope*, arXiv:0910.2998.

[188] M. Srednicki, S. Theisen, and J. Silk, *Cosmic Quarkonium: A Probe of Dark Matter*, *Phys. Rev. Lett.* **56** (1986) 263. [Erratum: Phys. Rev. Lett.56,1883(1986)].

[189] S. Rudaz, *Cosmic Production of Quarkonium?*, *Phys. Rev. Lett.* **56** (1986) 2128.

[190] L. Bergstrom and H. Snellman, *Observable Monochromatic Photons From Cosmic Photino Annihilation*, *Phys. Rev.* **D37** (1988) 3737–3741.

[191] **HESS**, A. Abramowski *et. al.*, *Search for Photon-Linelike Signatures from Dark Matter Annihilations with H.E.S.S.*, *Phys. Rev. Lett.* **110** (2013) 041301, [arXiv:1301.1173].

[192] B. Anderson, S. Zimmer, J. Conrad, M. Gustafsson, M. Sánchez-Conde, and R. Caputo, *Search for Gamma-Ray Lines towards Galaxy Clusters with the Fermi-LAT*, *JCAP* **1602** (2016), no. 02 026, [arXiv:1511.00014].

[193] J. Aleksić *et. al.*, *Optimized dark matter searches in deep observations of Segue 1 with MAGIC*, *JCAP* **1402** (2014) 008, [arXiv:1312.1535].

[194] A. Geringer-Sameth and S. M. Koushiappas, *Dark matter line search using a joint analysis of dwarf galaxies with the Fermi Gamma-ray Space Telescope*, *Phys. Rev.* **D86** (2012) 021302, [arXiv:1206.0796].

[195] C. Weniger, *A Tentative Gamma-Ray Line from Dark Matter Annihilation at the Fermi Large Area Telescope*, *JCAP* **1208** (2012) 007, [arXiv:1204.2797].

[196] T. Bringmann, X. Huang, A. Ibarra, S. Vogl, and C. Weniger, *Fermi LAT Search for Internal Bremsstrahlung Signatures from Dark Matter Annihilation*, *JCAP* **1207** (2012) 054, [arXiv:1203.1312].

[197] T. Bringmann, L. Bergstrom, and J. Edsjo, *New Gamma-Ray Contributions to Supersymmetric Dark Matter Annihilation*, *JHEP* **01** (2008) 049, [arXiv:0710.3169].

[198] R. Flores, K. A. Olive, and S. Rudaz, *Radiative Processes in Lsp Annihilation*, *Phys. Lett.* **B232** (1989) 377–382.

[199] L. Bergstrom, *Radiative Processes in Dark Matter Photino Annihilation*, *Phys. Lett.* **B225** (1989) 372–380.

[200] A. Ibarra, S. Lopez Gehler, and M. Pato, *Dark matter constraints from box-shaped gamma-ray features*, *JCAP* **1207** (2012) 043, [arXiv:1205.0007].

[201] **Fermi-LAT**, W. B. Atwood *et. al.*, *The Large Area Telescope on the Fermi Gamma-ray Space Telescope Mission*, *Astrophys. J.* **697** (2009) 1071–1102, [arXiv:0902.1089].

[202] https://www-glast.stanford.edu/.

[203] M. Su, T. R. Slatyer, and D. P. Finkbeiner, *Giant Gamma-ray Bubbles from Fermi-LAT: AGN Activity or Bipolar Galactic Wind?*, *Astrophys. J.* **724** (2010) 1044–1082, [arXiv:1005.5480].

[204] **HESS**, H. Hofmann, *The HESS project*, in *International Symposium: The Universe Viewed in Gamma Rays Kashiwa, Chiba, Japan, September 25-28, 2002*, p. T03, 2002.

[205] https://www.mpi-hd.mpg.de/hfm/HESS/.

[206] **CTA Consortium**, M. Actis *et. al.*, *Design concepts for the Cherenkov Telescope Array CTA: An advanced facility for ground-based high-energy gamma-ray astronomy*, *Exper.Astron.* **32** (2011) 193–316, [arXiv:1008.3703].

[207] https://www.cta-observatory.org/.

[208] K. Bernlöhr *et. al.*, *Monte Carlo design studies for the Cherenkov Telescope Array*, *Astropart. Phys.* **43** (2013) 171–188, [arXiv:1210.3503].

[209] https://portal.cta-observatory.org/Pages/CTA-Performance.aspx.

[210] **HAWC**, G. Sinnis, *HAWC: A next generation VHE all-sky telescope*, *AIP Conf. Proc.* **745** (2005) 234–245. [,234(2005)].

[211] M. Tluczykont, D. Hampf, D. Horns, T. Kneiske, R. Eichler, R. Nachtigall, and G. Rowell, *The ground-based large-area wide-angle gamma-ray and cosmic-ray experiment HiSCORE*, *Adv. Space Res.* **48** (2011) 1935–1941, [arXiv:1108.5880].

[212] G. G. Raffelt, *Stars as laboratories for fundamental physics*. 1996.

[213] E. Wigner, *Gruppentheorie und ihre Anwendung auf die Quantenmechanik der Atomspektren*. 1931.

[214] L. D. Landau, *On the angular momentum of a system of two photons*, *Dokl. Akad. Nauk Ser. Fiz.* **60** (1948), no. 2 207–209.

[215] C.-N. Yang, *Selection Rules for the Dematerialization of a Particle Into Two Photons*, *Phys. Rev.* **77** (1950) 242–245.

[216] C. Garcia-Cely and J. Heeck, *Polynomial spectral features from dark matter and connection to the diphoton resonance*, arXiv:1605.08049.

[217] R. D. Peccei and H. R. Quinn, *CP Conservation in the Presence of Instantons*, *Phys. Rev. Lett.* **38** (1977) 1440–1443.

[218] D. G. Cerdeno, M. Peiro, and S. Robles, *Enhanced lines and box-shaped features in the gamma-ray spectrum from annihilating dark matter in the NMSSM*, *JCAP* **1604** (2016), no. 04 011, [arXiv:1507.08974].

[219] D. G. Cerdeno, M. Peiro, and S. Robles, *Fits to the Fermi-LAT GeV excess with RH sneutrino dark matter: implications for direct and indirect dark matter searches and the LHC*, *Phys. Rev.* **D91** (2015), no. 12 123530, [arXiv:1501.01296].

[220] C. Garcia-Cely, A. Ibarra, and E. Molinaro, *Cosmological and astrophysical signatures of dark matter annihilations into pseudo-Goldstone bosons*, *JCAP* **1402** (2014) 032, [arXiv:1312.3578].

[221] H. M. Lee, M. Park, and W.-I. Park, *Fermi Gamma Ray Line at 130 GeV from Axion-Mediated Dark Matter*, *Phys. Rev.* **D86** (2012) 103502, [arXiv:1205.4675].

[222] H. M. Lee, M. Park, and W.-I. Park, *Axion-mediated dark matter and Higgs diphoton signal*, *JHEP* **12** (2012) 037, [arXiv:1209.1955].

[223] H. M. Lee, M. Park, and V. Sanz, *Interplay between Fermi gamma-ray lines and collider searches*, *JHEP* **03** (2013) 052, [arXiv:1212.5647].

[224] P. Gondolo and G. Gelmini, *Cosmic abundances of stable particles: Improved analysis*, *Nucl. Phys.* **B360** (1991) 145–179.

[225] Y. Nomura and J. Thaler, *Dark Matter through the Axion Portal*, *Phys. Rev.* **D79** (2009) 075008, [arXiv:0810.5397].

[226] J. Mardon, Y. Nomura, D. Stolarski, and J. Thaler, *Dark Matter Signals from Cascade Annihilations*, *JCAP* **0905** (2009) 016, [arXiv:0901.2926].

[227] J. Mardon, Y. Nomura, and J. Thaler, *Cosmic Signals from the Hidden Sector*, *Phys. Rev.* **D80** (2009) 035013, [arXiv:0905.3749].

[228] M. Cirelli, M. Kadastik, M. Raidal, and A. Strumia, *Model-independent implications of the e+-, anti-proton cosmic ray spectra on properties of Dark Matter*, *Nucl. Phys.* **B813** (2009) 1–21, [arXiv:0809.2409]. [Addendum: Nucl. Phys.B873,530(2013)].

[229] N. Arkani-Hamed, D. P. Finkbeiner, T. R. Slatyer, and N. Weiner, *A Theory of Dark Matter*, *Phys. Rev.* **D79** (2009) 015014, [arXiv:0810.0713].

[230] J. Hisano, S. Matsumoto, M. M. Nojiri, and O. Saito, *Non-perturbative effect on dark matter annihilation and gamma ray signature from galactic center*, *Phys. Rev.* **D71** (2005) 063528, [hep-ph/0412403].

[231] M. Pospelov and A. Ritz, *Astrophysical Signatures of Secluded Dark Matter*, *Phys. Lett.* **B671** (2009) 391–397, [arXiv:0810.1502].

[232] J. McDonald, *Gauge singlet scalars as cold dark matter*, *Phys. Rev.* **D50** (1994) 3637–3649, [hep-ph/0702143].

[233] B. Patt and F. Wilczek, *Higgs-field portal into hidden sectors*, hep-ph/0605188.

[234] F. F. Deppisch, P. S. Bhupal Dev, and A. Pilaftsis, *Neutrinos and Collider Physics*, *New J. Phys.* **17** (2015), no. 7 075019, [arXiv:1502.06541].

[235] A. Kusenko, *Sterile neutrinos: The Dark side of the light fermions*, *Phys. Rept.* **481** (2009) 1–28, [arXiv:0906.2968].

[236] A. Atre, T. Han, S. Pascoli, and B. Zhang, *The Search for Heavy Majorana Neutrinos*, *JHEP* **05** (2009) 030, [arXiv:0901.3589].

[237] F.-X. Josse-Michaux and E. Molinaro, *A Common Framework for Dark Matter, Leptogenesis and Neutrino Masses*, *Phys. Rev.* **D84** (2011) 125021, [arXiv:1108.0482].

[238] F.-X. Josse-Michaux and E. Molinaro, *Triplet scalar dark matter and leptogenesis in an inverse seesaw model of neutrino mass generation*, *Phys. Rev.* **D87** (2013), no. 3 036007, [arXiv:1210.7202].

[239] F. del Aguila and J. A. Aguilar-Saavedra, *Electroweak scale seesaw and heavy Dirac neutrino signals at LHC*, *Phys. Lett.* **B672** (2009) 158–165, [arXiv:0809.2096].

[240] M. B. Gavela, T. Hambye, D. Hernandez, and P. Hernandez, *Minimal Flavour Seesaw Models*, *JHEP* **09** (2009) 038, [arXiv:0906.1461].

[241] A. Ibarra, E. Molinaro, and S. T. Petcov, *TeV Scale See-Saw Mechanisms of Neutrino Mass Generation, the Majorana Nature of the Heavy Singlet Neutrinos and $(\beta\beta)_{0\nu}$-Decay*, *JHEP* **09** (2010) 108, [arXiv:1007.2378].

[242] A. Ibarra, E. Molinaro, and S. T. Petcov, *Low Energy Signatures of the TeV Scale See-Saw Mechanism*, *Phys. Rev.* **D84** (2011) 013005, [arXiv:1103.6217].

[243] D. N. Dinh, A. Ibarra, E. Molinaro, and S. T. Petcov, *The $\mu - e$ Conversion in Nuclei, $\mu \to e\gamma, \mu \to 3e$ Decays and TeV Scale See-Saw Scenarios of Neutrino Mass Generation*, *JHEP* **08** (2012) 125, [arXiv:1205.4671]. [Erratum: JHEP09,023(2013)].

[244] J. Lopez-Pavon, E. Molinaro, and S. T. Petcov, *Radiative Corrections to Light Neutrino Masses in Low Scale Type I Seesaw Scenarios and Neutrinoless Double Beta Decay*, *JHEP* **11** (2015) 030, [arXiv:1506.05296].

[245] P. B. Pal and L. Wolfenstein, *Radiative Decays of Massive Neutrinos*, *Phys. Rev.* **D25** (1982) 766.

[246] G. Vertongen and C. Weniger, *Hunting Dark Matter Gamma-Ray Lines with the Fermi LAT*, *JCAP* **1105** (2011) 027, [arXiv:1101.2610].

[247] W. A. Rolke, A. M. Lopez, and J. Conrad, *Limits and confidence intervals in the presence of nuisance parameters*, *Nucl. Instrum. Meth.* **A551** (2005) 493–503, [physics/0403059].

[248] T. Bringmann, F. Calore, G. Vertongen, and C. Weniger, *On the Relevance of Sharp Gamma-Ray Features for Indirect Dark Matter Searches*, *Phys. Rev.* **D84** (2011) 103525, [arXiv:1106.1874].

[249] G. Cowan, *Statistical data analysis*. 1998.

[250] https://www.slac.stanford.edu/exp/glast/groups/canda/lat_Performance.htm.

[251] http://fermi.gsfc.nasa.gov/ssc/data/access/.

[252] http://fermi.gsfc.nasa.gov/ssc/data/analysis/.

[253] http://fermi.gsfc.nasa.gov/ssc/data/analysis/software/.

[254] **Fermi-LAT**, M. Ackermann *et. al.*, *Search for gamma-ray spectral lines with the Fermi large area telescope and dark matter implications*, *Phys. Rev.* **D88** (2013) 082002, [arXiv:1305.5597].

[255] **HESS**, A. Abramowski *et. al.*, *Search for a Dark Matter annihilation signal from the Galactic Center halo with H.E.S.S*, *Phys. Rev. Lett.* **106** (2011) 161301, [arXiv:1103.3266].

[256] R. K. Bock *et. al.*, *Methods for multidimensional event classification: A case study using images from a Cherenkov gamma-ray telescope*, *Nucl. Instrum. Meth.* **A516** (2004) 511–528.

[257] J. R. Hoerandel, *On the knee in the energy spectrum of cosmic rays*, *Astropart.Phys.* **19** (2003) 193–220, [astro-ph/0210453].

[258] D. Maurin, F. Melot, and R. Taillet, *CRDB: a database of charged cosmic rays*, *Astron.Astrophys.* **569** (2014) A32, [arXiv:1302.5525].

[259] D. J. Fegan, *TOPICAL REVIEW: gamma/hadron separation at TeV energies*, *Journal of Physics G Nuclear Physics* **23** (Sept., 1997) 1013–1060.

[260] **H.E.S.S. Collaboration**, F. Aharonian *et. al.*, *The energy spectrum of cosmic-ray electrons at TeV energies*, *Phys.Rev.Lett.* **101** (2008) 261104, [arXiv:0811.3894].

[261] **AMS Collaboration**, M. Aguilar *et. al.*, *Precision Measurement of the $(e^+ + e^-)$ Flux in Primary Cosmic Rays from 0.5 GeV to 1 TeV with the Alpha Magnetic Spectrometer on the International Space Station*, *Phys.Rev.Lett.* **113** (2014), no. 22 221102.

[262] **H.E.S.S. Collaboration**, F. Aharonian *et. al.*, *Discovery of very-high-energy gamma-rays from the galactic centre ridge*, *Nature* **439** (2006) 695–698, [astro-ph/0603021].

[263] M. Chernyakova, D. Malyshev, F. A. Aharonian, R. M. Crocker, and D. I. Jones, *The high-energy, Arcminute-scale galactic center gamma-ray source*, *Astrophys. J.* **726** (2011) 60, [arXiv:1009.2630].

[264] **HESS**, F. Aharonian *et. al.*, *H.E.S.S. observations of the Galactic Center region and their possible dark matter interpretation*, *Phys. Rev. Lett.* **97** (2006) 221102, [astro-ph/0610509]. [Erratum: Phys. Rev. Lett.97,249901(2006)].

[265] V. Lefranc, E. Moulin, P. Panci, and J. Silk, *Prospects for Annihilating Dark Matter in the inner Galactic halo by the Cherenkov Telescope Array*, *Phys. Rev.* **D91** (2015), no. 12 122003, [arXiv:1502.05064].

[266] T. A. Porter and A. Strong, *A New estimate of the Galactic interstellar radiation field between 0.1 microns and 1000 microns*, astro-ph/0507119.

[267] I. V. Moskalenko, T. A. Porter, and A. W. Strong, *Attenuation of vhe gamma rays by the milky way interstellar radiation field*, *Astrophys.J.* **640** (2006) L155–L158, [astro-ph/0511149].

[268] H. Silverwood, C. Weniger, P. Scott, and G. Bertone, *A realistic assessment of the CTA sensitivity to dark matter annihilation*, *JCAP* **1503** (2015), no. 03 055, [arXiv:1408.4131].

[269] M. Pierre, J. M. Siegal-Gaskins, and P. Scott, *Sensitivity of CTA to dark matter signals from the Galactic Center*, *JCAP* **1406** (2014) 024, [arXiv:1401.7330]. [Erratum: JCAP1410,E01(2014)].